Theoretical calculations of the magnetic properties of inorganic molecules.

A thesis submitted to The University of Manchester for the degree of Doctor of Philosophy in the School of Chemistry.

2013

Simon Bennie MChem

Contents:

List of Tables

List of Figures.

Abstract

The original research in this thesis is by Simon Jonathan Bennie for the degree of Doctor of Philosophy in 2013 in the subject of Theoretical Chemistry. The work was conducted at The University of Manchester in the School of Chemistry.

The zero field splittings (ZFS) of inorganic molecules were studied with a view to understanding the applicability of new methods in Density Functional Theory (DFT). The initial thrust of this work was to benchmark the three methods available: Pederson Kahana, quasirestricted orbitals and the coupled perturbed equations. Simple 3d monometallic systems were studied with a unique focus on the effect of adjusting the basis set size of the metal. We also studied the effect of a range of commonly available functionals. We found that by using a large quadruple zeta basis set that the results of general gradient approximation (GGA) functionals can be improved. Hybrid functionals were found not to be as accurate as the GGAs and are often degraded by going to a larger basis. The degree of accuracy appears to be a function of the covalency of the metal to ligand bond as measured by the Mayer bond orders and Mulliken charges. We also present the results for complete active space self consistent field calculations and ZFS values for restricted open DFT determinants coupled with the multi-reference configuration interaction methods of obtaining the ZFS.

Chapter 5 of this work focuses of the characterisation of a more complex di-chromium system called Kremer's dimer. This system has three magnetically active spin states each of which has well-defined ZFS values. Under the broken symmetry method we found no functional to be able to qualitatively reproduce the ordering of the spin state or the ZFS. Through analysis of the natural orbitals and spin eigenvalues we determined that this is due to a strong amount of multi-configurational character. Simple complete active space self consistent field (CASSCF) calculations were found to reproduce the experimental spin ladder. Multi-reference configuration interaction on the CASSCF solutions were found to accurately calculate the experimental ZFS values, with state optimised calculations being the most accurate choice for the CASSCF.

Declaration

No portion of the work referred to in the thesis has been submitted in support of an application for another degree or qualification of this or any other university or other institute of learning;

Copyright

Thesis restriction declarations deposited in the University Library, The University Library's regulations (see http://www.manchester.ac.uk/library/aboutus/regulations) and in The University's policy on Presentation of Theses.

Dedication.

To my father: your support every day of my life has made this thesis possible. You have been my source of strength through all the bad times and my source of laughter in the good times. You are without a doubt my idol and hero.

Acknowledgments.

This work was funded by the Engineering and Physical Sciences Research Council (EPSRC), under the supervision of Dr J. J. W. McDouall and Prof. D. Collison, both of whose advice and guidance was critical in this work.

I would like to acknowledge Dr M. Vincent for his technical support and useful discussions and Dr N. Burton who supported my application to this Ph.D and has offered me continuing encouragement over the last 5 years.

The Author.

Simon Bennie graduated from The University of Manchester in 2009 with an upper second-class masters degree in chemistry. His interest in computational chemistry started in his third year when he undertook an unpaid internship with Prof. P. L. A. Popelier. He conducted his 4th year research project on the magnetic properties of actinides under the supervision of Dr N. Burton. During his Ph.D he has presented two posters on his research and has given oral presentations numerous times, including at the American Chemical Society meeting in Philadelphia. His final year oral presentation won first prize for the Inorganic/Physical sections, leading him to present at the regional Dalton meeting. He has attended numerous workshops such as the Oxford Theoretical Chemistry Summer School and the Electronic Structure Workshop in Essen. In the last year he has finished a separate 4 month research project for the Science and Technology Facilities Council (STFC). Chapter 5 of this thesis was published in the Journal of Computational and Theoretical Chemistry.[1]

Chapter 1: Introduction

1.1 The importance of spin-nano magnets.

The data storage industry is fast approaching the limit of the traditional bulk magnets used in computer hard drives. The ferromagnets that have been employed since IBM introduced the technology in 1953 are fundamentally limited, since the data becomes more volatile as the bit is made smaller. This has been termed the super-paramagnetic limit.[2,3] Increasingly sophisticated methods are being used to evade this limit, such as perpendicular storage[4] or using different substrates in disk construction. The issue is that as the domain of these bulk ferromagnets decreases, the potential for spontaneous demagnetisation (randomisation of spin orientation) becomes greater. Currently the bulk magnetic domain (which is made out of many small magnetic grains) is around the order of 100 nm.[5,6] Instead of continuing to evade this limit it is possible to take a "bottom up" chemical approach to the construction of the magnetic bit. The ultimate goal of the nano-magnet is to create a molecule that is stable at room temperature, that retains its spin orientation for long periods and that can be easily read or manipulated. If this can be achieved then a new age of quantum storage is possible.

1.2 The single molecule magnet and the potential of quantum storage.

The single molecule magnet[7,8] (SMM) is one approach to creating a molecular bit. Each individual molecule is used to store data as the orientation of its electronic spin. The critical equation that governs the eligibility of an SMM takes the form

$$E = |D|S^2 \qquad (1.1)$$

where *E* is the energy of the spin reversal barrier, *S* is the total spin of the system and *D* is the large component of the magnetic anisotropy. The energy barrier dictates the

temperature up to which the spin retains its stability and thus controls the magnetic half life of a nano-magnet. The issue of constructing large energy barriers is a chemical problem with two avenues to exploit, either the total spin of the system or the magnetic anisotropy could be increased. The current experimental trend is to construct ever larger clusters of inorganic molecules that contain multiple spin-unpaired electrons.[9] To create a molecule with a large paramagnetic ground state there are three main options; using a heterometallic system where the metal spins are unbalanced, a homometallic system that contains an odd number of metal centres or a spin frustrated system. There is on-going research into the applicability of f block elements[10,11] to attain ever higher ground state spins. A limitation of this approach is becoming apparent in that although the energy barrier scales as S^2, the D tensor tends to scale as $\sim S^{-2}$ and thus renders the barrier increasing with spin of the order of S^0.[12,13] A second factor in the construction of an SMM that must be considered is the magnetic anisotropy, D, which determines the spacing between the various spin states along the energy barrier.

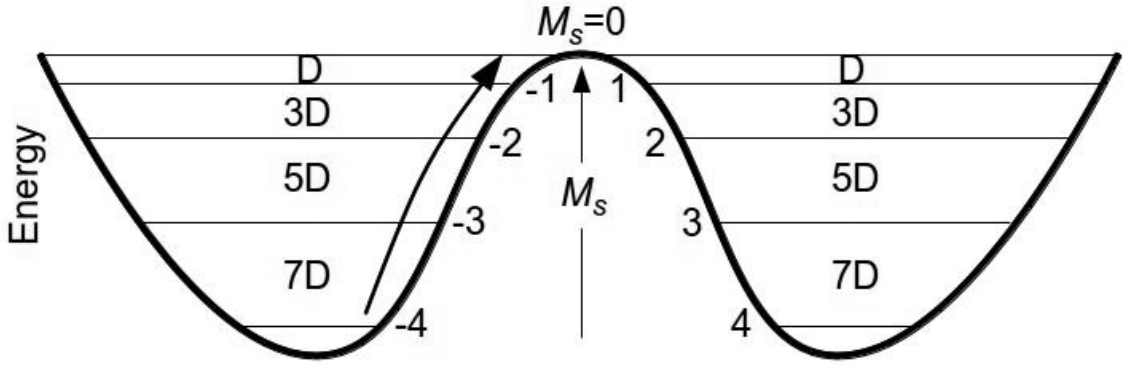

Figure 1: Diagram of the SMM energy barrier for an S = 4 system.

Where in Figure 1 M_s is the projection of spin in the S_z direction (the spin quantisation axis). To create an SMM, D must be negative as this guarantees a ground state where the spin is all aligned along S_z and thus has a defined orientation for manipulation. As the molecule is excited and accesses higher lying M_s states, the spin is

less orientated along S_z until it reaches the top of the energy barrier where $M_s = 0$ and is no longer orientated along that axis, at this point data would be lost. A discussion of the quantum tunnelling mechanism is outside the work of this thesis. *D* is a difficult parameter to control chemically as in inorganic systems it is dominated by spin-orbit coupling (SOC) and is extremely sensitive to ligand effects. It is this phenomenon that is the primary concern in this work.

1.3 The role of theory in developing new magnetic molecules.

Theoretical chemistry has some clear advantages in elucidating what is needed to create large *D* values. We are able to break *D* into its component factors of spin-spin interaction and spin-orbit coupling. We are then able to break down the spin-orbit coupling further and analyse the way its components influence its magnitude. Being able to calculate large SMMs is however out of the reach of pure wavefunction methods due to their high computational cost, instead we must turn to density-functional theory (DFT), which has a much better scaling factor. Recently, Frank Neese developed new methods of calculating the ZFS in a DFT framework, however it remains unclear if DFT in its current form is able to accurately model the coupling of the excited spin states needed to calculate *D*. Some analogy can be made to the electronic *g* factor which is now readily studied in theory with a good degree of accuracy.[14] However, this is where the current limit of theoretical chemistry lies as the *g* value only involves the coupling of electronic configurations of the same spin and the *D* value requires the coupling of excited states that can vary from the state of interest by $S \pm 1$. It is not clear that DFT is able to accurately model excited states of this nature as it is a theory of the ground state density. DFT studies so far show qualitative agreement with experiment.[15] The historic calculations of ZFS were done with *ab initio* methods.[16,17] In this work we present a comparison of different methods to calculate *D* as well as data on the sensitivity of this

value to the choice of functional. We also present the current limit of DFT at calculating inorganic systems and show how multi-configurational methods are required in certain situations.

Chapter 2: Theoretical basis of this work.

2.1.1 Many electron wavefunctions.

Quantum chemistry is the study of different approximations to replicate the physical intricacies of the motion of electrons as they interact around nuclei. The complexity of the field arises because it does not follow the basic recipe of classical mechanics, i.e. to take in certain parameters such as charge or momentum and to predict the positions of a moiety such as an electron at some point in the future. The fundamental attribute in the quantum nature of matter is that position and momentum cannot be simultaneously known, this accords with the Heisenberg uncertainty principle and is what renders classical mechanics to be inapplicable for small systems. By substituting the momentum function with the derivative of position ($p_x \rightarrow d/dx$) one can come to the time dependent Schrödinger equation and with the further separation of the time variable to the time independent Schrödinger equation (equation **2.1**). This is the wave equation for the motion of an electronic system under the restrictions of quantum mechanics (i.e. within boundary conditions) as a steady state and without relativistic considerations.

$$\hat{H}\Psi = E\Psi \tag{2.1}$$

Where $\hat{H}$ is the Hamiltonian of the system and Ψ is the many electron wavefunction. Each wavefunction is a function of the position of multiple electrons and nuclei:

$$\begin{aligned}\hat{H}\Psi(x_1, x_2, x_3, \dots, x_n, R_1, R_2, R_3, \dots, R_n) \\ = E\Psi(x_1, x_2, x_3, \dots, x_n, R_1, R_2, R_3, \dots, R_n)\end{aligned} \tag{2.2}$$

where each electron has the space and spin position x_i and the nuclei at R_i.

2.1.2 The meaning of the wavefunction and operators.

According to Born's interpretation, the wavefunction is a probability amplitude, only its square provides the statistical information on the position of electrons. The wavefunction is not an observable and can be complex; instead its presence is experimentally inferred from the observable one electron density ρ(r), a quantity that we discuss in section **2.4**.

Applying a Hermitian operator to the wavefunction allows the determination of a property. In the case of the Schrödinger equation the operator is the Hamiltonian and the property that it exposes (its eigenvalue) is the energy of that electronic wavefunction.

The Hamiltonian function of classical mechanics is a special formulation that describes the energy of a system as the potential energy plus the kinetic energy. When the quantum mechanical momentum substitutions are made, the many electron Hamiltonian takes the form

$$\hat{H} = -\sum_{i=1}^{N}\frac{\nabla_i^2}{2} - \sum_{A=1}^{M}\frac{\nabla_A^2}{2M_A} - \sum_{i=1}^{N}\sum_{A=1}^{M}\frac{Z_A}{r_{iA}} + \sum_{A>B}^{M}\frac{Z_A Z_B}{R_{AB}} + \sum_{i>j}^{N}\frac{1}{r_{ij}} \qquad (2.3)$$

where the ∇^2 is the Laplacian operator or kinetic energy operator. This operator is constructed out of the square of the momentum operator (the derivative of the electronic position) as is needed when describing momentum in quantum mechanics. With some algebraic manipulation, equation **2.3** can be rendered in spherical coordinates and solved to find the hydrogenic orbitals. Such one electron cases are the only time in which the Schrödinger equation is exactly solvable. It is the final inter-electron term that causes difficulty in quantum chemistry as it is a many-body problem.

2.1.3 The form of the wavefunction and eigenequations.

The quantisation of nature does not allow a continuum of solutions for the energy of matter, instead it must have discrete values. The use of an eigenequation enforces quantisation by selecting functional forms that are harmonics within the boundary conditions of the system. The wavefunction must be finite, continuous and single valued. When applying the Hamiltonian operator to a wavefunction one wishes to find the eigenfunctions which correspond to the possible electronic energy levels. This means that the operator returns the same function that it has acted on multiplied by a constant. The derivative in the kinetic term of the Schrödinger equation means that acceptable functions from which to form a basis are exponentials, sines and cosines.

2.1.4 Energy operator and the Born-Oppenheimer approximation.

The small mass of electrons means that as they orbit heavy nuclei they are able to respond effectively instantaneously to any change in nuclear coordinates. This opens up an avenue to reduce the computational cost of the full Hamiltonian. It can be said that the electronic wavefunction depends explicitly on the electronic coordinates but only parametrically on the nuclear coordinates. By removing the nuclear kinetic energy term and the nuclear repulsive energy from equation **2.3** we arrive at the Born-Oppenheimer Hamiltonian.

$$\hat{H} = -\sum_{i=1}^{N}\frac{\nabla_i^2}{2} - \sum_{i=1}^{N}\sum_{A=1}^{M}\frac{Z_A}{r_{iA}} \sum_{A>B}^{M}\frac{Z_A Z_B}{R_{AB}} + \sum_{i>j}^{N}\frac{1}{r_{ij}} \qquad (2.4)$$

By applying equation **2.4** one is able to neglect the kinetic motion of the nuclei and calculate the electronic energy for a fixed molecular geometry. To recover the total energy the nuclear-nuclear repulsion has to be added to the end of the electronic structure calculation, but this need only be calculated once per geometry.

2.1.5 Spin operators.

The electronic Schrödinger equation (**2.1**) covers the Cartesian degrees of freedom that an electron possesses. The Stern-Gerlach experiments[18] proved that under the influence of a homogeneous external field, **B**, atoms with an unpaired electron are divided according to the energy of their interaction with the external field into a doublet. The origin of this interaction can only be explained by electrons possessing an internal degree of freedom that has been termed 'spin' or internal angular momentum. Because the electron is a charged particle this 'internal motion' creates a small magnetic field that determines the electron's interaction with external fields (as exploited in EPR). When the electron's field is aligned with **B** it is deflected along the direction of the field (lowered in energy in EPR), when anti-aligned the electron is deflected against the direction of **B** (raised in energy in EPR). This property is manifestly similar to the angular momentum of an electronic orbit, but is not an accurate description of the physical reality as spin is a pure quantum phenomenon. The key feature of electronic spin is that it obeys the same rules as traditional quantised angular momentum,[19] the main difference is that it is of half integer value opposed to the unit values observed in orbital motion.

$$S^2|S, M_s\rangle = S(S+1)|S, M_s\rangle \tag{2.5}$$

$$\langle S^2\rangle = S(S+1) = \left(\frac{N_\alpha - N_\beta}{2}\right)\left(\frac{N_\alpha - N_\beta}{2} + 1\right) \tag{2.6}$$

Operating S^2 from equation **2.5** on a state returns the total spin magnitude of that state as an eigenvalue, this means that it sums the spin components along the three axes

that the spin could be aligned and returns the total possible value.

$$S_Z|S, M_s\rangle = M_s\ |S, M_s\rangle \tag{2.7}$$

The S_z operator in equation **2.7** provides the spin in the Z direction as M_s eigenvalues (the same values as in Figure 1). These two spin operators commute ($[S^2,S_z]=0$) and thus can be simultaneously observed, but the three spin directions, S_z, S_x and S_y, do not commute. In the absence of magnetic contributions there is no energetic impetus to align the spin along S_z, S_x or S_y and thus the M_s values are all degenerate. The lifting of this degeneracy can be achieved by an external field or by the zero field splitting (ZFS). The use of the non-relativistic Hamiltonian in most electronic structure calculations means that the choice of axis of quantisation for spin is arbitrary and is usually just defined as S_z.

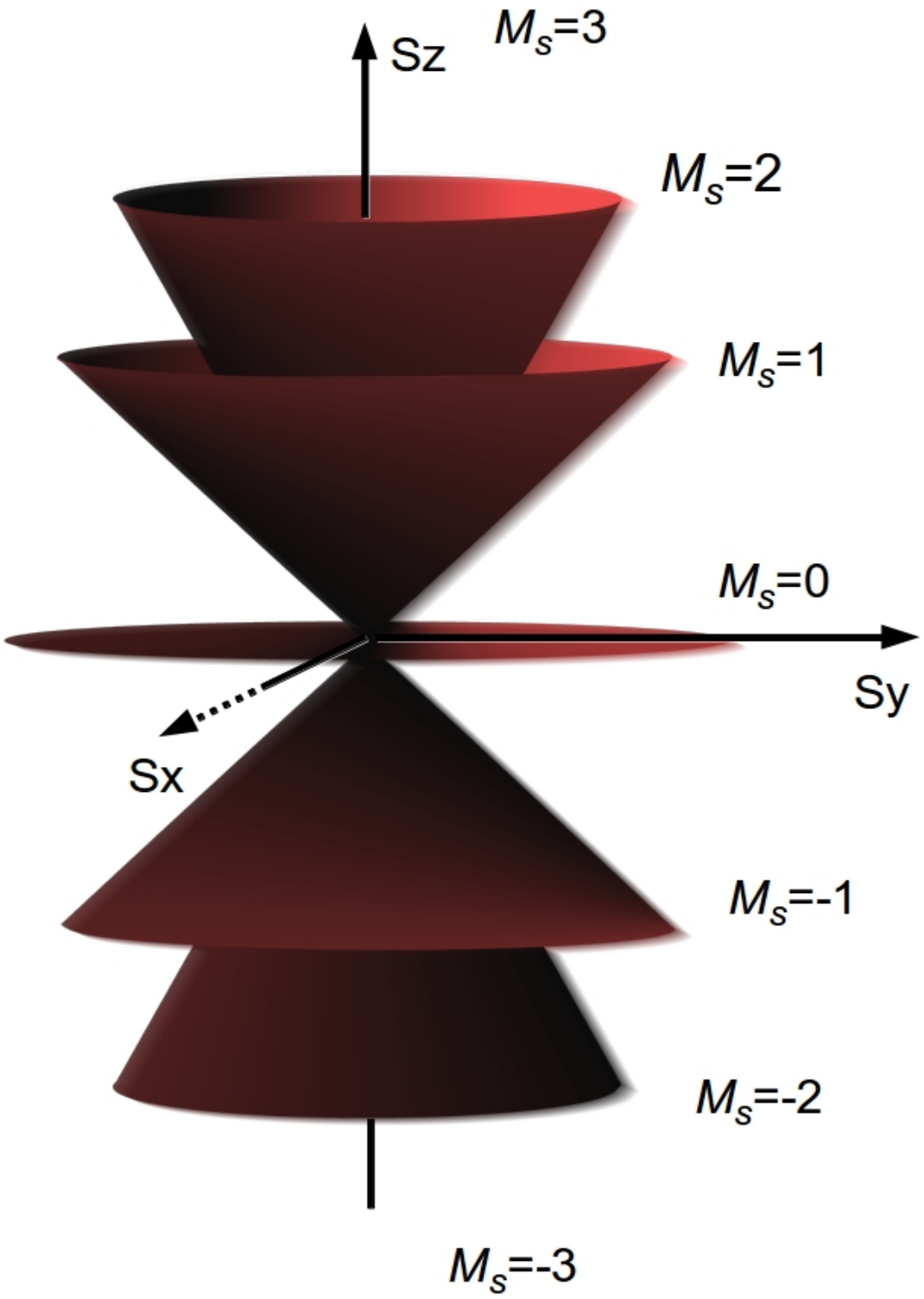

Figure 2: Vector cone diagram showing the possible spin orientations of the spin along the z direction.

The vector model of coupling for visualising M_s is shown in Figure 2. Each vector cone indicates the amount of spin in the S_z direction. When $M_s = 3$ then the state has all its spin aligned along S_z. When $M_s = 0$ there is no spin in the S_z direction, however because of the commutation rules of the spin components it is not possible to determine

along which axis the spin is actually aligned. The cones become wider as the uncertainty of the remaining spin direction increases.

Within the Schrödinger equation the effect of spin can be added by enforcing antisymmetry, but only to the level of neglecting the magnetic effects that arise from angular momentum. To fully calculate spin properties the Dirac equation must be employed (section 2.7).

2.1.6 The spin orbital.

In quantum chemistry the wavefunction is decomposed into a product of one electron functions that chemists call orbitals. From equation **2.2** the wavefunction can be described as the function of an electronic state made out of the electron coordinates (and time). Adding the spin variable to the Cartesian coordinates results in orbitals of the form:

$$\phi(x) = \varphi(r)\sigma(s) \qquad (2.8)$$

The σ indicates the addition of a spin coordinate to the electronic degrees of freedom. The spin function is either α or β and represents the electron spin as being +½ or -½ respectively. This total one electron function is called a spin orbital.

2.1.7 Slater determinants and antisymmetry.

By adding spin as a fourth variable to the electron in non relativistic wavefunctions no additional physics is recovered. To achieve a better description of the many electron wavefunction we are required to enforce the Pauli exclusion principle, which states that any two fermions must be antisymmetric under interchange of their coordinates. To illustrate this we construct an example wavefunction of two fundamental quantum

particles, which can be found either at r_1 or r_2. Because fundamental particles are indistinguishable it is not possible to label a particular one as being at a position and thus the probability $|\Psi|^2$ must be the same if the labels are switched.

$$|\Psi|^2 = [a(r_1)b(r_2)]^2 = [a(r_2)b(r_1)]^2 \tag{2.9}$$

The wavefunction must reflect this and thus must be a linear combination of the two possibilities.

$$\Psi(r_1, r_2) = \frac{1}{\sqrt{2}}(a(r_1)b(r_2) \pm a(r_2)b(r_1)) \tag{2.10}$$

The particles in equation **2.10** have two possible arrangements giving rise to two equally probable combinations, the symmetric combination (+) or the antisymmetric combination (-). If the symmetric combination is taken then the probability ($|\Psi|^2$) of finding both particles is additive and thus greatest when they occupy the same point in space; this is the case for bosons such as photons. When the antisymmetric combination is taken then the probability of both particles being found at the same point in space is zero; this is the case for electrons. If a and b are the same, as would be the case when the electrons have the same quantum number, then the particles occupy all the same positions in space and the antisymmetric combination evaluates to zero. This means that there is zero probability of finding two electrons in the same state, this is the Pauli exclusion principle.

The antisymmetry principle is backed by spectroscopic evidence, this is most often argued based on the excited states of helium.[20] No antisymmetric triplet states or symmetric singlet states have been observed, this is because for a triplet state only the spatial terms can be interchanged and for the singlet state only the spin terms can be

interchanged.

In quantum chemistry antisymmetry on is achieved by using Slater determinants. For a two electron wavefunction this takes the form:

$$\Psi = \frac{1}{\sqrt{2}} \begin{vmatrix} \psi(r_1)\alpha(1) & \psi(r_1)\beta(1) \\ \psi(r_2)\alpha(2) & \psi(r_2)\beta(2) \end{vmatrix} \tag{2.11}$$

The $1/\sqrt{2}$ is a normalisation of the wavefunction and enforces statistical probability of finding an electron when integrated over all space to be 1. If any two columns of a Slater determinant are interchanged then the wavefunction changes in sign, making the wavefunction obey the antisymmetry principle. When any two columns are the same the determinant evaluates to zero, this is in effect a statement that the probability is zero for finding the two electrons in the same state. The Slater determinant also introduces the physics of electron spin pairing, by allowing the electrons to possess the same spatial component provided that they possess opposite spins. In a Slater determinant every electron is associated with every orbital and the indistinguishability of electrons is achieved. It is the combinations of Slater determinants that form the basis of quantum chemistry.

2.2 The Hartree-Fock operator.

2.2.1 The Hartree operator.

The multi-electron wavefunction introduced in equation **2.1** can be made tractable by introducing simplifications to the way the electrons interact. The first simplification is to replace the multi-electron Hamiltonian with a series of non-interacting one electron Hamiltonians.

$$\hat{H} = \sum_{i=1}^{N} h(i) \tag{2.12}$$

Each Hamiltonian *h*(i) contains all the physical interactions of that electron with its surrounding environment. Combining all the one electron functions (orbitals) and their eigenvalues gives:

$$\sum_{i=1}^{N} h(i)\phi_j(x_i) = \sum_{i=1}^{N} \varepsilon_j \, \phi_j(x_i) \tag{2.13}$$

We are thus able to use this approximation as a starting point to construct the many electron wavefunction. The issue with the Hartree product is that it violates the antisymmetry principle and the indistinguishability of electrons by labelling each electron as belonging to a particular orbital χ.

2.2.2 The Fock operator and electron exchange.

Requiring the wavefunction to be antisymmetric and thus to be represented by a Slater determinant, as discussed in section 2.1.7, accounts for indistinguishability. In a Slater determinant the electrons of the same spin are said to be correlated, this means that their motion reflects the position of the other electrons in their environment. The reason this occurs is because the action of a Slater determinant creates a Fermi hole round each electron that makes the probability of finding two electrons of the same spin occupying the same point in space, zero. Thus for a single determinant wavefunction the position of an electron explicitly depends on the position of other electrons with parallel spin. To describe the electronic interaction in a molecular environment the final electron-electron term of the Born-Oppenheimer Hamiltonian must be considered.

$$\hat{H} = \sum_{i=1}^{N} h_i + \sum_{i>j}^{N} \frac{1}{r_{ij}} \tag{2.14}$$

The first term describes the non interacting energy of the electron; its potential energy with respect to the nucleus and its kinetic energy. The second term is the two-electron term that can be broken into two components *J* and *K*. Each electron experiences a Coulombic mean field from the other electrons, described by the two-electron Coulomb operator *J*. This electronic repulsion term makes electrons interact with the mean field of the other electrons in the environment.

$$J_{ij} = \int \psi_i^*(1)\psi_j^*(2)\left(\frac{1}{r_{12}}\right)\psi_i(1)\psi_j(2)\, dv_1 dv_2 \tag{2.15}$$

A second term that arises from the use of Slater determinates is the exchange operator, this is a non-local two-electron operator *K*. The exchange term results directly from the matrix elements of combining the Slater determinant with the Hartree one electron model. The exchange operator switches the position of the electrons in the Coulomb integral. The effect of the exchange operator is to reduce the repulsion of same spin electrons and thus localise them. The form of the *K* integral is given below.

$$K_{ij} = \int \psi_i^*(1)\psi_j^*(2)\left(\frac{1}{r_{12}}\right)\psi_i(2)\psi_j(1)\, dv_1 dv_2 \tag{2.16}$$

Thus to get the energy of any molecular system the Hartree-Fock operator for a closed shell system has the form

$$E = \langle \Psi | H | \Psi \rangle = \sum_{i=1}^{N} h_{ii} + \frac{1}{2} \sum_{i=1}^{N} \sum_{j=1}^{N} (2J_{ij} - K_{ij}) \tag{2.17}$$

From this equation it is clear that there is a double counting of certain Coulomb interactions, in effect the self interaction of an electron, this is exactly cancelled by the exchange integral. Thus it is clear that the total energy of the Hartree-Fock wavefunction is lower than the Hartree solution and in fact the HF solution is the lowest energy solution possible with a single determinant.

2.2.3 The Roothaan-Hall equations.

The Hartree-Fock equations are only exactly numerically solvable in atomic calculations. Roothaan showed that by introducing a truncated basis set of known functions that the HF equations could approximately be solved analytically.

$$\psi_i = \sum_{\mu=1}^{k} C_{\mu i} \phi_\mu \tag{2.18}$$

where $C_{\mu i}$ is the coefficient of function ϕ_μ for orbital *i*. This converts the calculations of molecular orbitals into a matrix problem. By substituting this into the Fock equation we arrive at

$$\hat{F}\Psi = \sum_i f_i \sum_\mu C_{\mu i} \phi_\mu = \sum_i \varepsilon_i \sum_\mu C_{\mu i} \phi_\mu \tag{2.19}$$

To calculate the expectation values this equation is multiplied through by the

complex conjugate of the wavefunction. This results in the formation of the overlap matrix **S** and the Fock matrix **F**. The final form of the Roothaan-Hall equation is then

$$FC = SC\epsilon \tag{2.20}$$

The aim of this equation is to find ***C*** matrices (orbital coefficients) that diagonalise the Fock matrix. However, the orbitals from atomic orbitals are not orthogonal, to correct this the overlap matrix has to be diagonalised as a step in solving this eigenvalue equation.

2.2.4 Self consistent field and variation theorem.

Because the Fock equation depends on the form of the wavefunction it operates on it is not possible to solve the equation exactly, instead a guess starting point is needed and the HF equation is iteratively solved until the energy of the system is minimised.

$$\langle \Psi' | \hat{H} | \Psi' \rangle \geq E_0 \tag{2.21}$$

Any trial wavefunction Ψ' must result in a higher in energy than the true solution. The procedure to solve the Roothaan-Hall equation in order to obtain the eigenvalues is well described in Szabo and Ostland.[21] The most critical aspect is that by taking a set of trial coefficients and inputting them into the Roothaan-Hall equation it is possible to calculate a new set of transformed coefficients from the diagonalised Fock matrix.

2.2.5 Restricted, restricted open and unrestricted calculations.

There are two possible electronic situations in chemistry, true closed-shell situations where there is no EPR information and open-shell calculations, which are magnetically active. Open-shell $S = 0$ systems such as diradicals can be of the second category. The equations shown so far are the closed-shell form but can be extended to the open shell situations. To tackle open shell molecules there are two main methods, based on either restricted open determinants or unrestricted determinants. The Restricted Open Hartree-Fock (ROHF) form is a direct extension of the normal closed shell methodology with the addition of open shell orbitals into the determinant. The Unrestricted Hartree-Fock (UHF) introduces an extra degree of variational freedom to the wavefunction, whereby the α and β orbitals are not required to have the same energies or spatial form, they are said to have broken spin symmetry. Broken symmetry orbitals have a lower symmetry than the molecular symmetry.

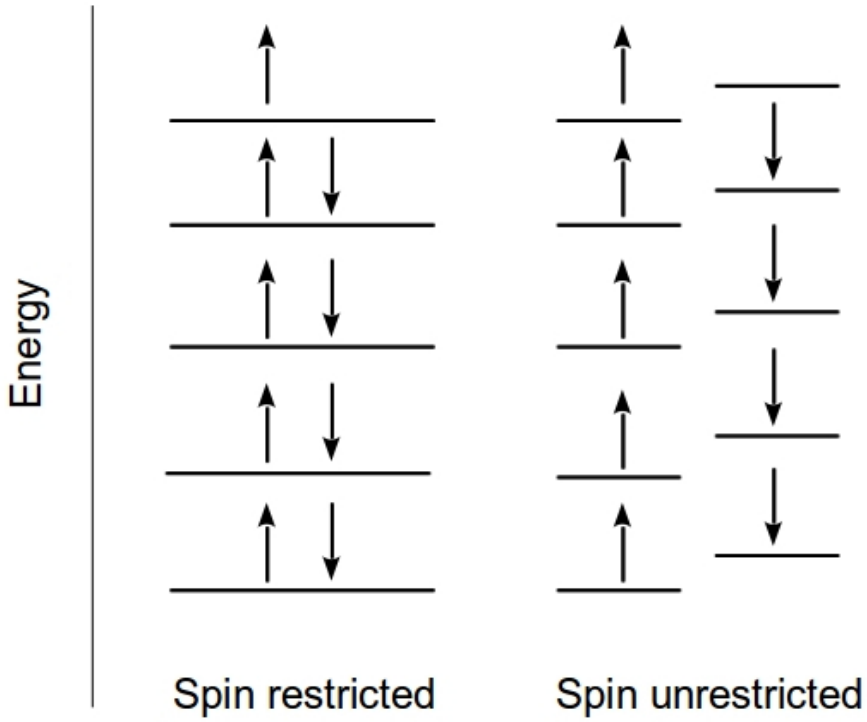

Figure 3: Pictorial representation of spin symmetry breaking for ROHF (left) and UHF (right) determinants.

The UHF method is most commonly used in open-shell quantum chemistry as it introduces some desirable characteristics into the wavefunction. Figure 3 shows the α and β electrons to have different spatial components, which allows the UHF solutions to reproduce homolytic dissociation, whilst the ROHF solution is only able to find the ionic dissociation. This is because in restricted calculations the electron pairs must have the same spatial function and upon dissociation must be both localised on the same atom even if the homolytic dissociation is of lower energy. This has implications for other chemical situations where there can be degeneracy such as in the case of the d block metals being studied in this work.

2.2.6 Spin eigenfunctions and spin contamination

UHF wavefunction calculations have a fundamental flaw in that they do not form spin eigenfunctions as occurs for ROHF determinants (providing their unpaired electrons are parallel). This means that the expectation values of the $\hat{S}^2$ operator on UHF wavefunctions have deviations which make them larger than the ideal ROHF expectation value. To evaluate the expectation value from the $\hat{S}^2$ operator in UHF calculations we use the form:

$$\langle s^2 \rangle = \left(\frac{N_\alpha - N_\beta}{2}\right)\left(\frac{N_\alpha - N_\beta}{2} + 1\right) + N_\beta - \sum_i^{N_\alpha} \sum_j^{N_\beta} \left|\left\langle \Psi_i^\alpha \middle| \Psi_j^\beta \right\rangle\right|^2 \qquad (2.22)$$

The expectation value for $\hat{S}^2$ for an UHF calculation deviates from the ROHF, by the overlap density between the α and β electrons. The reason for this deviation is that by allowing the spin orbitals to break degeneracy in an open shell state the α electrons are lowered in energy as they experience more exchange than the β electrons, which has the effect of introducing contamination of higher spin states. The same methodology can be

applied to calculating unrestricted singlet states, but there must be an impetus for the alpha and beta electrons to break degeneracy such as mixing the HOMO with its antibonding partner. The introduction of spin contamination significantly affects spin density and properties that are spin dependent and is the reasoning behind the quasi-restricted-orbital (QRO) method developed by Neese, which we discuss in section **2.8.5.5**. Within the unrestricted DFT context it is not appropriate to calculate $\hat{S}^2$ in the same way for UHF because DFT is based on a fictitious non-interacting system. The more rigorous methods[22,23] of calculating the spin magnitude are not commonly implemented in quantum codes. The regular UHF method of calculating spin contaminations is the most common method and this is the method used throughout this work.

2.3 Electron correlation.

2.3.1 The mean field problem and correlation.

The main issue with the Hartree-Fock method is that it is a mean field method, where the full Hamiltonian has been replaced by a model two-electron Hamiltonian. Because of this approximation the HF energy is above the true energy of the system as the electrons of opposite spin are not correlated.

$$E_{HF} = E_{Correlation} - E_{exact} \tag{2.23}$$

The correlation energy is defined as the difference between the HF solution and the exact solution to the many body problem.

2.3.2 CI approaches.

To improve the HF energy it is possible to systematically improve the wavefunction by introducing more states into the HF equations. These states are different Slater determinants that represent excited electronic states.

$$\Psi_A = \sum_i C_i^A \Phi_i \tag{2.24}$$

The total wavefunction Ψ is made up of a linear combination of determinants, and the challenge is to minimise the energy of the system by variation of the coefficients, those states with large coefficients C_i^A are most important to the wavefunction. The inclusion of additional configurations further correlates the wavefunction and reduces the energy of the system. The increased number of Coulomb integrals that arise from the configurations increases the repulsion between the electrons and results in the structure delocalising to minimise the repulsion.

2.3.3 The systematic improvement of the wavefunction.

The inclusion of all possible determinants is not realistic for most molecular systems as the number of configurations quickly rises with the number of orbitals, the scaling problem is described by the binomial coefficient[24]:

$$\binom{2K}{N} = \frac{(2K)!}{(2K-N)!\,N!} \tag{2.25}$$

where there are *N* electrons and *K* orbitals. The difficulty in performing the full configuration interaction (CI) has led to the development of a range of truncation schemes reducing the computational cost. Approximations that are most commonly used include determinants with a restricted number of excitations, normally based

around CI and coupled cluster (CC). There are also methods explicitly designed to improve the spectroscopic properties such as Spectroscopy Orientated CI (SORCI) and Difference Dictate CI (DDCI)[25,26].

2.3.4 The unrestricted natural orbitals.

The HF canonical molecular orbitals are only one of a possible infinite selection of different orbitals that can be used to describe the same state. These orbitals generally maintain molecular symmetry and are useful because they are eigenvectors of the Fock operator. However, other acceptable solutions can be formed by a unitary transformation of the orbitals. One such solution is the natural orbitals (NOs), formed by the diagonalisation of the density matrix. The NOs are generally easier to interpret with chemical arguments and have the advantage that CI calculations started from them are generally more convergent. They are also used in multi-configurational calculations where multiple configurations contribute to a single set of orbitals that can conveniently be represented by the NOs. The Fock operator restricts the orbitals to be occupied as 2, 1 or 0, in the NO the values can be any value between 0-2. This same methods can be extended to unrestricted methods creating the unrestricted natural orbitals (UNOs)

2.4 The Kohn-Sham equations.

The fundamental concept of density functional theory (DFT) is that there is a way of directly obtaining the energy of a molecular system from its probability density. The basis of this concept originates from the uniform electron gas model by Thomas and Fermi in 1927.[27,28] This was improved in 1951 by Slater,[29] who also later devised the popular Xα functional.[30] The proof of density → energy mapping came from the Hohenberg-Kohn theorems in 1964. The basis of all DFT comes from the proof that the non-degenerate ground state of a system is uniquely described by the external potential

that is determined by the density.

$$\rho_0 \Rightarrow (N, Z_A, R_A) \Rightarrow \hat{H} \Rightarrow \Psi_0 \Rightarrow E_0 \tag{2.26}$$

The electronic density thus encompasses all the variables in the system and can be used to create the molecular Hamiltonian, which in turn, can be used to define the Ψ_0 that provides the energy of the system. Because the total energy of the system is the functional of the density, then so are its physical components.

$$E_0[\rho_0] = T[\rho_0] + E_{ee}[\rho_0] + E_{Ne}[\rho_0] \tag{2.27}$$

where *T* is the kinetic energy E_{ee} is the electron-electron repulsion and E_{Ne} is the potential energy of the electron nuclear attraction. The electron-electron repulsion can be broken down into classical Coulombic repulsion and nonclassical contributions.

$$E_{ee}[\rho_0] = \frac{1}{2}\int\int \frac{\rho(\vec{r}_1)\rho(\vec{r}_2)}{r_{12}}\, d\vec{r}_1 d\vec{r}_2 + E_{ncl}[\rho_0] \tag{2.28}$$

From this equation it can be seen that the Coulombic repulsion of the electrons can be calculated as an integral over space, leaving the nonclassical, quantum, terms to be evaluated.

2.4.1 A short cut to the dynamical correlation.

The probabilistic description of the wavefunction gives rise to the central quantity in DFT, the electronic density.[31]

$$\rho(\vec{r}) = N \int \dots \int |\Psi(x_1, x_2, x_3, \dots, x_n)|^2 \, ds_1 d\vec{x}_2 \dots d\vec{x}_n \tag{2.29}$$

Where Ψ is integrated over the volume element dr_1 to result in the one-electron density. $\rho(\vec{r})$ is the probability of finding an electron in a volume of space and, due to indistinguishability, the probability of finding any electron in a volume element is *N* times the one electron probability. The electron density is dependent on the 3 spatial coordinates of the electron opposed to the 4*N* variables (3 space and 1 spin) that are required in the wavefunction methods, making the many body problem far more tractable. The antisymmetry principle is reflected in the electron density through the reduced (or two particle) density matrix[32,33]:

$$\gamma(\vec{x}_1, \vec{x}_2; \vec{x}_1', \vec{x}_2') = N(N-1) \int \dots \int \Psi(\vec{x}_1, \vec{x}_2, \vec{x}_3, \dots, \vec{x}_n) \, \Psi^*(\vec{x}_1', \vec{x}_2', \vec{x}_3, \dots, \vec{x}_n) \, d\vec{x}_3 \dots d\vec{x}_n \tag{2.30}$$

This equation integrates over all the electronic positions other than the $\vec{x}_1'$ and $\vec{x}_2'$ coordinates. This can be expanded into a familiar wavefunction form[34,35]

$$\gamma(\vec{x}_1, \vec{x}_2; \vec{x}_1', \vec{x}_2') = \sum_{i=1}^{N} \sum_{j=1}^{N} \{\psi_i^*(1')\psi_i^*(1)\psi_j^*(2')\psi_j^*(2) - \psi_i^*(1')\psi_j(1)\psi_j^*(2')\psi_i(2)\} \tag{2.31}$$

This reduced density matrix can be expanded to be in the form of the antisymmetic

interaction that occurs in the HF equations. Thus we show the relation between antisymmetry and electron density, however this is not a recipe for how to generate this density. The reduced density matrix can be turned into the pair density by making $\vec{x}_1' = \vec{x}_1$ and $\vec{x}_2' = \vec{x}_2$ and thus making:

$$\rho(\vec{x}_1, \vec{x}_2) = N(N-1) \int \dots \int |\Psi(\vec{x}_1, \vec{x}_2, \vec{x}_3, \dots, \vec{x}_n)|^2 \, d\vec{x}_3 \dots d\vec{x}_n \tag{2.32}$$

This is a critical quantity in DFT as it contains all the information on the pairwise interaction between the electrons and thus provides the information on how electrons distribute with regard to each other when they are in the volume elements $\vec{x}_1$ and $\vec{x}_2$.

2.4.2 Coulomb and Fermi holes.

To provide a better physical description it is necessary for any functional not only to describe the Fermi correlation, as in HF theory, but also to describe the many body Coulomb correlation. Because all electron-electron interaction is encompassed by the pair density it thus must be possible to describe these two types of correlation as parameters of this matrix. Because the pair density can be integrated to the one electron density plus the electron-electron interaction we are able to continue from equation **2.28** and define the nonclassical interactions as the effect of the exchange correlation hole.

$$H_{xc}(\vec{x}_1; \vec{x}_2) = \frac{\rho(\vec{x}_1, \vec{x}_2)}{\rho(\vec{r}_1)} - \rho(\vec{r}_2) \tag{2.33}$$

The pair exchange correlation $H_{xc}(\vec{x}_1; \vec{x}_2)$ can be obtained as the component of the pair density that is not due to the classical interaction of electrons.

$$E_{ee}[\rho_0] = \frac{1}{2}\int\int \frac{\rho(\vec{r}_1)\rho(\vec{r}_2)}{r_{12}} + \frac{1}{2}\int\int \frac{\rho(\vec{r}_1)H_{xc}(\vec{x}_1;\vec{x}_2)}{r_{12}}\, d\vec{r}_1 d\vec{r}_2 \qquad (2.34)$$

The first term is the spin-independent Coulomb repulsion of the two reference electrons. The exchange correlation hole is further composed of two factors, the Fermi hole, h_x, that affects the electronic density by carving a hole around each electron that perturbs electrons of the same spin and the Coulomb hole, h_c, that describes the interactions of electrons of opposite spins. If the correct form of h_{xc} was known then the many body problem would be solved. The exchange hole is the larger contributor to the energy as in post-HF calculations and its correct, non local, description should result in the cancellation of self interaction exactly as occurs through the exchange integral in HF theory.[36] A key restriction of Fermi holes is that their integration over all space must equal -1.

$$\int H_x(\vec{r}_1, \vec{r}_2)\, d\vec{r}_2 = -1 \qquad (2.35)$$

Evaluation the exchange contribution at any point in space for any electron should give a negative value as it reduces the chance of another electron of the same spin being found in that region of space. The integral evaluates to -1 because the space $\vec{r}_1$ contains the spin of the reference electron and thus there are *N*-1 other electrons left.

The effect of the Coulomb hole is to redistribute the electron density and results in the zero change to the electronic density over all space:

$$\int H_c(\vec{r}_1, \vec{r}_2)\, d\vec{r}_2 = 0 \qquad (2.36)$$

This is because the Coulomb hole is independent of the electronic spin and thus does not change the chance of finding the electron over all space. The Coulomb hole is

strongly negative around the space of the reference electron (where the electrostatic interaction is largest) and becomes positive further away from the reference electron. This has the effect of delocalising electrons.

2.4.3 The Kohn-Sham orbitals and their meaning.

The contribution of Kohn and Sham (KS) in 1965 was to conjecture that the basis of the poor kinetic energy in DFT originated from a deficiency in the Thomas Fermi model. Their solution was to construct the electronic density from a fictitious, non-interacting reference system made of orbitals.

$$f^{KS}\varphi = \varepsilon_i\varphi \tag{2.37}$$

Where f^{KS} is the one electron Kohn-Sham operator which includes the kinetic and potential energy required to make this fictitious system replicate the total electronic density of the real system. The Kohn-Sham method uses a single reference determinant to create a set of antisymmetrised non-interacting orbitals, it is a key feature of this method that it allows a method for DFT to reflect the density in equation **2.30**.

The use of one electron orbitals means that the noninteracting kinetic energy recovers the majority of the true kinetic energy and allows the rest to be dealt with in an approximate manner. The result is that the E_{xc} term is slightly modified in the KS description:

$$E_{xc}[\rho] = (T[\rho] - T_s[\rho]) + E_{ncl}[\rho] \tag{2.38}$$

This new exchange correlation term now contains a kinetic term that accounts for the error in the non interacting term $T_s[\rho]$ as well as the non classical interactions $E_{ncl}[\rho]$.

The kinetic energy correction can be described by approximations, the result is that the majority of the kinetic energy is now qualitatively correct. The key advantage of this approach is that the many body problem of the wavefunction has now been split from one function of 30 parameters (in the case of 10 electrons) to 10 equations of 3 parameters.

2.4.4 Parameterisation of the exchange correlation.

The E_{xc} functional contains all the terms that remain unknown and picking a form that describes the interactions has led to an array of functionals (colloquially known as the 'ZOO' of functionals).[37] Because the exchange and correlation term are separate it is trivial to create permutations of functionals. The major question that remains in DFT is how to describe the exchange-correlation term, there are many different, increasingly sophisticated, methods to describe this unknown functional. Methods generally start by looking at the local spin density and are corrected for the gradient of the electronic density. Some deficiency was found to occur still at this level based on the long range self-interaction of electrons, this led to the mixing in of a portion of HF exchange. More recently there has been work to add the kinetic energy gradient and range-separated hybrids.[38] Some more exotic DFT methods have also been devised to account for static correlation such as CAS-DFT.[39]

2.4.5 The local density approximation.

The basis of all the functionals used in this work is the homogeneous electron gas (HEG) introduced by Thomas and Fermi in 1927 and reintroduced by Kohn and Sham.[40] The combination of KS theory and HEG gives rise to the local density approximation (LDA).

$$E_{xc}^{LDA}[\rho] = \int \rho(\vec{r})\,(\varepsilon_x(\rho(\vec{r})) + \varepsilon_c(\rho(\vec{r})) \tag{2.39}$$

The LDA finds the exchange correlation of a particle at $\vec{r}$ multiplied by the density of electrons in that space. This means that the exchange-correlation is a function of the density in the space $\vec{r}$. The exchange term takes the form[41]

$$E_x^{LDA}[\rho] = -\frac{3}{4}\left(\frac{3}{\pi}\right)^{1/3} \int (\rho(\vec{r}))^{4/3} \tag{2.40}$$

This is Slater's exchange term.[42] The correlation term was computed using quantum Monte Carlo in 1980 by Alder.[43] The LDA can be extended to account for spin polarisation relatively simply by separating the α and β density and operating on them independently, creating the local spin density approximation (LDSA). This is the situation for a perfect bulk metal with smeared nuclear charge and is successful in materials science, but the LDA alone does not find common use in quantum chemistry.

2.4.6 The Generalised Gradient Approximation (GGA).

The first correction to this approximate model is to account for the fact that the electrons do not move in a homogeneous positive environment, the point charges of the nuclei create areas where the electron density varies quickly, leading to the HEG breaking down. The initial attempt to account for the inhomogeneity of the density was to introduce the gradient of the electronic density in the gradient expansion approximation (GEA), where it was found that the LDA was only the first term in a Taylor expansion of the gradient terms.

$$E_{xc}^{GGA}[\rho] = \int \rho(\vec{r})\,\varepsilon_{xc}(\rho(\vec{r})\,\nabla\rho(\vec{r})) \tag{2.41}$$

where $\nabla\rho(\vec{r})$ is the gradient dependence of the density at $\vec{r}$. **2.41** shows a simplified GGA exchange-correlation term that neglects spin. The GEA was found to perform worse than the LDA because it violated the conditions in equation **2.35** and **2.36**.[44] This is corrected by imposing cut-offs that truncate the range errors of the functional. Thus by using the gradient we are able to take the density at a point and infer some information about the non-local environment.

2.4.7 The self interaction problem.

The general gradient approximation reaches chemical accuracy (chapter 8.6 of Cramer's book[45] provides an overview), however there is an issue with GGAs tending to overestimate the electronic interaction, resulting in density that is too diffuse. This originates in the local nature of DFT exchange. The issue arises in the classical interaction term $J[\rho]$ of the electronic interaction, to be correct there must be an exact cancellation of this term to reduce the electron self interaction:

$$0 = \frac{1}{2}\int\int \frac{\rho(\vec{r}_1)\rho(\vec{r}_2)}{r_{12}} d\vec{r}_1 d\vec{r}_2 - E_{xc}[\rho] \qquad (2.42)$$

Thus the interaction of an electron with its own density should be cancelled by the exchange correlation functional, however this is upheld for the one electron case in a few functionals (PKZB and TPSS).

HF theory's exchange is non local and exactly cancels any Coulomb self interaction as it depends on the electron over all space. DFT treats exchange as a local feature and thus it is not able to account for the self-interaction problem and the electrons interact with themselves in an unphysical way. Treating this condition has become the obsession of modern DFT.

2.4.8 The Hybrid functional.

One method of solving the issue of the long range self interaction was to turn to the situation where the solution is known, HF theory. By mixing in a degree of HF exchange[46] we are able to reduce the self interaction until a desired empirical accuracy is achieved. This is done at the expense of having to evaluate the exchange integrals, but is still cheaper than the time required to reach the comparable accuracy with post-HF methods.

$$E_{xc}^{Hybrid} = aE_x^{HF} + (1-a)E_x^{DFT} + E_c^{DFT} \qquad (2.43)$$

The exchange-correlation thus has mixed in a fraction *a* of exact exchange. E_{xc} for the B3LYP functional contains empirically fitted parameters and has the form

$$E_{xc}^{B3LYP} = (1-a)E_x^{LDA} + a\,E_{xc}^{HF} + bE_x^{B88} + cE_c^{LYP} + (1-c)E_c^{LDA} \qquad (2.44)$$

There are three parameters that can be varied in the B3LYP functional, the first term describes the portion of local density exchange and the second term describes the counterpoise HF contribution. The third term describes the Becke 88[47] general gradient correction and the last two terms describe the portion of Lee, Yang and Parr[48] correlation and the LDA correlation contribution. In equation **2.44** *b* = 0.72, c = 0.81 and most importantly the HF exchange has a prefactor of *a* = 0.2. The B3LYP functional thus mixes in 20% HF exchange, whilst the other hybrids focused on in this work, PBE0, mixes in 25% exact exchange. As will be demonstrated later in this work, the inclusion of exact exchange has a profound effect on the quantum chemical interpretation of the wavefunction.

2.4.9 Meta functionals.

To correct the form of the functional in DFT further it is possible to include information from the Laplacian of the local density $\nabla^2\rho(\vec{r})$ into the exchange correlation functional.[49]

$$E_{xc}^{MGGA}[\rho] = \int \rho(\vec{r})\, \varepsilon_{xc}\, (\rho(\vec{r})\, \nabla\rho(\vec{r})\nabla^2\rho(\vec{r})) \tag{2.45}$$

In addition there are corrections for the kinetic energy of the Kohn-Sham orbitals though this kinetic energy density.

2.4.10 Choice of functionals.

It is not possible to use all the functionals available instead we select a subset of well tested, commonly available, functionals. The majority of which are GGA functionals.

The functionals we have chosen with the Becke[47] exchange term are the BLYP[48] functional, the BP86[50] and the BPW91[51,52,53] functional. We also use the PBE[54] functional of Perdew and the OLYP[55,56] functional of Handy.

For hybrid functionals we have chosen the B3LYP[57] functional and the PBE0[58] functional because they allow for direct comparison to their pure GGA analogues.

There are three meta-functionals used in this work as they represent the forefront of DFT methods that are readily available in quantum chemical codes. The first is the meta-GGA TPSS functional by Tao *et al*.[59] The second two are the meta-GGA M06-L[60] and the meta-hybrid M06[61], both come from the Minnesota family of functionals parameterised in the Truhlar group.

2.4.11 The DFT grid.

The two electron integrals in DFT are not normally solvable using analytic methods

as is done in HF theory, instead they are usually evaluated using a numerical quadrature which can be selected depending on a desired accuracy. DFT uses atom centred, radially expanding, grids that are most dense closest to the nucleus where there is the most electron density. Each radial shell has a number of angular points selected according to the property of interest.

$$E_{xc}[\rho] = \int \rho(\vec{r})\ \varepsilon_{xc}\left(\rho(\vec{r})\right) \approx \sum_{I}^{grid} W_I \rho(R_I)\ \varepsilon_{xc}\left(\rho\left(\overrightarrow{R_I}\right)\right) \tag{2.46}$$

where the grid coordinates are at R_I and W_I are the weights of the grid. The issue with this approach is that it introduces numerical noise into calculations and this is still an area of active research.[62] Due to this work being focused on transition metals and properties that are on the spectroscopic energy scale (~1cm^{-1} = 4.5×10^{-6} Hartree) we have chosen highly dense grids, especially for the metal.

It is possible to perform DFT calculations without numerical grids[63], but most quantum codes do not have such methods implemented.

2.4.12 The limits of DFT.

Whilst DFT has had tremendous success in most applications, its implementations are nearly always empirically tuned and often parameterised against experimental data sets. Because of the dependence on a subset of properties and molecules it is unlikely that this approach will generate the universal functional, but the wide variety of functionals means that it may be possible to find one that is accurate for magnetic properties such as the ZFS.

Another problem occurs in situations where single determinant methods are not able to correctly calculate properties. In modern quantum chemistry such systems fall under the realm of *ab initio* multi-configurational techniques that we describe in the next

section (**2.5**). Because DFT has been proven to have the potential to be exact it must be possible to replicate multi-configurational character via a single determinant, however the form that the functional must take to achieve this remains unknown.

2.4.13 The broken symmetry approach.

The electronic density should reflect the molecular symmetry of a system, this means that the electronic configuration of a state will generally be described by a set of spatially symmetric orbitals. However this becomes an issue in single determinant DFT as it has insufficient flexibility to find lower energy solutions. In certain cases it can be advantageous to create a wavefunction that breaks the molecular symmetry in order to obtain a better final energy. One such situation is the exchange coupling between spin states. Taking a metal homonuclear dimer as an example, there exist multiple possible spin states that can be the ground state, usually either a high spin ferromagnetic state (where spins on the metals align), or an antiferromagnetic low-spin state (where the spins on the metals anti-align). Standard DFT tends to fail at calculating the energy separation between these states, often calculating the symmetric low spin state to be too high in energy. The solution to this came from Noodleman[64], where we obtain the following expression for J

$$\mathrm{E_{BS}} - \mathrm{E_{HS}} = 2\mathrm{S_1S_2J} \qquad (2.47)$$

Where the broken symmetry E_{BS} solution is a configuration of orbitals that localises the spin to different atoms, the localised spin maximises the exchange terms and thus results in this state being lower in energy than a symmetrically correct solution. The reason that this solution is not found in the initial SCF despite being variationally lower in energy is that there is no impetus for the spin density to localise. Although this

method recovers a portion of multi-configurational character it causes much greater spin polarisation than the corresponding symmetric spin state. To form a broken symmetry solution one has first to calculate the high spin state and then use this to start the lower spin state, the details as how to accomplish this vary, but inspection of the resulting density is necessary to make sure that a true broken symmetry solution is found.

2.5 Multi-configuration techniques

2.5.1 The break down of the single determinant approximation.

The HF equations provide a one determinant solution that is appropriate to equilibrium systems with no degeneracy. However, many chemical situations arise when the true state may only be describable as a linear combination of determinants. Such cases are called multi-configurational wavefunctions and are characterised as having static correlation, meaning correlation that is not related to the Coulombic limitation of the mean-field approximation. Situations that are characterised by static correlation are bond dissociations, rotations of certain functional groups where the HOMO and LUMO become degenerate and metal systems where the d and f orbitals enable charge transfer states (the case this work is concerned with). The contribution of multiple determinants to the ground state means that a set of orbitals must be variationally adjusted to incorporate the effect of all the determinants. This area of quantum chemistry comes under the umbrella of multi-configurational self consistent field procedures (MCSCF), of these methods the simplest is the Complete Active Space Self Consistent Field (CASSCF)[65,66], which is the focus of Kremer's dimer in chapter 5.

2.5.2 The complete active space self consistent field technique.

The CASSCF method involves a selection of orbitals that are expected to contribute to the multi-configurational character of a system and then creating all possible configurations that could occur within these orbitals. There are three types of orbitals in a CASSCF, the core orbitals that have a frozen configuration, the active orbitals that can take any configuration of a defined multiplicity and the virtual orbitals which remain unoccupied during the SCF.

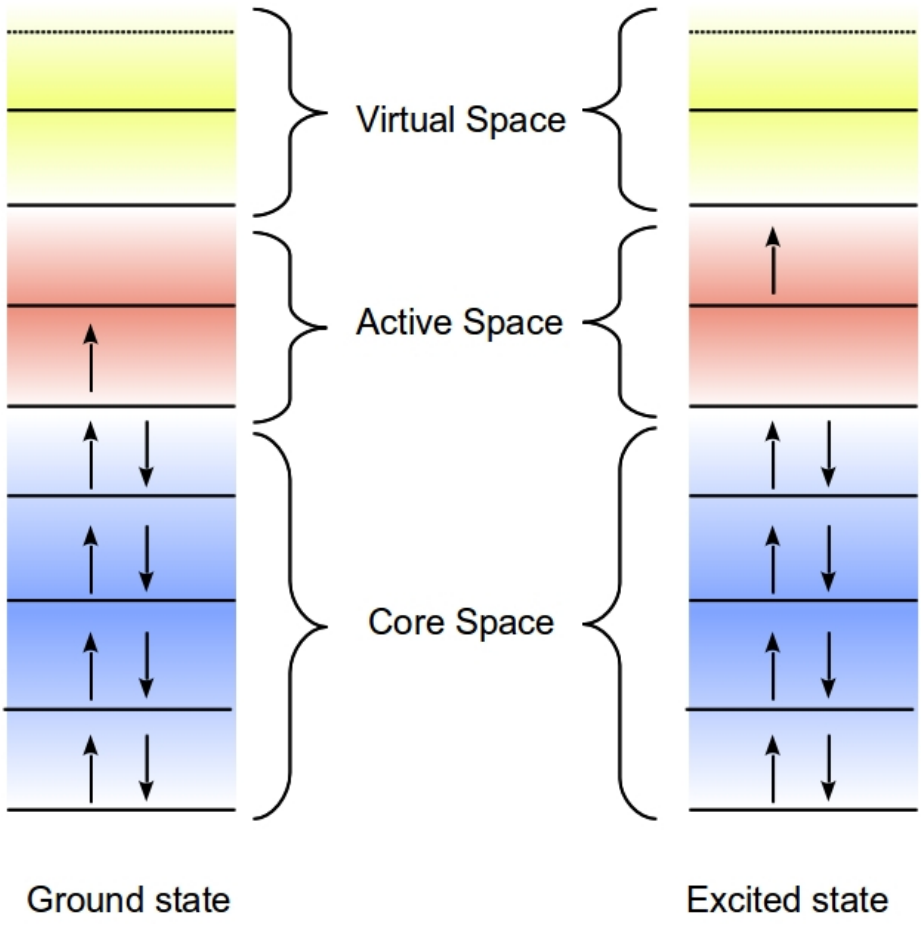

Figure 4: Pictorial representation of a CASSCF active space. For both a ground state determinant and an excited state.

Because multiple configurations contribute to the active space the orbitals can have non integer occupancies.

$$\Psi_A = \sum_N^{\infty} \psi_N C_N^A \tag{2.48}$$

For state A the CASSCF wavefunction is composed of *N* determinants that are electronic permutations within the active space. Determinants are only one choice of function with which to build the active space, another is the configuration state function (CSF) which is a symmetry adapted function that remains a spin eigenfunction, CSFs are linear combinations of Slater determinants.

The Hamiltonian in CASSCF is written in second quantised form[67]

$$\hat{H} = \sum_{p,q} h_{pq} \hat{E}_{pq} + \frac{1}{2} \sum_{p,q,r,s} (pq|rs)\left(\hat{E}_{pq}\hat{E}_{rs} - \delta_{qr}\hat{E}_{ps}\right) \tag{2.49}$$

The first term contains the usual one electron Hamiltonian modified by $\hat{E}_{pq}$, which is a excitation operator:

$$\hat{E}_{pq} = \sum_{\sigma=\alpha,\beta} \hat{a}_{p\sigma}^{+} \hat{a}_{q\sigma} \tag{2.50}$$

This unitary group operator is constructed from the creation and annihilation operator. In this case this unitary operator is an excitation operator moving the electron in orbital q into orbital p. The second term in equation **2.49** is the two electron integral (*pq*|*rs*) followed by two unitary excitation operators and their anticommutation product δ_{qr}. The energy of the CASSCF Ψ_A state from equation **2.49** is thus:

$$E_A = \langle \Psi_A | \hat{H} | \Psi_A \rangle = \sum_{pq} \langle \varphi_p | \hat{h} | \varphi_q \rangle \gamma_{pq}^A + \sum_{pqrs} (pq|rs)\ \Gamma_{pqrs}^A \tag{2.51}$$

Where γ^{A}_{pq} is the first order reduced density matrix and Γ^{A}_{pqrs} is the second order reduced density matrix. The CI coefficients C^{A}_{M} of these reduced density matrices can be respectively expressed as:

$$\gamma^{A}_{pq} = \sum_{MN} C^{A}_{M} C^{A}_{N} \gamma^{A}_{pq} \tag{2.52}$$

$$\Gamma^{A}_{pq} = \sum_{MN} C^{A}_{M} C^{A}_{N} \Gamma^{A}_{pqrs} \tag{2.53}$$

Where γ^{A}_{pq} describes the coupling between any two determinants under E_{pq} and Γ^{A}_{pqrs} describes the coupling between any two determinants through $\hat{E}_{pq}\hat{E}_{rs} - \delta_{qr}\hat{E}_{ps}$. From this the orbitals φ and CI coefficients C^{A}_{M} are varied until the energy of the system in minimised.

2.5.3 Weyl's formula

The number of possible configurations in a CASSCF is far smaller than the binomial seen in equation **2.25** because of the restriction that is placed on the acceptable configurations. The permutations are dependent on the spin *S* of the systems as well as the number of orbitals *M* and electrons *N* in the active space. To calculate the number of configurations Weyl's formula is used[68]:

$$N_{CSF} = \frac{2S+1}{M+1}\binom{M+1}{N/2-S}\binom{M+1}{N/2+S+1} \tag{2.54}$$

Thus we arrive at the number of configurations that are included in the CASSCF active space. The CASSCF calculation is defined by the following notation; a 6 electron

in 10 orbital active space would be a CASSCF(6,10) and the number of configurations depends on the multiplicity of the system. For example for S=0 the number of configurations of a CASSCF(6,10) is 4950, a CASSCF(6,20) is 379,050 and a CASSCF(6,30) is 4,562,425. Thus a careful selection of active space is critically important in running efficient and economic calculations.

2.5.4 Maintaining spin eigenfunctions.

Configuration state functions are symmetry adapted linear combinations of determinants, their main advantage over determinants is that they are spin eigenfunctions and help to reduce the CI expansion. They are built by selecting determinants that are of a particular configuration and combining them so they become spin eigenfunctions.

$$\Psi = \sum_{M} C_M \psi_M \tag{2.55}$$

Where ψ_m are sets of excited configurations and C_M is the coefficient of the contribution of that determinant to the CSF. A review of the different methods to form CSFs is given in McWeeny and Sutcliffe.[69]

2.6 Basis sets

2.6.1 Gaussian functions

To solve the Roothan equation a set of functions must be selected from which to form a basis. The most obvious solution is the hydrogenic orbitals from the direct solution of the one electron Schrödinger equation, however they are difficult to work with programmatically. A simpler option is Slater orbitals, which have their radial component modified to a simpler form that removes the nodes in the radial component. The most common type of function used is the Gaussian function, these introduce a further simplification to the radial term that has the form.

$$g(r) = N\, x^i\, y^j\, z^k\, e^{-\alpha r^2} \tag{2.56}$$

where *N* is a normalisation constant, α is known as the orbital exponent and *i j* and *k* describe the form of the function, i.e if it is s p d or f type. Despite the simplicity of Gaussians they have the advantage that a product rule can be applied to them, which vastly reduces their computational expense when computing integrals.[70]

2.6.2 Contracted functions

The loss of the nuclear cusp and an increased radial decay from the r^2 term in the exponent means that the Gaussian functions do not represent the radial hydrogenic orbitals well, to recover a portion of the hydrogenic shape Gaussians are contracted into groups which are expressed as a series of contraction coefficients that determine their weighting to the total product Gaussian. The coefficients remain the same during the calculation, so that each contracted set of functions has only one entry in the C matrix of the Roothan equation. This gives rise to the *Slater Type Orbitals N Gaussian* (STO-NG) basis type where *N* is the number of functions that are included in the contraction, these

are considered minimal bases as there are only enough functions to contain the required number of electrons. An improvement over minimal basis sets is to describe each orbital with a series of functions, each of which is included in the C matrix and thus has its contribution varied throughout the SCF. These multi zeta functions are labelled according to how many functions are used to describe each orbital.

2.6.3 Split valence basis sets.

A compromise between the expense of multi zeta functions and minimal basis sets is the split valence basis set where the number of independent functions is larger in the valence region and the core region is made up of sets of contracted functions. These basis sets are the most commonly used in quantum chemistry as they allow the SCF variation freedom to lower the energy of the valence region. The famous Pople[71] type basis sets are of this type and are defined according to their split of functions. For instance the 6-31G basis[72] on carbon uses 6 contracted functions for the 1s orbital and then for the valence 2s and 2p orbitals uses two functions, one made of 3 contracted functions and one made of a single primitive, totalling 10 primitive Gaussian functions or 3 contracted functions. The contracted functions proportions are directly varied as the coefficients making up the molecular orbitals. The basis sets in this work usually are of the split valence type of Schaefer and Ahlrichs[73,74,75] such as SVP TZVP and QZVP, where SV stands for split valence (two primitives) polarisation and TZVP stands for triple zeta valence polarisation, etc.

2.6.4 Polarisation functions

An improvement of the split valence basis sets is the inclusion of functions with higher angular momentum than the functions needed in the minimal set[76], for example adding p type orbitals to hydrogen or d type orbitals to carbon. Doing this provides an

additional variational degree of freedom to the SCF and can significantly lower the energy of molecular systems.

Basis	Hydrogen	Carbon, Oxygen, Nitrogen	3d metal
SVP	(4s,1p)/[2s,1p]	(7s,4p,1d) /[3s,2p,1d]	(14s,9p,5d,1f)/[5s,3p,2d,1f]
TZVP	(5s,1p)/[3s,1p]	(11s,6p2d,1f)/[5s,3p,2d,1f]	(17s,11p,7d,1f)/[6s,4p,4d,1f]
QZVP			(24s,18p,9d,3f,1g)/[11s,6p,5d,3f,1g]

Table 1: The number of primitives in the round brackets and the number of contracted functions in square brackets []

From Table 1 it can be seen that the main group elements gain f type polarisation functions with the TZVP basis and the 3d metal gains g type functions with the QZVP basis. The addition of these functions is important to the ZFS as they provide variational freedom to the valence region, where the ZFS occurs.

2.6.5 Decontraction of a basis set.

This work makes use of a decontracted QZVP basis on the metal centres, decontraction involves the separation of the sets of contracted functions allowing each function to be independently varied in the SCF. So for the 3d metal [11s,6p,5d,3f,1g] → [24s,18p,9d,3f,1g]. This greatly increases the number of functions on the metal and represents the number of primitives going from 84 to 153, each of which is independently varied in forming the MOs.

2.6.6 Auxiliary basis sets and the resolution of the identity approximation.

A common method of accelerating calculations is to introduce an auxiliary basis in order to break apart the 4 centre two electron integrals into sets of three centre two electron integrals. Often this is done with a specially constructed set of auxiliary

functions, but can also be auto constructed from the decontracted form of the main basis set. It is important to stress that this method has the potential to be exact as long as the auxiliary basis is infinite. The use of truncated auxiliary basis sets leads to a small (0.1mEh) error in the energy.[77] The forms of the integrals in the resolution of the identity (RI) approximation are[78]:

$$(pq|rs) = \sum_{KL} (pq|K)(K|L)^{-1}(L|rs) \tag{2.57}$$

$$(pq|K) = \int\int \frac{\varphi_p^*(r)\varphi_q(r)K(r')}{|r - r'|} \tag{2.58}$$

where the integral is now over three indexes rather than 4. (K|L) is the overlap of the two auxiliary functions.[79]

2.7 Relativistic theory in chemistry.

2.7.1 The special theory of relativity and the 1s electron.

Einstein's formulation of special relativity can be written for a free particle in motion as

$$H = (m^2c^4 + p^2c^2)^{1/2} \tag{2.59}$$

Trying to marry this with the time dependent Schrödinger equation results in

$$H^2\Psi = (m^2c^4 + p^2c^2)\Psi = -\bar{h}^2\ \partial^2/\ \partial t^2\ \Psi \tag{2.60}$$

To avoid time variance of the density Dirac factorised the square of the operator and tried to solve the linear factors of the square root.

$$[c\alpha \cdot (p + eA/c) - e\phi + \beta mc^2]\Psi = i\bar{h}\ \partial/\ \partial t\,\Psi \qquad (2.61)$$

Equation **2.61** represents the fully relativistic Hamiltonian of fermionic particles. The square brackets contain the terms necessary to describe the Dirac Hamiltonian, the α and β terms are operators that act on the spin space of the particle. These operators are further decomposed into a set of 4 matrices that comprise the Pauli spin matrices. The operation of these matrices necessitates a 4 component wavefunction.

$$\Psi_4 = \begin{pmatrix} \Psi_1 \\ \Psi_2 \\ \Psi_3 \\ \Psi_4 \end{pmatrix} = \begin{pmatrix} \Psi_S \\ \Psi_L \end{pmatrix} \qquad (2.62)$$

It is usual to eliminate the small component as it corresponds to the positronic states. Such eliminations go back to before the proof of the Dirac equation to work by Pauli.[80]

2.7.2 The Dirac equation and the origin of spin.

Elimination of the small terms is done through looking at the relativistic limits of the Dirac equation, resulting in the small component being 2-4 orders of magnitude smaller than the large component depending on the nuclear charge.[81] The separation of the large and small components eventually leads to the following relativistic Hamiltonian.

$$\left(\frac{p^2}{2m} - \frac{Ze^2}{4\pi r} - \frac{p^4}{8m^3c^2} + \frac{Ze^2\vec{L}\cdot\vec{S}}{8\pi m^2c^2r^3} + \frac{Ze^2\bar{h}^2}{8m^2c^2}\delta^3(\vec{r})\right)\Psi = E\Psi \qquad (2.63)$$

The first two terms in **2.63** are the normal terms seen in the Schrödinger equation, the

kinetic and potential energy. The third term introduces a relativistic mass velocity correction to the kinetic term (hence its m^3c^2 dependence), this term is treated using the Zero Order Regular Approximation (ZORA) in this work. The 4th term couples the electron's angular momentum terms and is the origin of the spin orbit coupling. The mechanism of this interaction is through the various degrees of motion of the charged particle, each of which generates a magnetic field that slightly perturbs the energy of the electron. The final term is the Darwin term, primarily a correction to the s-type orbitals that is not independently considered in this work.

2.7.3 The zero order regular approximation.

In this work we test the kinetic relativistic correction in order to quantify the effect of the contraction of the s electrons.[82] This effect is expected to be minor for the 3d metals due to their low nuclear charge (and hence potential), but its quantification is important when moving to the heavier elements. The ZORA method in this work is the scalar relativistic version and neglects the spin orbit terms[83] that we later introduce with perturbation theory. The spin orbit correction in the ZORA would not account for the state mixing needed in the ZFS and it is not variationally stable.

$$h_{ZORA} = v - \vec{p}\frac{c^2}{2c^2 - V}\vec{p} \tag{2.64}$$

The form of the ZORA used with this work is the spin free version implemented in ORCA, which involves a model potential for V according to van Wüllen.[84] This is based on a potential:

$$\tilde{V}_{model} = -\sum_A \frac{Z_a}{|r - R_A|} + \int \frac{\rho_{model}(r')}{|r - r'|} dr' + V_{xc}^{LDA}[\rho_{model}] \tag{2.65}$$

The van Wüllen ZORA potential is constructed from a simplified spherical density around each atom, comprised from a series of s type Gaussians. These single atom densities are summed and then V_{ee} and V_{xc}^{LDA} is evaluated over the entire molecule. Once the model potential has been constructed it can easily be interfaced with the normal Kohn-Sham one electron kinetic term in the following way.

$$\langle \phi_\mu | \hat{T}_{ZORA} | \phi_\nu \rangle = \langle \phi_\mu | \hat{T} | \phi_\nu \rangle + \int \left\{ \nabla \phi_\mu^*(r) \frac{\tilde{V}(r)}{2c^2 - \tilde{V}(r)} \nabla \phi_\nu(r) \right\} \qquad (2.66)$$

Thus with this method a model calculation is performed with the ZORA formalism, then the SCF procedure is started and the ZORA model potential is used to adjust the one-electron matrix elements. This model potential does not depend on the Kohn-Sham orbitals used in the SCF and means that the model potential only needs to be calculated once during the set up on the SCF and not during each cycle. A clear advantage of this model for this work is that it can be used in the spin free form and it allows us to apply relativistic components independently of each other.

2.7.4 Effect of the scalar relativistic correction on a basis set.

The effect of the relativistic scalar correction imparted by the ZORA potential is that electrons in the region close to the nucleus experience a relativistic mass increase that contracts their orbits.

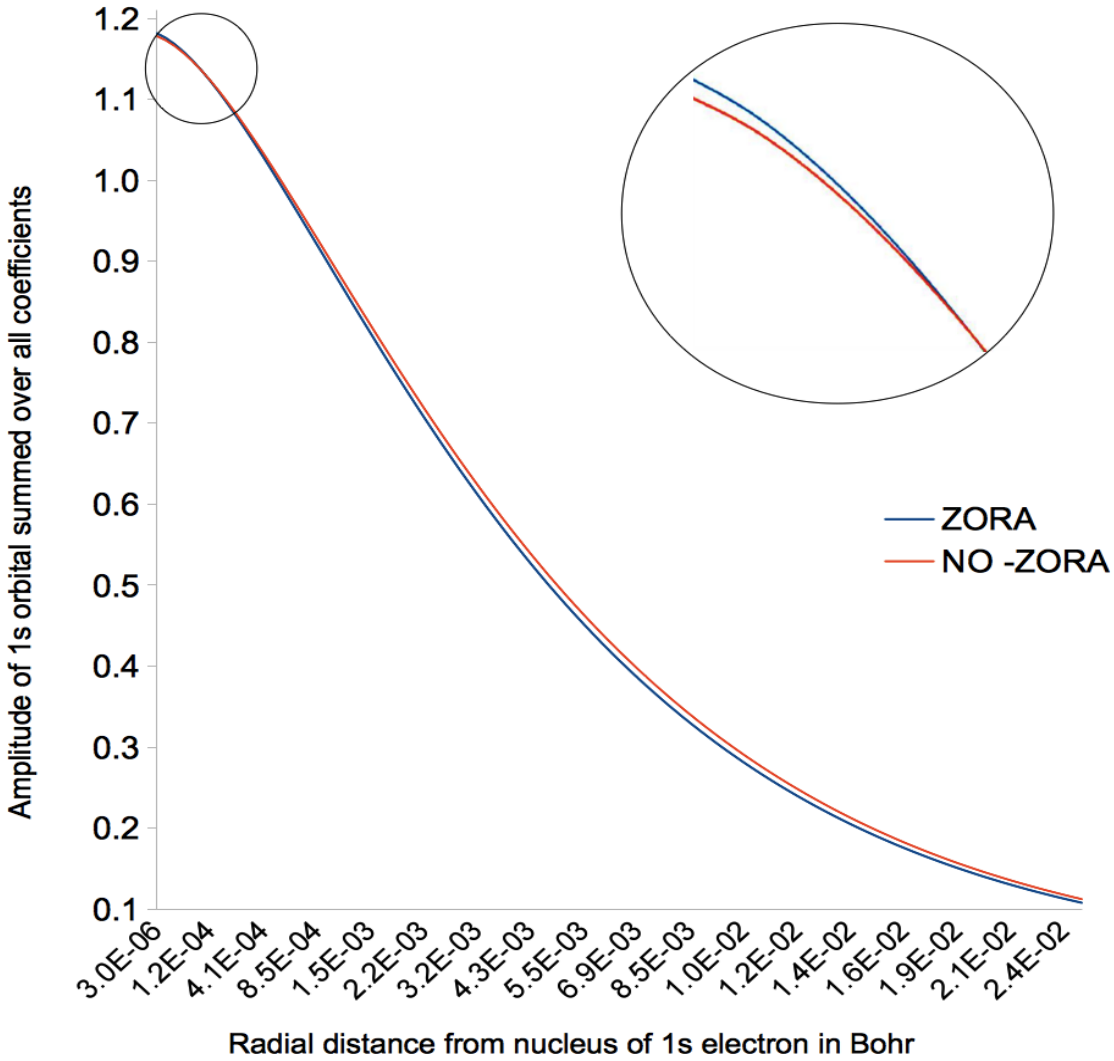

Figure 5: The radial amplitude of the 1s orbital of the Fe atom in the decontracted QZVP basis calculated at B3LYP.

The illustrative example in Figure 5 shows the nuclear region of iron to have a slightly elevated probability amplitude, whilst the region further from the nucleus has reduced probability amplitude. The Figure highlights a minute relativistic change for iron. This will, in turn, affect the orbitals higher up in the manifold. A similar effect is the origin of the coloration of gold.

2.8 Spin in chemistry

2.8.1 Electron paramagnetic resonance.

EPR[85] is the electronic analogue of nuclear magnetic resonance (NMR). The two phenomena are observed independently because the magnetic moment of the electron is 600 times larger[86] than that of a proton. In EPR a magnetic field is swept in strength across a sample in a microwave cavity. This external field interacts with the field of all the electrons. These fields emanate from the coupling of the various types of angular momenta. If the electron field is aligned with the external field then its energy is lowered, if it is anti-aligned then its energy is raised according to the Zeeman splitting.

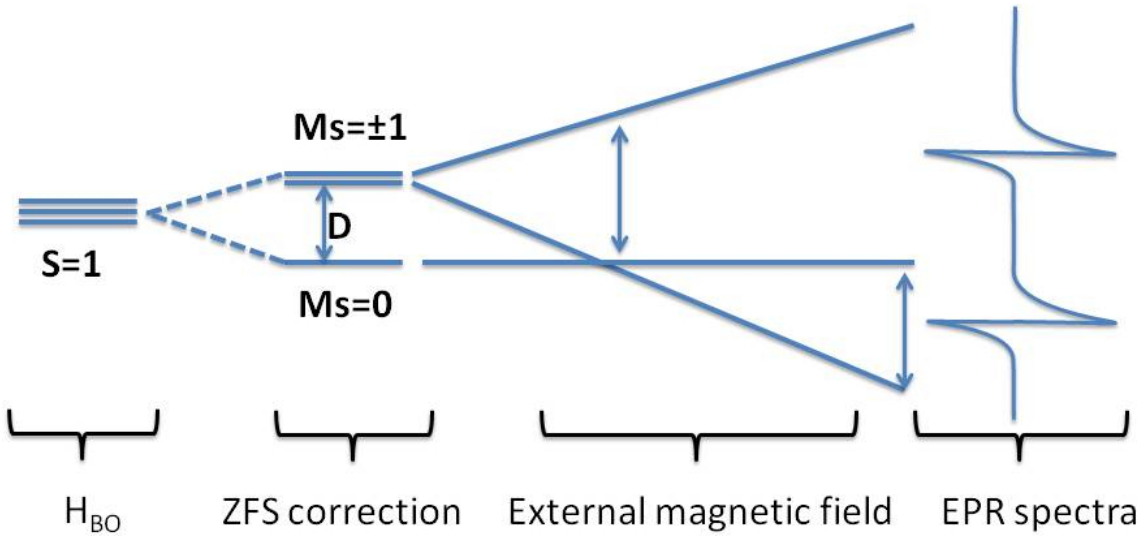

Figure 6: A diagram of electronic splitting relating HBO and ZFS correction to the EPR spectra.

The spectrometer accesses this splitting using a fixed frequency microwave beam that excites the electron from being in one spin orientation into its opposite spin orientation, this can only occur for unpaired electrons due to the Pauli principle. Because the photon is of a fixed energy, as the field sweeps different transitions occur and from this, information on the local electronic environment is observed. Several factors cause the electron to couple with its molecular environment, if any nuclei have a non-zero spin then they interact with the electron and further split the electronic energy levels. This phenomenon is called hyperfine coupling. The electron is additionally

affected by its **g** value, which in matrix form describes the strength of the coupling of the electron to the external field along each spatial axis. This factor is dependent on the molecular symmetry through the spin density. The remaining contribution in EPR occurs when there are multiple unpaired electrons, such as in di-radicals or metal-containing systems. This is the ZFS and is the focus of this work.

2.8.2 The phenomenological spin-Hamiltonian

EPR makes use of a phenomenological spin Hamiltonian[87] in order to avoid the cost of solving the full Schrödinger equation. The spin Hamiltonian contracts the normal spatial (non-spin dependent) terms into tuneable parameters and results in a Hamiltonian that contains spin operators acting on a spin space. In practice the spin Hamiltonian is used to reproduce the spectra that are seen in EPR by careful tuning of parameters according to chemical knowledge. The spin Hamiltonian acts on a truncated Hilbert space that includes only spin variables:

$$\hat{H}_s|S, M_s\rangle = E\,|S, M_s\rangle \tag{2.67}$$

This Hamiltonian is able to calculate the relative splitting between energy levels due to spin related phenomena qualitatively, but is not able to quantitatively determine electronic energy levels as is done in the Born Oppenheimer Hamiltonian. The Hamiltonian has the form[88,89]:

$$\begin{aligned}\hat{H}_s = \hat{S}D\hat{S} + \beta B g \hat{S} + \sum_A \left[\hat{S}A^{(A)}\hat{I}^{(A)} + \beta_N B g_N^{(A)}\hat{I}^{(A)} + \hat{I}^{(A)}Q^{(A)}\hat{I}^{(A)}\right] \\ + \sum_{i<j}\left[\hat{S}^{(i)}J^{(ij)}\hat{S}^{(j)}\right]\end{aligned} \tag{2.68}$$

The Spin Hamiltonian is composed of several terms that depend on the spin of the

electrons $\hat{S}$ and the spin of the nuclei $\hat{I}$. The first term in equation **2.68** describes the ZFS and the second term the **g** matrix. The third term sums over all the nuclear spin interactions such as the hyperfine A, the nuclear-field interaction and the quadrapole Q. The final term is the spin-spin exchange coupling.

2.8.3 Experimental observation of ZFS.

ZFS[90] was originally discovered in 1958 in naphthalene di-radicals, however interest in the phenomenon has rapidly increased over the last two decades since the discovery of the first SMM.[91] In molecules with multiply unpaired electrons each electron generates a magnetic field dependent on its environment and the intersection of these fields along each axis causes a magnetic perturbation of the energy levels. ZFS occurs independently of the external field and if strong can break the degeneracy of the M_s levels enough to prevent any observable EPR transitions, to de-convolute such situations either high frequency EPR is needed or zero-field EPR.[92]

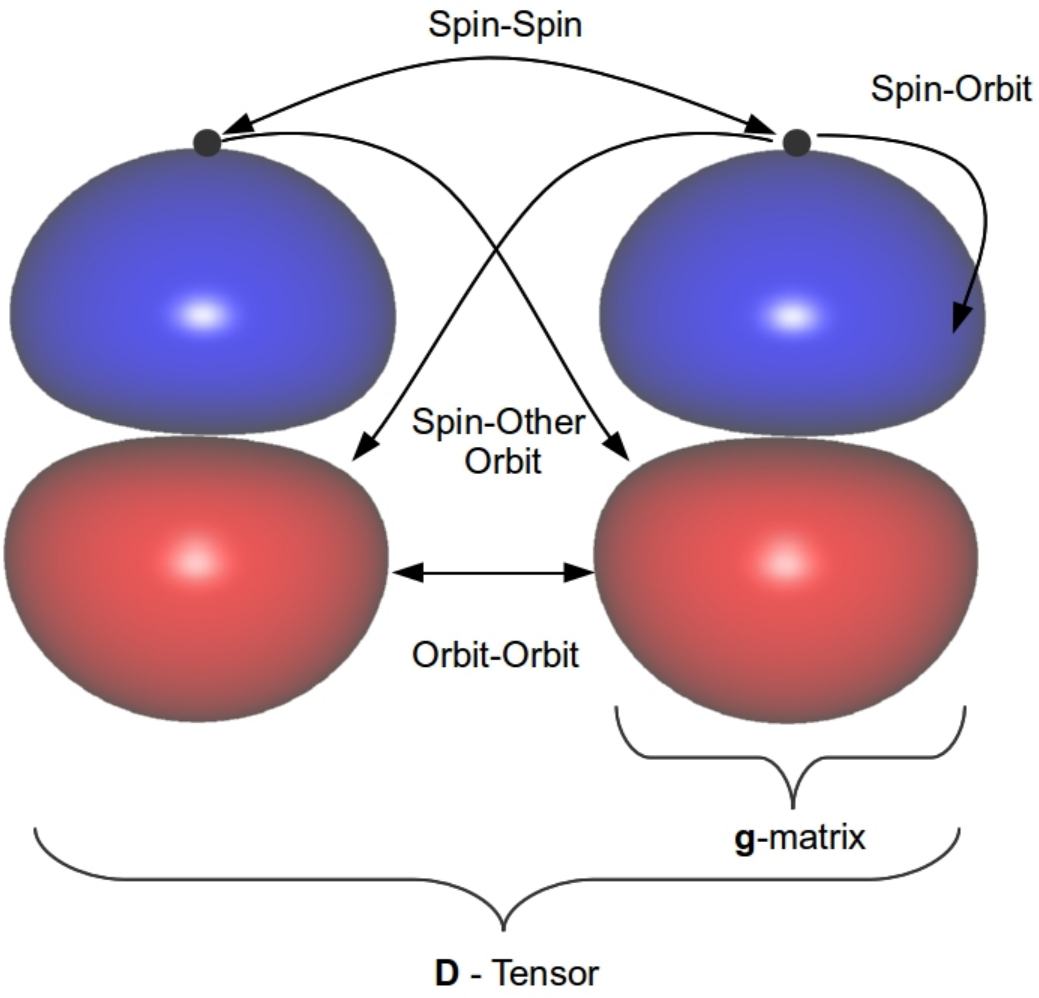

Figure 7: Cartoon of possible interactions between two electrons, with a fictitious point of spin at the top of the orbitals added for clarity.

The ZFS comprises more than the direct dipolar interaction between spins, it describes all of the possible interactions between all unpaired electrons through their magnetic fields. Each form of angular motion that an electron possesses generates a magnetic field and each of these interacts with the other unpaired electrons in the environment. For computational convenience it is common to separate these into dipolar terms and spin-orbit terms.

2.8.4 The origin of ZFS and the use of tensors.

The matrix form of the ZFS Hamiltonian is

$$\mathrm{H_{ZFS}} = \hat{\mathrm{S}}\mathrm{D}\hat{\mathrm{S}} = \begin{pmatrix} \mathrm{S_z} & \mathrm{S_y} & \mathrm{S_x} \end{pmatrix} \begin{pmatrix} \mathrm{D_{ZZ}} & \mathrm{D_{zy}} & \mathrm{D_{zx}} \\ \mathrm{D_{yz}} & \mathrm{D_{yy}} & \mathrm{D_{yx}} \\ \mathrm{D_{xz}} & \mathrm{D_{xy}} & \mathrm{D_{xx}} \end{pmatrix} \begin{pmatrix} \mathrm{S_z} \\ \mathrm{S_y} \\ \mathrm{S_x} \end{pmatrix} \tag{2.69}$$

When **D** is diagonalised it is equivalent to finding a coordinate system where the splitting is maximised. In this diagonal form $\mathrm{H_{ZFS}}$ becomes

$$\mathrm{H_{ZFS}} = \overline{\mathrm{D}}\left(\hat{\mathrm{S}}_\mathrm{z}^2 - \frac{1}{3}(\mathrm{S}(\mathrm{S}+1))\right) + \overline{\mathrm{E}}\left(\hat{\mathrm{S}}_\mathrm{x}^2 + \hat{\mathrm{S}}_\mathrm{y}^2\right) \tag{2.70}$$

Once the 9 component **D** tensor has been diagonalised ($\overline{\mathrm{D}}$) there are three elements for *D* which are collected into two values:

$$\overline{\mathrm{D}} = \overline{\mathrm{D}}_{\mathrm{ZZ}} - \frac{1}{2}(\overline{\mathrm{D}}_{\mathrm{XX}} + \overline{\mathrm{D}}_{\mathrm{YY}}) \tag{2.71}$$

Which describes the axial contribution to the ZFS and is the important factor in the construction of SMMs. *D* is defined by the direction with the largest degree of splitting and according to **2.70** it assigned the axis of *Sz*. Along this axis the energy levels all split according to the Zeeman interaction. Because *Sx*, *Sy* and *Sz* do not commute along other axes the Zeeman splitting becomes distorted and all the M_s levels have components that can interact with the external field.

A second factor that arises from the $\mathrm{H_{ZFS}}$ is the rhombic splitting *E*, this occurs as an additional breaking of the sublevel degeneracy within each M_s state providing the system is of integer total spin (non-Kramer type systems).

$$\overline{E} = \frac{1}{2}(\overline{D}_{XX} + \overline{D}_{YY}) \tag{2.72}$$

E is half the splitting between the M_s = +1/-1 levels, it should not be observed for transitions within higher spin states due to the conservation of angular momentum of the photon, although an exception occurs when the external field is weak giving rise to a half field phenomenon.[93] E describes the splitting perpendicular to the major axis of quantisation and is termed the rhombic splitting. The axes of *D* are assigned to so that:

$$|D_z| > |D_y| > |D_x| \tag{2.73}$$

Often *E* is not provided, instead the *E/D* ratio is given as the rhombicity. The rhombicity describes the degree of the anisotropy in the molecule. It is defined as being $0<E/D<1/3$, when it reaches its 1/3 limit it describes a system where all the sub levels are split equally, rendering the sign of *D* irrelevant.

2.8.5 Perturbation theory.

To correct the H_{BO} wavefunctions with magnetic terms there are two possible routes, either variationally or via a perturbative technique. In this work the focus is on perturbative techniques, where there is an assumption that the majority of the physics is captured by a zero order wavefunction, this wavefunction can then be adjusted with a small correction for the term of interest.

$$H = \hat{H}_0 + \hat{H}_1 \tag{2.74}$$

An alternative method is to calculate the additional terms variationally within the SCF, this method has been more applied to the calculation of the *g* value by Neese who

states that this method may be applicable to the ZFS[94].

2.8.5.1 The spin-spin contribution.

The first order contribution to the ZFS is the spin-spin contribution, this represents the explicit interactions of the ground state spin density. The form used in this work for DFT is based on the formula[95,96]

$$D_{KL}^{ss} = \frac{1}{2}\frac{\alpha^2}{S(2S-1)} \times \left\langle OSS \left| \sum_i \sum_{j \neq i} \frac{r_{ij}^2 \delta_{KL} - 3(r_{ij})_K (r_{ij})_L}{r_{ij}^5} \{2\hat{S}_{zi}\hat{S}_{zj} - \hat{S}_{xi}\hat{S}_{xj} - \hat{S}_{yi}\hat{S}_{yj}\} \right| OSS \right\rangle \quad (2.75)$$

This equation links the radial distance between two electrons r_{ij} to their spin vectors $\hat{S}_i$ along the x y and z axis. The first term's denominator becomes zero when S < 1 and this enforces the requirement for multiple unpaired electrons for the ZFS. The r_{ij}^5 denominator is reduced to $\sim r_{ij}^3$ due to its numerator. The final part in the {} brackets describes all possible direct spin couplings of any two electrons.

2.8.5.2 The spin-orbit contribution.

The second order contribution to the ZFS is the spin-orbit contribution There are three components to the spin orbit coupling that must be accounted for, the discussion here is largely based on the description of Harriman.[97] All the operators contribute to the form of

$$\hat{H}^{so} = i\beta^2 \sum_j H_j' \cdot S_j \quad (2.76)$$

Each electron's orbital components H_j' are coupled along each spin axis. The major component of the spin-orbit coupling is the one electron spin-orbit term:

$$\widehat{H}^{so} = -g_e' \sum_v Z_v \, K_0^2(r_{jv}) \frac{r_{jv} \times \nabla_j}{r_{jv}^3} \tag{2.77}$$

This is the direct coupling of electron *j* with its angular momentum ∇_j respective to nucleus *v*. The spin-other orbit terms are the interaction of electron *j* with the field generated by the orbit of electron *k* (∇_k).

$$\widehat{H}^{soo} = 4 \sum_{k(\neq j)} \frac{(r_k - r_j) \times \nabla_k}{r_{jk}^3} \tag{2.78}$$

An electron-electron spin-orbit term describes coupling interactions of two electrons by their orbital angular moment.

$$\widehat{H}^{eeso} = g_e' \sum_v \frac{(r_j - k_j) \times \nabla_j}{r_{jk}^3} \tag{2.79}$$

The last two operators are commonly combined into a single "spin-other orbit" Hamiltonian. The spin-orbit terms are thus a collection of Hamiltonians that describe the possible magnetic interactions that can occur between electrons, dependent on orbital angular momenta.

2.8.5.3 The spin-orbit mean field operator

In the method implemented in ORCA, the last two terms are collected and the resultant spin-orbit Hamiltonian is divided into one and two electron components.[98]

$$\hat{H}_{SOC}^{(1)} = \frac{\alpha^2}{2} \sum_i \sum_A Z_A r_{iA}^{-3} \hat{L}_{iA} \hat{s}_i \tag{2.80}$$

$$\hat{H}_{SOC}^{(2)} = -\frac{\alpha^2}{2} \sum_i \sum_{j \neq i} r_{ij}^{-3} \hat{L}_{ij} \left(\hat{s}_i + 2\hat{s}_j \right) \tag{2.81}$$

This is the Bret Pauli spin orbit operator. Two electron terms can be treated by the mean field approximation of Hess *et al*,[99] which has been shown to be accurate for g values.[100]

$$\begin{aligned} \langle \varphi_\mu | \hat{z}_k^{SOMF} | \varphi_\upsilon \rangle = \; & \langle \varphi_\mu | \hat{h}_k^{1el-SO} | \varphi_\upsilon \rangle + \\ & \left[\sum_{\kappa\tau} P_{\kappa\tau} \left(\varphi_\mu \varphi_\nu \right| \hat{g}_k^{SO} | \varphi_\kappa \varphi_\tau \right) \\ & - \frac{3}{2} \left(\varphi_\mu \varphi_\kappa | \hat{g}_k^{SO} | \varphi_\tau \varphi_\nu \right) - \frac{3}{2} \left(\varphi_\tau \varphi_\nu | \hat{g}_k^{SO} | \varphi_\mu \varphi_\kappa \right) \Big] \end{aligned} \tag{2.82}$$

The first term in equation **2.82** describes the one electron spin orbit interaction. The second term describes a mean field Coulomb interaction between two electrons, followed by two exchange terms. The 1 electron coupling Hamiltonian is:

$$\hat{g}_k^{SO} = -\frac{\alpha^2}{2} \hat{L}_{ij} r_{iA}^{-3} \tag{2.83}$$

The two electron coupling Hamiltonian is:

$$\hat{h}_k^{1el-SO} = -\frac{\alpha^2}{2}\sum_i\sum_A Z_A r_{iA}^{-3}\hat{L}_{iA;k} \tag{2.84}$$

In ORCA there are additional approximations added to this technique, such as simplifying the first two electron Coulomb integral with the RI approximation. The final two terms are approximated by one-centre terms (1X, for 1 centre exchange) and they are much smaller than the Coulomb term.

2.8.5.4 The Pederson-Khanna method.

The first method we consider is the Pederson-Khanna method[101] (PK),

$$
\begin{aligned}
D_{kl}^{SOC} = &-\frac{1}{4S^2}\sum_{i_\beta,a_\beta}\frac{\left\langle\psi_i^\beta\middle|h_k^{SOC}\middle|\psi_a^\beta\right\rangle\left\langle\psi_a^\beta\middle|h_l^{SOC}\middle|\psi_i^\beta\right\rangle}{\varepsilon_a^\beta-\varepsilon_i^\beta}\\
&+\frac{1}{4S^2}\sum_{i_\alpha,a_\alpha}\frac{\left\langle\psi_i^\alpha\middle|h_k^{SOC}\middle|\psi_a^\alpha\right\rangle\left\langle\psi_a^\alpha\middle|h_l^{SOC}\middle|\psi_i^\alpha\right\rangle}{\varepsilon_a^\alpha-\varepsilon_i^\alpha}\\
&-\frac{1}{4S^2}\sum_{i_\alpha,a_\beta}\frac{\left\langle\psi_i^\alpha\middle|h_k^{SOC}\middle|\psi_a^\beta\right\rangle\left\langle\psi_a^\beta\middle|h_l^{SOC}\middle|\psi_i^\alpha\right\rangle}{\varepsilon_a^\beta-\varepsilon_i^\alpha}\\
&-\frac{1}{4S^2}\sum_{i_\beta,a_\alpha}\frac{\left\langle\psi_i^\beta\middle|h_k^{SOC}\middle|\psi_a^\alpha\right\rangle\left\langle\psi_a^\alpha\middle|h_l^{SOC}\middle|\psi_i^\beta\right\rangle}{\varepsilon_a^\alpha-\varepsilon_i^\beta}
\end{aligned}
\tag{2.85}
$$

From this method there are 4 distinct classes of configurations that are included in the perturbation, the first two describe the transition of an electron that does not change the spin ($\Delta S=0$) $\alpha \rightarrow \alpha$ transition $\beta \rightarrow \beta$. The second two terms are 'Spin flip'[102] transitions where electrons change spin. The linear response of the wavefunction to each perturbation is contained in the second *bracket* and denominator.[103]

$$
\text{Linear response of wavefunction} = U_{ai} = \frac{\left\langle\psi_a'^\alpha\middle|h_l^{SOC}\middle|\psi_i'^\beta\right\rangle}{\varepsilon_a^\alpha-\varepsilon_i^\beta} \tag{2.86}
$$

where $\psi_a'^\alpha$ is the perturbed set of orbitals. The program of this method is to determine the matrix elements between different states according to the spin orbit coupling and then determine the change of the wavefunction to this perturbation.

2.8.5.5 The quasi-restricted orbit method.

In 1998 Neese and Solomon derived equations for ZFS using arguments based on the Spin Hamiltonian using the Clebsch-Gordan Coefficients. From this they worked out sum over state equations for the ZFS that include the ΔS=+/-1 transitions

$$
\begin{aligned}
D_{kl}^{SOC-(0)} &= -\frac{1}{S^2}\sum_{b(S_b=S)}\Delta_b^{-1} \\
&\times\left\langle 0SS\left|\sum_i h_k^{SO}(i)s_{i,z}\right|bSS\right\rangle \\
&\times\left\langle bSS\left|\sum_i h_l^{SO}(i)s_{i,z}\right|0SS\right\rangle \\
D_{kl}^{SOC-1} &= -\frac{1}{S(2S-1)}\sum_{b(S_b=S-1)}\Delta_b^{-1} \\
&\times\left\langle 0SS\left|\sum_i h_k^{SO}(i)s_{i,+1}\right|bS-1S-1\right\rangle \\
&\times\left\langle bS-1S-1\left|\sum_i h_l^{SO}(i)s_{si,-1}\right|0SS\right\rangle \\
D_{kl}^{SOC-(+1)} &= -\frac{1}{(S+1)(2S+1)}\sum_{b(S_b=S+1)}\Delta_b^{-1} \\
&\times\left\langle 0SS\left|\sum_i h_k^{SO}(i)s_{i,-1}\right|bS+1S+1\right\rangle \\
&\times\left\langle bS+1S+1\left|\sum_i h_l^{SO}(i)s_{i,+1}\right|0SS\right\rangle
\end{aligned}
\tag{2.87}
$$

This expression calculates all the possible state interactions that are important to the ZFS. $D_{kl}^{SOC-(0)}$ describes the two electron interaction of the reference state $|0SS\rangle$ with another state of the same multiplicity $|bSS\rangle$ along each set of Cartesian components $(K, L \in x, y, z)$. $D_{kl}^{SOC-(-1)}$describes states where an $\alpha \rightarrow \beta$ transition occurs. The final equation is the sum over states for the $\beta \rightarrow \alpha$ transitions (usually ligand transfer states).

The Δ_b^{-1} term is the energy difference between these states. The other novel component of these equations is that the spin prefactors change with the multiplicity, a feature absent from the PK method.

In a 2006 paper Neese[102] reworked the ZFS equations for use with quasi-restricted orbitals in order to regain states that are spin eigenfunctions, this is opposed to the unrestricted form of Pederson and Khanna. He achieved this by diagonalisation of the density matrix to form the UNOs and using the occupation of these orbitals to diagonalise the α and β Fock matrices. This set of quasi-restricted orbitals (QROs) is used to form excited determinants in a form reminiscent of a CI expansion, it very closely reflects the transition classes described in the PK method, resulting in equations of the form.

$$
\begin{aligned}
D_{kl}^{SOC} = &-\frac{1}{4S^2}\sum_{i,p}\frac{\left\langle\psi_i\middle|h_k^{SOC}\middle|\psi_p\right\rangle\left\langle\psi_p\middle|h_l^{SOC}\middle|\psi_i\right\rangle}{\varepsilon_p^{\beta}-\varepsilon_i^{\beta}} \\
&-\frac{1}{4S^2}\sum_{p,a}\frac{\left\langle\psi_p\middle|h_k^{SOC}\middle|\psi_a\right\rangle\left\langle\psi_a\middle|h_l^{SOC}\middle|\psi_p\right\rangle}{\varepsilon_a^{\alpha}-\varepsilon_p^{\alpha}} \\
&+\frac{1}{4}\frac{1}{S(2S-1)}\sum_{p\neq q}\frac{\left\langle\psi_p\middle|h_k^{SOC}\middle|\psi_q\right\rangle\left\langle\psi_q\middle|h_l^{SOC}\middle|\psi_a\right\rangle}{\varepsilon_q^{\beta}-\varepsilon_p^{\alpha}} \\
&+\frac{1}{2}\frac{1}{(S+1)(2S+1)}\sum_{i,a}\frac{\left\langle\psi_i\middle|h_k^{SOC}\middle|\psi_a\right\rangle\left\langle\psi_a\middle|h_l^{SOC}\middle|\psi_i\right\rangle}{\varepsilon_a^{\alpha}-\varepsilon_i^{\beta}}
\end{aligned}
\tag{2.88}
$$

where

$$\begin{gathered} i = \text{Doubly occupied orbital} \\ p = \text{Singly occupied orbital} \\ q = \text{Distinct singly occupied orbital} \\ a = \text{Virtual orbital} \\ \varepsilon = \text{Orbital energy} \end{gathered} \tag{2.89}$$

The QRO method is a limited set of excitations and does not include the ability to account for the linear response of the exact exchange. Because this method is a perturbative approach based on configuration interaction arguments, it is not applicable when there is significant spin polarisation. A further limitation is that the final term that describes DOMO → VIRTUAL is missing several types of excitation and is scaled by a factor of two compared to the other excitations. van Wüllen showed that the neglect of these excitations causes errors when including molecular cofactors such as anions or glassing materials[103]. The term QRO is used to represent both the orbital truncation and the response equations, in this work it shall refer to the ZFS perturbative method unless otherwise stated.

2.8.5.6 The coupled perturbed method.

A further development came from Neese who connected the perturbation approach to analytical derivatives as is done for a variety of properties such as dipole moments, polarisabilities and vibrational frequencies. The basis of this reasoning is that perturbation parameters can be expanded as a collection of derivatives

$$E_N = E_0 + \lambda^1 E_1 + \lambda^2 E_2 \ldots\ldots = E_0 + \lambda \frac{d^1 E_1}{d\lambda} + \lambda^2 \frac{d^2 E_2}{d\lambda^2} \ldots\ldots \tag{2.90}$$

where λ is the perturbation parameter that can be taken to infinite order. Because the

SOC is a second order perturbation the series is truncated to the second derivative. The SOC is a spin dependent parameter and the perturbation acts on the spin density of the system which has the form $P_{\mu\nu}^{(m)} = \left\langle 0SS \middle| \hat{S}_{\mu\nu}^{(m)} \middle| 0SS \right\rangle$, where $\hat{S}_{\mu\nu}^{(m)}$ is the spin operator for a given spin state. This means that when m=0 then it is the ground state spin, when -1 is the spin of an $\beta \rightarrow \alpha$ transition state and +1 is for an $\alpha \rightarrow \beta$ electron transition. The perturbation for the coupled-perturbed (CP) method is $x_K^{(m)}$ where m is the spin state with respect to the ground state (0, +/-1). By describing the effect of spin-orbit coupling as the change of the spin-density, a clear connection is made with the ZFS, which can be viewed as a magnetic distortion of the spin-density that originates from the magnetic interaction of electrons. The coupled equations use the following relations:

$$\frac{\partial E}{\partial x_K^{(m)}} = \sum_{\mu\nu} h_K^{SOC} P_{\mu\nu}^{(m)}$$
$$\frac{\partial^2 E}{\partial x_K^{(m)} \partial x_L^{(\Delta m)}} = \sum_{\mu\nu} h_K^{SOC} \frac{\partial P_{\mu\nu}^{(0)}}{\partial x_L^{(\Delta m)}} \tag{2.91}$$

The change of energy with respect to the first order perturbation is separated into spatial components h_k^{SOC} and the spin components $P_{\mu\nu}^{(m)}$. The second order energy change is the change of the spin-density with respect to the coupling of the excited state spin-orbit interaction.

$$
\begin{aligned}
D_{KL}^{SOC\,(0)} &= -\frac{1}{4S^2}\sum_{\mu\nu}\frac{\partial P_{\mu\nu}^{(0)}}{\partial x_L^{(0)}}\left(\mu\left|h_K^{SOC}\right|\nu\right)D_{KL}^{SOC(-1)} \\
&= -\frac{1}{2S(2S-1)}\sum_{\mu\nu}\frac{\partial P_{\mu\nu}^{(0)}}{\partial x_L^{(-1)}}\left(\mu\left|h_K^{SOC}\right|\nu\right)D_{KL}^{SOC(+1)} \\
&= -\frac{1}{2(S+1)(2S+1)}\sum_{\mu\nu}\frac{\partial P_{\mu\nu}^{(0)}}{\partial x_L^{(+1)}}\left(\mu\left|h_K^{SOC}\right|\nu\right)
\end{aligned}
\tag{2.92}
$$

The ZFS contribution is found by calculating the derivative of the ground state spin-density components with respect to a perturbation that describes the coupling by the spin-orbit operator. For example the contribution of +1 states is calculated from the ground state density ($P_{\mu\nu}^{(0)}$) coupling with the perturbation of the spin orbit terms emanating from all the +1 states.

For exact electronic structure calculations this method is as exact as taking an infinite sum over states. During his derivation Neese argues that this method is computationally a more manageable route. A key benefit of this method is that it allows the calculation of properties even with exact exchange. Neese further showed that the PK methods can be reformulated within the derivative framework and other than the spin prefactors, is equivalent. Van Wüllen[103] improved this method further by creating a single sum-over-states term for the ZFS in order to remove problems with nearby closed shell molecules, however this improvement has not yet been included in ORCA. All the calculations in this work are done without counter ions or co-molecules, so we expect any difference between the two methods to be small in our case.

2.8.5.7 Quasi degenerate perturbation theory.

Because DFT is a ground state property it is not clear that it is the correct framework from which to get accurate ZFS value. Furthermore because of the limitation of current functionals in multi-configurational situations it becomes attractive to turn to full multi-configurational techniques. In these methods normal perturbative corrections break down as the energy difference between states becomes zero.

$$\left\langle \psi_I^{SM} \middle| \widehat{H}^{BO} + \widehat{H}^{SOC} \middle| \psi_J^{SM'} \right\rangle = \delta_{IJ}\delta_{SS'}\delta_{MM'}E_I^{(S)} + \left\langle \psi_I^{SM} \middle| \widehat{H}^{SOC} \middle| \psi_J^{SM'} \right\rangle \qquad (2.93)$$

This technique relies on first generating the diagonalised interactions between states using the H_{BO} operator ($\delta_{IJ}\delta_{SS'}\delta_{MM'}E_I^{(S)}$), then calculating their matrix elements under spin orbit coupling and finally diagonalising the resulting matrix to gain the perturbed energy levels. This method has the advantage that it can calculate the SOC for any starting state provided that it is input as a spin-eigenfunction.

2.9 Population analysis.

2.9.1 The Mulliken populations analysis.

A key issue in interpreting quantum chemical calculations is the disconnect between chemically intuitive concepts and the values which result from quantum chemical calculations. Many methods exist to extract properties such as charges and bond strengths from calculations, however all are based on the concept of partitioning the wavefunction in ways that do not correspond to any observable. In this work we use standard population analysis techniques to describe charges and bond orders with the aim of creating a useful description of the effect of different functionals. The most common approach for studying atomic charges is Mulliken population analysis. This method is based on using only the orbital coefficients and the overlap matrix for the molecular orbitals. Mulliken population analysis looks at the overlap between orbitals on adjacent atomic centres and weights their contribution according to the electronic density. Mulliken population analysis makes the assumption that atomic orbitals remain a valid concept from which to partition molecular orbitals.

$$Q_A = Z_A - \sum_{\mu \in A} P_{\mu\mu} - \sum_{\mu \in A} \sum_{\mu \neq \upsilon} (PS)_{\mu\upsilon} \qquad (2.94)$$

The Mulliken charge Q for atomic centre A with a nuclear charge Z is shown in Equation **2.94**. The overlap of all the functions μ centred on A is compared with those functions centred on other atoms ν. **P** is the density matrix and **S** is the overlap matrix. During the work of this thesis an effort was made to replace the Mulliken approach with a custom programmed Roby operator, but this method was found not to be as generally applicable due to a reliance on using a minimal basis set.

2.9.2 The Mayer bond order.

An extension to this method is the Mayer bond order[104], which provides a measure of orbital overlap between two basis centres.

$$B_{AB} = \sum_{\upsilon \in B} \sum_{\mu \in A} (PS)_{\mu\upsilon}(PS)_{\upsilon\mu} + (P^{\alpha-\beta}S)_{\mu\upsilon}(P^{\alpha-\beta}S)_{\upsilon\mu} \qquad (2.95)$$

Where the overlap is taken as the sum of the functions summed over two atomic centres.

Chapter 3: Methodology and technical details.

3.1 The version of ORCA

Gaussian 09[105] is not able to calculate the ZFS as it lacks proper spin-orbit coupling treatment (opting for an effective potential method). Gaussian also lacks the ability to calculate electronic spin-spin coupling. To calculate the ZFS we had to use the ORCA computational suite, which includes the three methods of calculating the ZFS we have discussed. All of the monometallic results that we present were initially calculated in ORCA 2.8, which unfortunately carried an error in the computation of the spin-spin interaction. This forced us to recalculate all the results that we present here in ORCA 2.9.

3.2 Methodology of program use and structure preparation.

All of the geometries used in this thesis were crystal structures obtained from the Chemical Database Service[106] using the ConQuest[107] program. The hydrogen positions of the structures were then optimised using Gaussian 09 at the TZVP basis level using BLYP for the monometallic molecules and B3LYP for Kremer's dimer. The hydrogen positions were confirmed to be at a local minimum through the checking that the harmonic frequencies were all real valued. Where possible, comparisons were performed between ORCA and Gaussian final SCF energies to make sure that artificial convergences were avoided.

3.3 Integration grids.

The ZFS is a property bound to the valence region of atoms, it thus can be expected to be strongly affected by certain aspects of computational chemistry, such as the number of valence basis functions and the degree of polarisation. Critically it can be expected that since the ZFS is of the order of 1 cm^{-1} the integration grid is important. To

ensure that a sufficient grid has been selected we performed calculations on Fe^{3+}, which has a d^5 configuration. Because the calculation is of spherical symmetry the magnetic interaction should be found to be isotropic in the d^5 case and thus the *D* and *E/D* should both equal zero. We found that ORCA GRID5 was more than sufficient to result in E/D being 0. We further went beyond this by specifying the metal atoms to have additional radial accuracy of 11. This ensures for the decontracted calculations that the steep functions are fully accounted for.

3.4 The use of QZVP-SVP.

This work uses the notation QZVP-SVP to define a basis set where the metal atom uses a decontracted QZVP and the ligands have a normal SVP basis. This choice was made in order to test both the basis set dependence of the functionals and to ensure that the basis is flexible enough to allow the scalar relativistic corrections to affect the orbitals.

Chapter 4: Single metal molecules.

To test the applicability of DFT with the new methods to calculate the ZFS, we ran a series of calculations on a collection of monometallic molecules in a simple ligand environment. Shown in Table 2 are the molecules that have been studied and the ZFS values along with the source of the crystallographic structure.

Molecule	d orbital occupancy	Experimental Data			
		D / cm^{-1}	E / cm^{-1}	EPR	X-ray
$V(acac)_3$	d^2	+7.47	1.92	[108]	[109]
$Cr(acac)_3$	d^3	±0.59	0.05	[110]	[111]
$Mn(acac)_3$	d^4	-4.52	0.25	[112]	[113]
$Fe(acac)_3$	d^5	-0.14	0.03	[114]	[115]
$[Fe(mal)_3]^{3-}$	d^5	±0.12	0.03	[114]	[116]

Table 2: The experimental zero field splitting and d electron count of the molecules in this study.

The magnetic properties we used for comparison for $V(acac)_3$ were resolved using high frequency EPR at 25T, it is the most anisotropic molecule of this study with a large positive axial splitting of 7.47 cm^{-1}. No previous theoretical studies on the ZFS of this system have been identified in the literature. $Cr(acac)_3$ has been characterised using Q band EPR, and to the best of our knowledge no theoretical calculations have been performed on this system. The magnetic properties of $Mn(acac)_3$ are well studied with a large negative splitting, which serves as a model example of the original SMM ($Mn_{12}O_{12}$).[117] Neese has conducted studies on $Mn(acac)_3$ using a number of theoretical techniques.[102] Several structures of $Mn(acac)_3$ exist, a geometry which includes Jahn-teller distortions and metal to ligand bond lengths close to the structure reported by

Neese was chosen for study in this work. $Fe(acac)_3$ and $[Fe(mal)_3]^{3-}$ were characteriested in the same EPR study using Q and X band EPR. Both molcules can be expected to have similar ZFS properties due to their electronic and structural similarities. The study of the malonate alows for the testing of anionic magnetic marterials, however we have exluded the $[Co(NH_3)_6]^{3+}$ counter ion for computational expediancy. Both of these systems were calculated by Neese in 2009 using the PBE functional where he reported results inline with experiment.[118]

4.1 Vanadium tris-acetylacetonate - $V(acac)_3$.

4.1.1 DFT results.

$V(acac)_3$ is a distorted octahedral molecule with a d^2 electronic configuration. High frequency electron paramagnetic resonance (HFEPR) provides zero field splitting (ZFS) values of $D = 7.27\ cm^{-1}$, $E = 1.92\ cm^{-1}$ and $E/D = 0.264$.

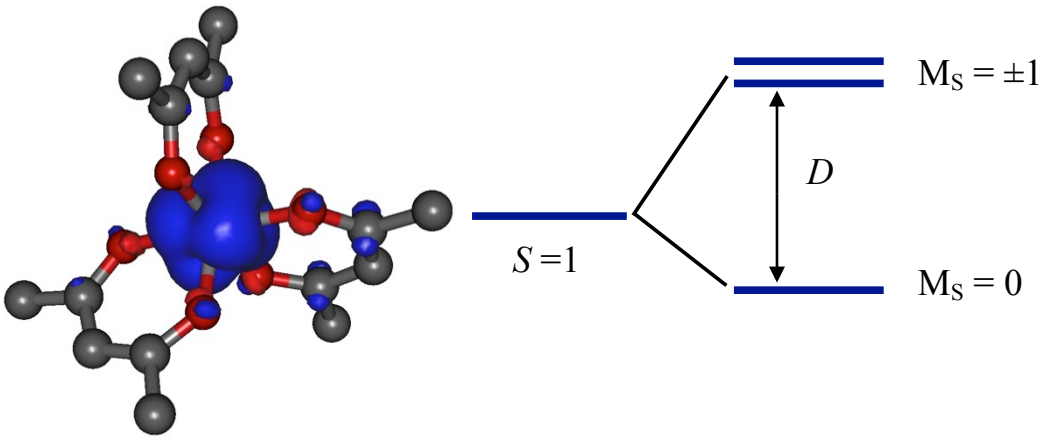

Figure 8: Left: Spin density for $V(acac)_3$ studied at the B3LYP-TZVP level. Isosurface rendered at 0.004 a.u. Right: The splitting diagram from the ZFS Hamiltonian for the triplet state.

To understand the theoretical parameters that strongly influence ZFS we combined seven density functionals with the three orbital response methods available within the ORCA suite.

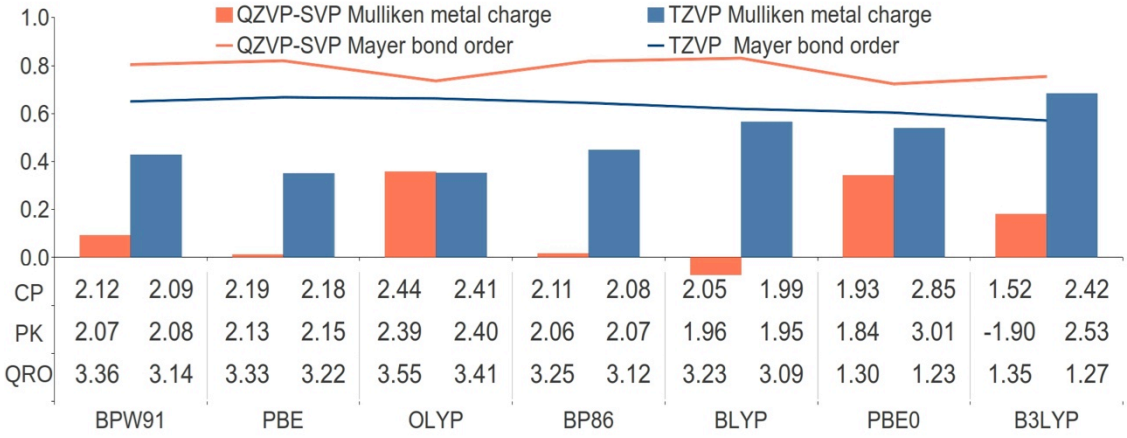

Figure 9: The calculated axial splitting (D cm^{-1}) for seven functionals and three spin orbit response methods in the QZVP-SVP basis on the left hand side columns and the TZVP basis on the right hand side columns. The Mulliken metal charge is represented by bars and the average Mayer bond order of the metal-to-ligand interaction is represented by lines.

The Mulliken charge and Mayer bond orders shown in Figure 9 can be used to represent the covalency of the metal-to-ligand interaction, this chemical region is highly important to the ZFS as it generally describes the extent of the spin density in Figure 8. The QZVP-SVP basis set results in lower Mulliken charges and higher Mayer bond orders than TZVP, although an exception is shown for the Mulliken charge of the OLYP functional. The GGAs are more covalent than the hybrid functionals, this is a well known feature arising from self interaction errors in DFT that cause electron delocalisation. The exact exchange in the hybrids is an attempt to correct this and manifests as increased ionicity. The GGA-QRO combination results in the largest *D* splittings, however with the hybrid functionals the QRO method has the smallest splitting by 2 cm^{-1}. The discrepancy in the performance of the QRO ZFS method is because its formulation lacks certain spin transitions (e.g. β to β transitions) that are required to describe the range of relevant excitations needed in the ZFS.

The GGAs are slightly more accurate with the QZVP-SVP basis, however the accuracy of the hybrids is reduced. The bias of the QZVP-SVP basis on the metal clearly enhances the covalency (self-interaction delocalisation) of the GGAs and

appears to be important for increasing *D*. The difference between the GGA functionals is of the order of 0.2 cm^{-1} for this molecule, whereas the hybrids are less consistent and in the case of B3LYP-PK *D* is found to be negative. The incorrect sign of this calculation originates from the size of its rhombicity (0.29), which is close to the 1/3 limit that renders the sign of *D* irrelevant.

In summary the GGAs with the QZVP-SVP basis are slightly more accurate, but also show a significant saving in the number of basis functions, which drop from 822 for TZVP to 561 for QZVP-SVP.

Additional calculations of the BP86, BLYP, PBE0 and B3LYP functionals were run without the ZORA correction and the *D* splittings were found to vary only by ~ 1% of the relativistic calculations.

4.1.2 Multi-configurational results.

An alternative approach to using DFT with an approximate orbital response method is to utilise multi-configuration *ab initio* techniques with quasi-degenerate perturbation theory (QDPT) to determine the sub-level splitting. This method is more involved in its set-up as it requires specification of configurations with the desired multiplicity and then finding their spin-orbit coupling elements. By using this technique we are able to move away from qualitative DFT considerations to a quantitative discussion of how many determinants are required to reach an arbitrary accuracy. Our initial approach was to follow the methodology of Neese where one averages 5 active d orbitals in the CASSCF from the ground state triplet with the *S*_ (singlet) states. For accurate description of the magnetic corrections it is necessary to correlate the d orbitals, to achieve this we swapped orbitals with significant d coefficients from the virtual space into the active space. It is important to make a distinction between the inclusion of states in the orbital optimisation step and the inclusion of states in the QDPT. We ran

two types of state averaged calculations, one that only included the triplet states in the SCF and a second that introduced singlet states into the SCF. Scalar relativistic corrections were included in the form of the zero-order regular approximation (ZORA). In all three calculations the QDPT included the 10 triplet states and 15 singlet states. The singlet states should be expected to be magnetically inactive.

Number of roots	ZORA	Spin-spin D (cm^{-1})	Spin-orbit D (cm^{-1})	total D (cm^{-1})	total E/D (cm^{-1})
10 triplets 15 singlets	NO	0.6066	-20.74	-20.89	0.09
10 triplets	NO	0.5274	-15.76	-15.88	0.09
10 triplets	YES	0.5770	-19.71	-19.82	0.09

Table 3: Summary of results from the state averaged CASSCF(2,5) at the TZVP level.

The state averaged calculations in Table 3 show the *D* splitting to be more than twice the experimental number of 7.27 cm^{-1}, which is in contrast with the earlier DFT calculations that had *D* splittings too small by over 50%. The large splitting originates from the SOC, which also gives rise to a negative splitting sign in line with experiment. By turning to a more detailed analysis of the energy levels we find some interesting features that highlight some of the limits in quantum chemical calculations. These results are found in an appendix of this chapter.

Restricting the state-averaging to include only the 10 triplet states results in a similarly large *D* of -15.94 cm^{-1}arising from the spin-orbit term. A reduction of 5 cm^{-1} from the earlier SA-CASSCF that included the singlet contributions to the orbitals. *E* is also smaller with a value of 1.57 cm^{-1} and *E/D* is thus 0.11.

The scalar relativistic corrections from ZORA were not found to improve the *D* values. The gap between states A → B increases to 3.9 cm^{-1} and the state B → C gap to -21.73 cm^{-1}

The ORCA suite uses only configurations of the ground state multiplicity when calculating the spin density used in the SSC and we thus do not find that it varies much from 0.6 cm^{-1}, this indicates that including the singlet state configurations does not have much effect on the orbitals.

We conclude the state-averaged results by noting that the overestimation of the splitting by a factor of two is not unreasonable for a calculation with no dynamic correlation and a small active space.

Orbital	90	91	92	93	94
dz^2	17.4	23.7	1.9	32.4	2.8
dxz	11.9	6.9	0.8	16.5	4.9
dyz	7.1	24.9	2.8	27.2	25.1
dx^2-y^2	52.4	40.1	83.8	2.8	1.5
dxy	7.6	1.3	0.5	12.2	30.7
Occupation	1.00	1.00	0	0	0

Table 4: The occupation and coefficients of the d orbitals for a state optimised CASSCF(2,5).

The large *D* values from the SA-CASSCF may indicate that the forcing of multi-configurational character is producing orbitals that are inappropriate for the ZFS. Turning to state-optimised CASSCF(2,5) (SO-CASSCF) wavefunctions, we show in Table 4 that the density is localised to orbitals 90 and 91. This indicates that this molecule is adequately described by a single determinant. By applying QDPT to this wavefunction we find $D = 1.2$ cm^{-1}, $E = 0.12$ cm^{-1} and *E/D* as 0.1. This underestimation of splitting is similar to the earlier DFT results. The spin-spin component of *D* was found to be 0.48 cm^{-1}, which is fairly consistent with the state-averaged CASSCF values found earlier.

4.1.4 Restricted open shell determinants with QDPT.

The lack of electronic density in the virtual orbitals for the state optimised calculation shows that a

minant can adequately describe this molecule. The accuracy of the QRO method with the GGAs shown earlier indicates that using restricted orbitals may be a fruitful avenue of investigation, possibly because it maintains the orbitals as spin eigenfunctions. The orbitals from any restricted open shell calculation can be used with QDPT, providing one rotates the virtual orbitals into a configuration that includes as much d character in the configuration space as possible. In contrast to CASSCF this arrangement results in the QDPT performing a CI on a selected active space without any optimisation of the orbitals.

Basis	Method	Spin-spin D (cm^{-1})	Spin-orbit D (cm^{-1})	Total D (cm^{-1})	Total E/D
TZVP	HF	0.31	0.63	0.86	0.10
QZVP-SVP	HF	0.30	0.63	0.85	0.09
TZVP	PBE0	0.73	1.00	1.69	0.13
QZVP-SVP	PBE0	0.74	1.08	1.78	0.12
TZVP	PBE	0.87	1.19	2.00	0.09
QZVP-SVP	PBE	0.87	1.28	2.11	0.08

Table 5: The QDPT ZFS values from restricted open electronic structure methods.

Table 5 shows the results for the restricted open shell calculations for three electronic structure methods with decreasing amounts of HF exchange. We chose the PBE functional for its fair performance in the earlier DFT results as well as its hybrid analogue PBE0. We also provide results from ROHF calculations to show the effect of

not optimising the virtual orbitals as one would do in a CASSCF.

The *D* splitting becomes smaller as the amount of HF exchange is increased, both for the SOC and SSC terms. The ROHF calculation has the smallest spin-spin *D* splitting, However, we find this calculation to have the largest metal Mulliken spin density (1.95) pointing to a more localised spin than PBE0 (1.85) and PBE (1.64). The smaller *D* value, despite the localised spin, can be rationalised by turning to the SSC rhombicity which we find for ROHF to be ~0.25; compared to PBE at ~0.18. The high rhombicity indicates that the spin is spread over the three axes and thus results in weaker dipolar interaction.

The largest *D* in Table 4 is from RO-PBE and should be comparable to the QRO numbers shown earlier for this functional, however we find it to be 37% smaller than the earlier PBE-QRO results. It is not possible to say if this indicates that the process of forming the QROs from the UNOs is maintaining some desirable orbital character from the original unrestricted calculation or if the QRO-ZFS method's neglect of certain spin transitions is leading to larger splitting magnitudes.

The magnitude of *D* for all methods improves upon using the QZVP-SVP basis. We find a general trend of increasing covalency when going down Table 5 in line with HF exchange decreasing. The *D* from the ROHF calculation is 0.85 cm^{-1}, smaller by ~0.2 cm^{-1} than the earlier SO-CASSCF. This highlights the importance of optimising the weakly occupied orbitals in the CASSCF active space. The virtual orbitals for the ROHF (Table 6) were found to be more delocalised across the molecule (less d orbital centric), as would be expected for uncorrelated orbitals.

Orbitals	90	91	92	93	94
dz^2	11.7	30.4	12.7	-0.3	-0.9
dxz	1.8	17.3	15.8	-0.1	7.0
dyz	15.5	16.7	4.4	29.1	-0.7
dx^2-y^2	69.0	24.5	-0.1	-0.1	11.8
dxy	0.1	8.7	3.9	4.9	12.0
Occupation	1.00	1.00	0	0	0

Table 6: The occupation and coefficients of the d orbitals for the TZVP ROHF method.

4.2 Chromium-tris-acetylacetonate - $Cr(acac)_3$.

The experimental anisotropy values of this molecule are $D = \pm 0.59$ cm^{-1}, $E = 0.05$ cm^{-1} and thus $E/D = 0.085$.

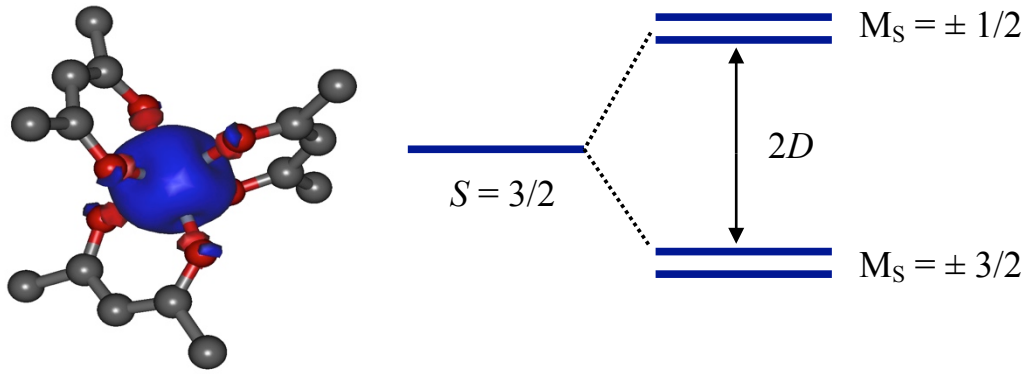

Figure 10: Left: Spin density for $Cr(acac)_3$ studied at the B3LYP-TZVP level. Isosurface rendered at 0.004 a.u. Right: The splitting diagram from the ZFS Hamiltonian for the quartet state, shown for $D < 0$.

4.2.1 DFT results.

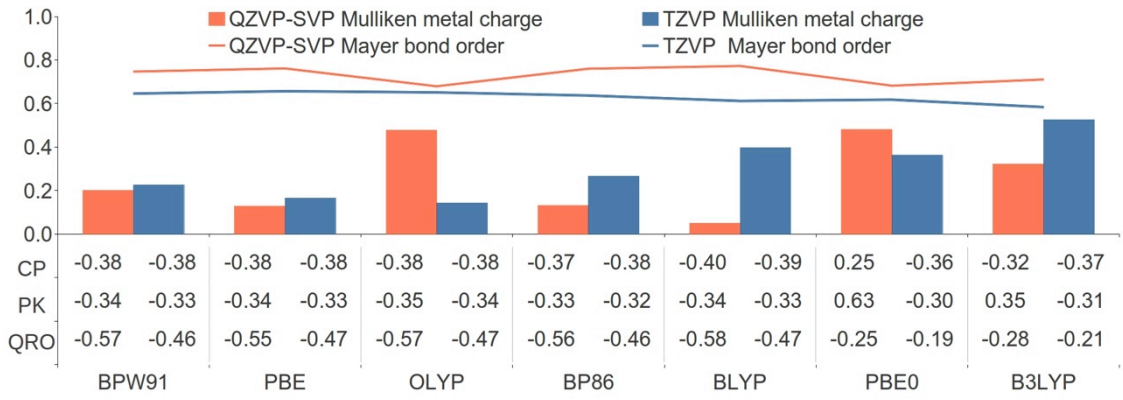

Figure 11: The calculated axial splitting (D cm^{-1}) for seven functionals and three spin orbit response methods in the QZVP-SVP basis on the left hand side columns and the TZVP basis on the right hand side columns. The Mulliken metal charge is represented by bars and the average Mayer bond order of the metal-to-ligand interaction is represented by lines.

For the GGA functionals the QRO ZFS method was found to result in larger D splitting values than the CP and PK methods by ~0.1 cm^{-1}. The hybrids, whereas, were found to be less accurate with this ZFS method by around 0.2 – 0.3 cm^{-1}. The CP method does not vary much across functional or basis set, the only exception being

PBE0 at the QZVP-SVP basis level where it results in a positive sign and a splitting ~0.1 cm^{-1} smaller than the other results with this method. The PK method is similarly invariant across the GGAs, but has positive *D* splitting values with the QZVP-SVP basis set for the hybrids. PBE0 gives a splitting of 0.63 cm^{-1}, this is the only calculation of $Cr(acac)_3$ where *D* is greater than the experimental number. The QRO response is more accurate with the QZVP-SVP basis, by ~0.1 cm^{-1} for the GGA functionals and by ~0.06 cm^{-1} for the hybrid-QRO combination.

The three combinations with positive splitting are PBE0-CP, PBE0-PK and B3LYP-PK, which have the respective rhombicities of 0.3, 0.3 and 0.1. The origin of the rhombicity for PBE0-CP and B3LYP-PK is the spin-spin term, which has a different large axis of splitting to the SOC. The spin-spin term thus contributes heavily to the *E* value and results in the system having rhombic anisotropy. PBE0-PK has a large positive spin orbit term which originates from the PK method having 4 times the pre-factor term for the β to α channel than that of the CP method. All the other functionals calculate *E/D* to be smaller than experiment, giving better agreement with the axial anisotropy.

The QZVP-SVP basis is shown in Figure 11 to produce higher Mayer bond orders than the TZVP basis. The bond order for this basis is lower for the OLYP and PBE0 functionals and this corresponds to the higher Mulliken metal charges. Of all the combinations tested BLYP is the most covalent functional for this molecule and with the QRO method has the most accurate *D* splitting of the DFT data by ~0.01 cm^{-1}. The OLYP-CP, OLYP-PK and PBE0-PK are more accurate with the QZVP-SVP basis and this is despite the metal being described as more ionic. This indicates the decontracted basis to have better flexibility for calculating the ZFS.

4.2.2 Multi-configurational results.

State optimised CASSCF(3,5) calculations at the TZVP basis level were found not to spread density within the active space and indicate a single determinant ground state into the SCF. The splitting values from this calculation are D = -0.27 cm^{-1} and E/D = 0.003, half of the experimental axial splitting. The rhombicity is only 3% of the experimental value but agrees with the anisotropy being generally axial.

Number of roots	ZORA	Spin-spin D (cm^{-1})	Spin-orbit D (cm^{-1})	Total D (cm^{-1})	Total E/D
10 quartet 40 doublet	NO	-0.090	-0.336	-0.425	0.014
10 quartet 40 doublet	YES	-0.090	-0.334	-0.424	0.015
10 quartets	NO	-0.090	-0.341	-0.431	0.015
10 quartets	YES	-0.090	-0.340	-0.430	0.015

Table 7: Summary of results from the state averaged CASSCF at the TZVP level including the population numbers.

In Table 7 we present state averaged CASSCF(3,5) results for orbitals formed from both the quartet ground state and calculations that include the doublet excited states. The spin-spin term consistently contributes 0.09 cm^{-1} to the splitting, this is a result of the spin density being formed exclusively from the quartet states. The spin-orbit contribution is also consistent for these calculations, splitting the sub-levels by -0.43 cm^{-1}. These splitting numbers show that the inclusion of the doublet states in the SCF has little effect on the converged orbitals. Furthermore we find the splitting values are not affected by removing the ZORA relativistic corrections. These state averaged D splitting values are twice the magnitude of the state optimised numbers and also possess a rhombicity in better agreement with experiment.

4.2.3 Restricted open shell determinants with QDPT.

Basis	Method	Spin-spin D (cm^{-1})	Spin-orbit D (cm^{-1})	Total D (cm^{-1})	total E/D
TZVP	HF	-0.09	-0.15	-0.24	0.03
QZVP-SVP	HF	-0.03	-0.05	-0.08	0.07
TZVP	PBE0	-0.31	-0.11	-0.42	0.08
QZVP-SVP	PBE0	-0.10	-0.21	-0.31	0.01
TZVP	PBE	-0.11	0.34	-0.44	0.33
QZVP-SVP	PBE	-0.11	0.36	0.45	0.32

Table 8: The QDPT ZFS values from restricted open electronic structure methods.

Results from restricted open shell determinants with QDPT are shown in Table 8, the results from the TZVP basis ROHF calculation is similar to the earlier state optimised CASSCF values. The small difference can be attributed to these ROHF calculations lacking any optimisation of the unoccupied active orbitals. The PBE-QZVP-SVP combination is the closest to the experimental D value, however this method calculates the system to have rhombic anisotropy and thus results in a positive D value. The PBE functional with the TZVP basis is 0.15 cm^{-1} less than experiment, although the system was again calculated to be rhombic. The flip in the sign of D occurs because of the 0.02 cm^{-1} reduction in the SOC for the QZVP-SVP basis and together with the rhombicity causes the sign to change. PBE0 results in the correct rhombicity and D splitting values that are 0.17 cm^{-1} from experiment, making it the best of the methods in this set.

4.3 Manganese-tris-acetylacetonate - $Mn(acac)_3$.

The experimental results for $Mn(acac)_3$ are D = -4.52 cm^{-1}, E = 0.25 cm^{-1} and thus E/D = 0.055 making the system axial.

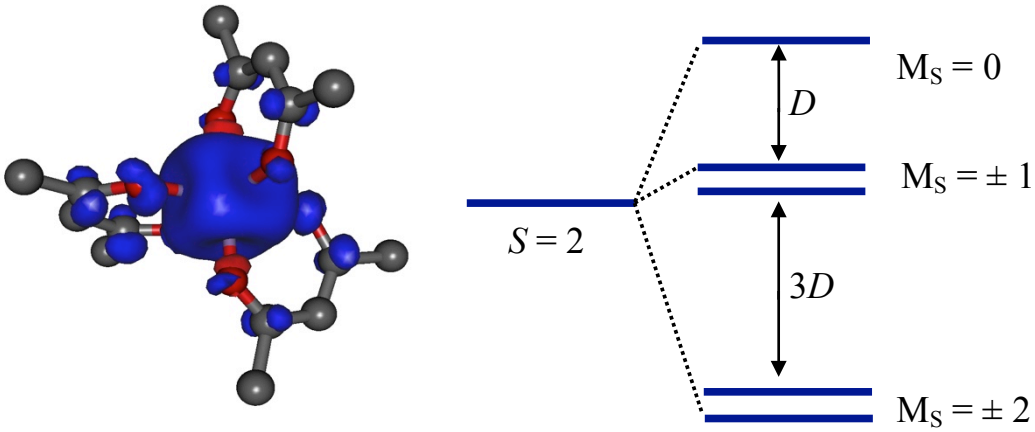

Figure 12: Left: Spin density for $Mn(acac)_3$ studied at the B3LYP-TZVP level. Isosurface rendered at 0.004 a.u. Right: The splitting diagram from the ZFS Hamiltonian for the pentet state.

4.3.1 DFT results.

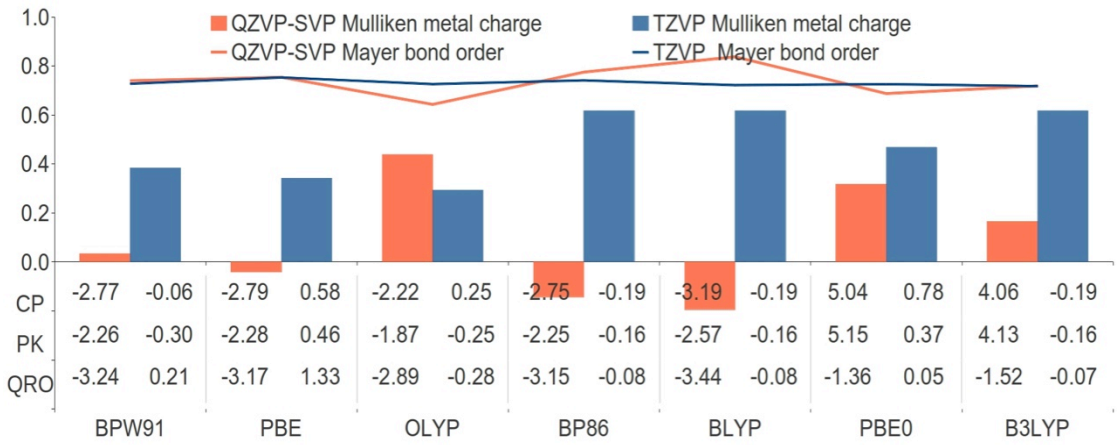

Figure 13: The calculated axial splitting (D cm^{-1}) for seven functionals and three spin orbit response methods in the QZVP-SVP basis on the left hand side columns and the TZVP basis on the right hand side columns. The Mulliken metal charge is represented by bars and the average Mayer bond order of the metal-to-ligand interaction is represented by lines.

All the DFT functionals in Figure 13 at the TZVP basis level calculate the *D* splitting to be much smaller than the experimental value of -4.5 cm^{-1}, the best result from this basis is the PBE-QRO combination that finds 30% of the experimental value (1.33 cm^{-1}). The PBE and PBE0 functionals both give a positive axial splitting and a low rhombicity. This molecule has been extensively studied by Neese, and he reports that his numbers agree well with experimental data. However, using the TZVP basis it has not been possible to replicate his success. It is notable that the crystal structure that is reported here has minor differences of the order of 0.01 Å for the metal-to-ligand bond lengths compared to the structure he uses in his calculations. To check the validity of these results, a second crystal structure for this molecule was tested and we found that the numbers were of the same scale as above for the TZVP basis.

We discovered that by moving to the QZVP-SVP basis the magnitude of *D* is dramatically increased. The hybrid functionals with the CP and PK methods agree well with the experimental number, but have an incorrect sign of splitting. The inversion of sign cannot be attributed to the rhombicity in these calculations as the *E/D* values for the PK set are ~0.06, a good agreement with the expected axiality of the molecule. PBE0-CP and PBE0-PK are the only combinations that result in axial splitting greater than experiment for this molecule. The majority of the splitting for these two combinations occurs in the α to α and β to β spin channels which have the same pre-factor in CP and PK and hence are similar in Figure 13. The GGA functionals are consistently more accurate with the QRO ZFS method, with a difference of around 1.0 cm^{-1} from experiment. The most accurate functional is the BLYP functional with an error of 23.8% (1 cm^{-1}) and the least accurate is OLYP which was 1.6 cm^{-1} from experiment.

The spin-spin coupling contribution is negligible for the TZVP basis, whereas it contributes ~0.4 cm^{-1} with the QZVP-SVP basis.

Population analysis in Figure 13 shows that at the QZVP-SVP level the hybrid functionals have more cationic Mulliken charges on the metal than the GGAs. An exception to this is found for OLYP, which is also the least accurate GGA functional for calculating *D* in this basis. The accuracy of OLYP for calculating *D* does improve with the QZVP-SVP basis despite the lower covalency, which may be indicative of the decontracted basis being better at forming the valence space. The most covalently bonded functional with the QZVP-SVP basis is BLYP with the QRO response method and this corresponds to the most accurate result for *D* with the correct sign.

4.3.2 Multi-configurational results.

Number of roots	Basis	Spin-spin *D* (cm^{-1})	Spin-orbit *D* (cm^{-1})	total *D* (cm^{-1})	total *E/D* (cm^{-1})
5 pentets 45 triplets	QZVP-SVP	1.446	3.06	4.07	0.135
5 pentets	QZVP-SVP	1.980	3.682	4.171	0.1342

Table 9: Summary of results from the state averaged CASSCF at the QZVP-SVP level including the population numbers.

Multi-configurational calculations at the TZVP basis level for $Mn(acac)_3$ all resulted in splitting below one wave number. When the triplet states were included in the orbital configurations available to the MRCI the spin-orbit coupling made the triplet contributions lower in energy than the pentet states by 3000 wavenumbers. Shown in Table 9 are the results of QZVP-SVP basis, both of which have the correct state ordering and splitting values nearly exactly that of experiment. The inclusion of triplet states in the CASSCF reduces the sublevel splitting.

4.3.3 Restricted open shell determinants with QDPT.

$Mn(acac)_3$ was confirmed to be a single-configuration wavefunction by running state optimised CASSCF calculations over 5 d orbitals at the TZVP basis level. No electron density is found in the virtual orbitals of the active space and indicates a pure ROHF solution. The resultant *D* splitting from this calculation is -0.015 cm^{-1} and is highly rhombic with an *E/D* value of 0.29.

Basis	Method	Spin-spin *D* (cm^{-1})	Spin-orbit *D* (cm^{-1})	Total *D* (cm^{-1})	total *E/D*
TZVP	HF	~	~	~	~
QZVP-SVP	HF	-0.52	-2.52	-3.04	0.03
TZVP	PBE0	-0.26	-0.27	-0.40	0.20
QZVP-SVP	PBE0	-0.46	-2.70	-3.15	0.00
TZVP	PBE	-0.06	0.39	0.36	0.09
QZVP-SVP	PBE	-0.40	-2.47	-2.87	0.06

Table 10: The QDPT ZFS values from restricted open electronic structure methods.

The *D* splitting values from QDPT in Table 10 are similar to the perturbed DFT calculations shown earlier for both basis sets. The TZVP basis resulted in much smaller *D* values than the QZVP-SVP basis. A possible contributive factor is that to obtain d centric valence orbitals for the CASSCF active space the TZVP calculations had to be started from the QRO orbitals of a converged unrestricted calculation. The ROHF calculation at the TZVP level did not converge to d centric valence orbitals and thus was excluded from these results. The QZVP-SVP basis reasonably reproduces the experimental *D* and *E/D* values, with PBE0 having the highest accuracy with a splitting of -3.15 cm^{-1}. Despite a lack of dynamical correlation the ROHF calculation reasonably replicates the *D* splitting at 2 cm^{-1} (32%) less than the experimental value.

For both crystal structures of $Mn(acac)_3$ that we tested in this work the QZVP-SVP

basis results in higher molecular energy than for the TZVP basis. Other systems in this work find the converse to be the case and this may indicate insufficient flexibility of the basis to account for geometric distortions in this molecule. We find similar results for calculations without ZORA.

4.4 Iron-tris-acetylacetonate - $Fe(acac)_3$.

Experimental splitting values for this compound are D = -0.14 cm^{-1}, E = 0.03 cm^{-1} and thus E/D = 0.214 making the molecule rhombically distorted.

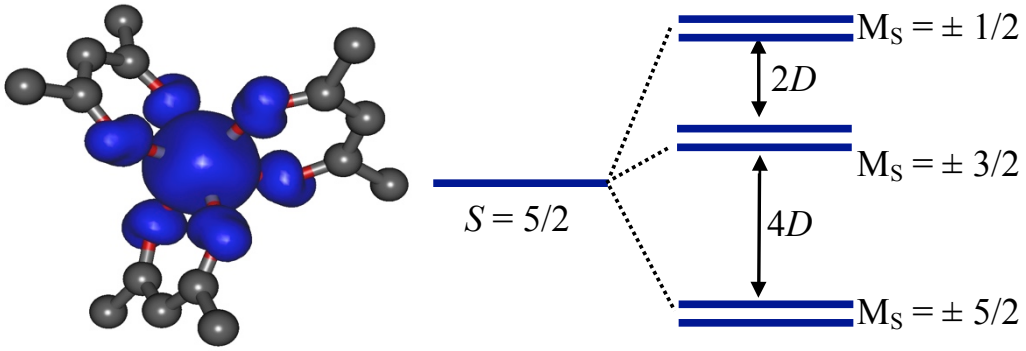

Figure 14: Left: Spin density for $Fe(acac)_3$ studied at the B3LYP-TZVP level. Isosurface rendered at 0.004 a.u. Right: The splitting diagram from the ZFS Hamiltonian for the sextet state.

4.3.1 DFT results.

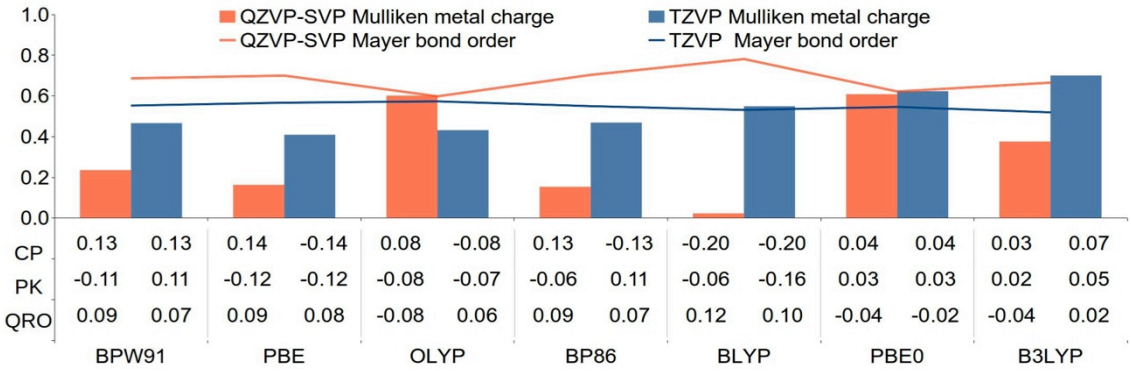

Figure 15: The calculated axial splitting (D cm^{-1}) for seven functionals and three spin orbit response methods in the QZVP-SVP basis on the left hand side columns and the TZVP basis on the right hand side columns. The Mulliken metal charge is represented by bars and the average Mayer bond order of the metal-to-ligand interaction is represented by lines.

When discussing the ZFS of the molecule it is necessary to emphasise the small size of the splitting and the high rhombicity that makes the sign of D harder to determine. Figure 15 shows that there is little to distinguish the results of the GGA functionals, the worst of which is the OLYP functional that finds D to be below 0.08 cm^{-1}. The hybrid

functionals did not calculate the splitting with as much accuracy as the GGAs and generally only managed 50% of the experimental splitting. The QZVP-SVP basis is again found to create more covalent interactions around the metal. The GGA-QRO combination showed larger *D* splitting values by 0.1 – 0.2 cm^{-1}. The GGA-CP combinations results in the most accurate splitting values, with the PBE functional calculating *D* exactly.

The sign of *D* is found to vary with both basis sets, this is because of the high rhombicity of ~0.3 for many of the calculations. High rhombicities indicates a situation where the splitting is highly anisotropic between the three axis (i.e. the gap between the sub-levels of x, y and z axis is similar). For such calculations a correct or consistent sign cannot necessarily be obtained as the choice of the major axis is not definable in the rhombic limit.

The spin-spin coupling does not vary much between the two basis sets for $Fe(acac)_3$ and is inconsistent across functional type with values between 8% (0.01 cm^{-1}) and 28% (0.03 cm^{-1}) of the total *D* value.

4.4.2 Restricted open shell determinants with QDPT.

Basis	Method	Spin-spin *D* (cm^{-1})	Spin-orbit *D* (cm^{-1})	Total *D* (cm^{-1})	total *E/D*
TZVP	HF	-0.01	-0.01	0.01	0.03
QZVP-SVP	HF	-0.01	0.01	0.01	0.06
TZVP	PBE0	-0.03	-0.02	-0.05	0.11
QZVP-SVP	PBE0	-0.03	-0.02	-0.05	0.11
TZVP	PBE	-0.04	0.02	-0.03	0.10
QZVP-SVP	PBE	-0.04	0.01	-0.03	0.04

Table 11: The QDPT ZFS values from restricted open electronic structure methods.

A CASSCF(5,5) for a sextet state has only one possible configuration and thus our discussion is limited to restricted open determinants with QDPT. The most accurate *D* values in Table 11 were from the PBE0-QZVP-SVP combination at 32% of experiment, additionally this method had the highest rhombicity at 0.109. The spin-spin term was found to increase as the amount of HF exchange was reduced and all calculations found this term to be highly axial. The spin-orbit term for the ROHF and PBE calculations is highly rhombic at over 0.27 and thus results in a positive sign. For PBE the spin-spin term dominates the splitting and thus the total sign agrees with experiment. PBE0 has a spin-orbit rhombicity of 0.23, and a negative *D* splitting that coincides with the spin-spin component, resulting in the most accurate result.

4.5 Iron-tris-malonate - $[Fe(mal)_3]^{3-}$.

$[Fe(mal)_3]^{3-}$ has experimental values similar to $Fe(acac)_3$ with $D = \pm 0.12$ cm^{-1}, $E = 0.03$ cm^{-1} and $E/D = 0.25$ making the system highly rhombic. The sign for this molecule is not experimentally assigned and thus little comment can be made as to the performance of the functionals in this respect.

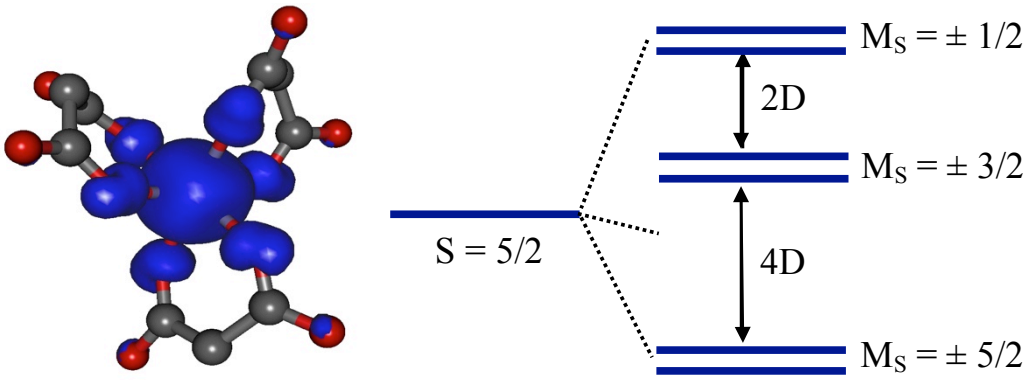

Figure 16: Left: Spin density for $[Fe(mal)_3]^{3-}$ studied at the B3LYP-TZVP level. Isosurface rendered at 0.004 a.u. Right: The splitting diagram from the ZFS Hamiltonian for the sextet state shown for $D < 0$.

4.5.1 DFT results.

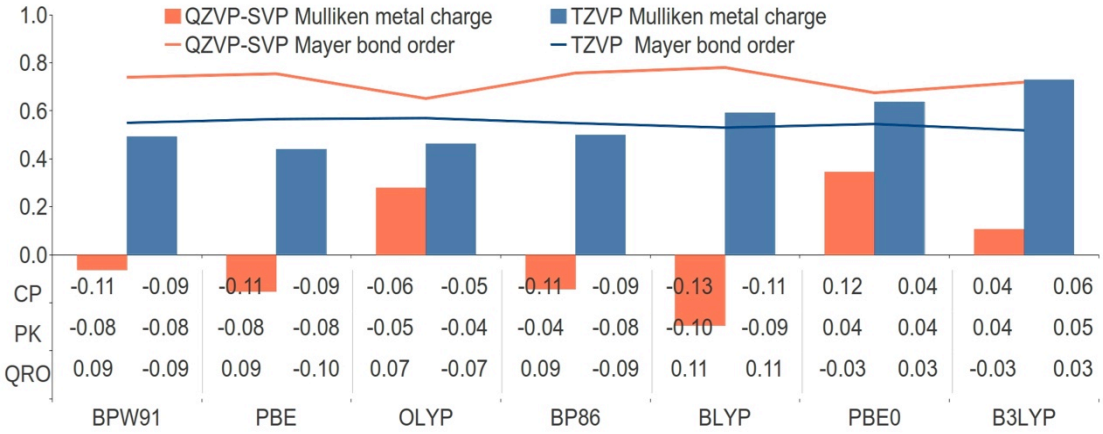

Figure 17: The calculated axial splitting (D cm^{-1}) for seven functionals and three spin orbit response methods in the QZVP-SVP basis on the left hand side columns and the TZVP basis on the right hand side columns. The Mulliken metal charge is represented by bars and the average Mayer bond order of the metal-to-ligand interaction is represented by lines.

The $[Fe(mal)_3]^{3-}$ system, shown in Figure 17, is more covalent with the QZVP-SVP

basis. The GGA functionals form negative Mulliken charges for this basis, except for the OLYP functional. For both basis sets OLYP is the least accurate GGA for calculating the *D* splitting. The BLYP functional is both the most covalent and the most accurate functional for calculating *D*. Hybrid functionals are generally less accurate than the GGAs, although the PBE0-CP combination manages to calculate the splitting exactly, however with the TZVP basis this combination only recovers 30% of the experimental splitting.

The CP ZFS method results in splitting numbers ~0.1 cm^{-1} larger than the QRO method which is larger by this amount again than the PK method. The hybrid functionals find a positive *D* with CP and PK. This contrasts with the negative sign for these ZFS methods with the GGA functionals. The QRO ZFS method is not found to be consistent in calculating a sign of *D*.

The *E/D* values were found to vary for all combinations of functionals and basis sets, for example BP86-PK has a rhombicity of 0.05 for QZVP-SVP and then 0.28 for the TZVP basis, we attribute this to the fact that the *E* value is 0.03 for this system may be reaching the limits of the numerical precision for the SOMF(1X) operators evaluation of spin-orbit effects.

4.5.2 Restricted open shell determinants with QDPT.

Basis	Method	Spin-spin D (cm^{-1})	Spin-orbit D (cm^{-1})	Total D (cm^{-1})	total E/D
TZVP	HF	-0.01	0.02	0.02	0.12
QZVP-SVP	HF	-0.01	0.02	0.02	0.09
TZVP	PBE0	-0.02	-0.02	-0.04	0.03
QZVP-SVP	PBE0	-0.02	-0.02	-0.04	0.03
TZVP	PBE	-0.02	-0.02	-0.05	0.16
QZVP-SVP	PBE	-0.02	-0.02	-0.05	0.15

Table 12: The QDPT ZFS values from restricted open electronic structure methods.

The sign of the spin-spin and spin-orbit terms are coincident for the DFT calculations in Table 12 and combine to result in a negative *D*. All the calculations find smaller *D* splitting values than experiment, the most accurate numbers were obtained with PBE where both the *D* and *E/D* values were around half of the experimental values. The ROHF determinant finds only 13% of the experimental splitting, as the wavefunction is uncorrelated this is unsurprising.

4.6 Conclusions for monometallic systems.

The use of density functional theory to calculate the ZFS is shown to be reasonably accurate for a range of molecules with different magnitudes of axial splitting. The use of the large de-contracted QZVP basis on the metal with a small SVP basis on the ligands provides more accurate splitting values and also reduces the computational cost, possibly opening a route to calculations of larger magnetic molecules. The sign of the splitting is generally found to be accurate for the GGA functionals, although ambiguity clearly arises in the case of $Fe(acac)_3$ and $[Fe(mal)_3]^{3-}$ where the magnitude of splitting is small and the rhombicity high. It may be necessary to replace the SOMF(1X) operator

in molecules with such small splitting values with the full SOMF operator, or another more accurate spin-orbit operator.

The hybrid functionals predict more ionic electronic structures compared to the GGAs, which we characterise by the Mayer bond order and Mulliken charge. By moving to the QZVP-SVP basis we find that the covalency is generally enhanced for the GGA functionals and combined with the QRO method is a way of increasing the magnitude of the splitting. Although we do not attribute this success purely as a parameter of the electronic populations, we do feel that this may be a good guide for picking better functionals for calculating the ZFS phenomenon. The OLYP functional is a clear outlier for the GGAs, throughout this work and other than for $[Fe(mal)_3]^{3-}$ it is more ionic with the QZVP-SVP basis. However, its ZFS values do show a small improvement in spite of its ionicity. The best DFT-ZFS combination for these molecules is BLYP-QRO with the QZVP-SVP basis (although PBE is a close second), which averaged over all results was 20% away from the experimental values. For many cases this combination provides the largest splitting magnitudes and the most consistent accuracy. The hybrid functionals are generally less accurate and have a wider variation in their ZFS values, this lack of consistency makes them hard to recommend with the current ZFS methods. The covalency is useful in characterising the shortcomings of these functionals for calculating ZFS, however other factors may need to be explored. For instance the HOMO-LUMO gap for the hybrid functionals is larger than the GGAs because the HF exchange reduces the self-interaction. Greater energy gaps between spin states could reduce their coupling and whether this is the root of the issue with hybrid functionals is open to further investigation.

Care should be taken when assigning the component energy levels of ZFS, as in the case of $V(acac)_3$ the axis of quantisation can sometimes be incorrectly chosen which can result in ostensibly bad M_s values, however clarification of the identity of the sub-levels

can be restored with the application of the Zeeman operator.

The single-configurational character for all these systems led us to try restricted open calculations coupled with QDPT. The results are somewhat encouraging and the ROHF method performs surprisingly well for the Cr and Mn systems. Restricted open DFT appears to be the better choice for QDPT, probably because of its improved description of the electronic density, although we do not feel it possible to recommend one functional over the other. The choice of functional warrants expanded study. Whilst the QDPT with single determinants did not provide the best results of our research it may be a more systematic route to improving *D*, by enabling the active space to be selectively and systematically expanded, providing more correlated spin orbit interactions. A particularly interesting route would be to employ one of the many multi-configuration DFT methods described in the literature.

4.7 Appendix.

In this appendix we examine an interesting diversion into the characterisation of the M_s states through the application of the Zeeman operator for the $V(acac)_3$.

		Energy (cm^{-1})	Contribution weight	M_s
STATE	A	**0**	0.19	1
			0.60	0
			0.19	-1
STATE	B	**4.24**	0.33	1
			0.33	0
			0.01	0
			0.33	-1
STATE	C	**22.88**	0.47	1
			0.06	0
			0.47	-1

Table 13: The SS+SOC spectra of the ZFS effect on the SA-CASSCF(2,5) over all triplet and singlet routes.

The micro-state splitting from the CASSCF(2,5) averaged over the triplet and singlet states is shown in Table 13. The ZFS is a measure of degeneracy breaking between the spin-projections (M_s value) at zero field, in most calculations the M_s number of each state can be identified by looking at the contributive weights. However, the weights in Table 13 cannot correspond to the energy level splitting that one would expect from the ZFS Hamiltonian. We find $M_s = 0$ to dominate state A and $M_s = \pm 1$ to dominate states B and C, this determination gives a D splitting ($Ms = 0 \rightarrow \pm 1$) of 4.24 cm^{-1} and an E

splitting (Ms = +/- 1 → -/+ 1) of 18.64 cm^{-1}. The E/D would thus be greater than 0.33 and is clearly incorrect. According to the ZFS Hamiltonian the largest splitting (D) is a measure of the splitting along the primary axis of quantisation (S_z) and combined with the rules of extracting splitting from the full ZFS tensor this restricts rhombicity to less than 1/3.

The primary quantisation axis in experiment is assigned according to the external laboratory frame (the direction of the magnetic field) and D is determined by observing the transitions in the Zeeman splitting of the Ms states in the Sz orientation. In Born-Oppenheimer calculations the assignment of Sz is arbitrary because all spin directions are isotropic and all spin projections (Ms) are degenerate. When the ZFS perturbation is applied to these calculations it is done in the molecular frame (without a magnetic field) and will not necessarily assign the primary axis of quantisation correctly. Because the spin coupling is anisotropic the degree to which it varies along the different axis determines which direction should be Sz. Thus it is not possible to definitively know the Sz direction before the calculation of D. And furthermore, the Ms values will not necessarily be those from the Sz direction, such as is the case in Table 13. To find the orientation that has good Ms values (the axis that corresponds to Sz) a rotation of the molecular frame is needed. The energy of the states in Table 13 would not change upon such a rotation as they are at zero field, all that is achieved is ensuring that the Ms weights reported in the energy spectra are those that correspond to the Sz direction as must be the case when properly defining D.

It is possible to find the correct orientation by applying a magnetic field and then rationalising the Zeeman splitting of the sublevels:

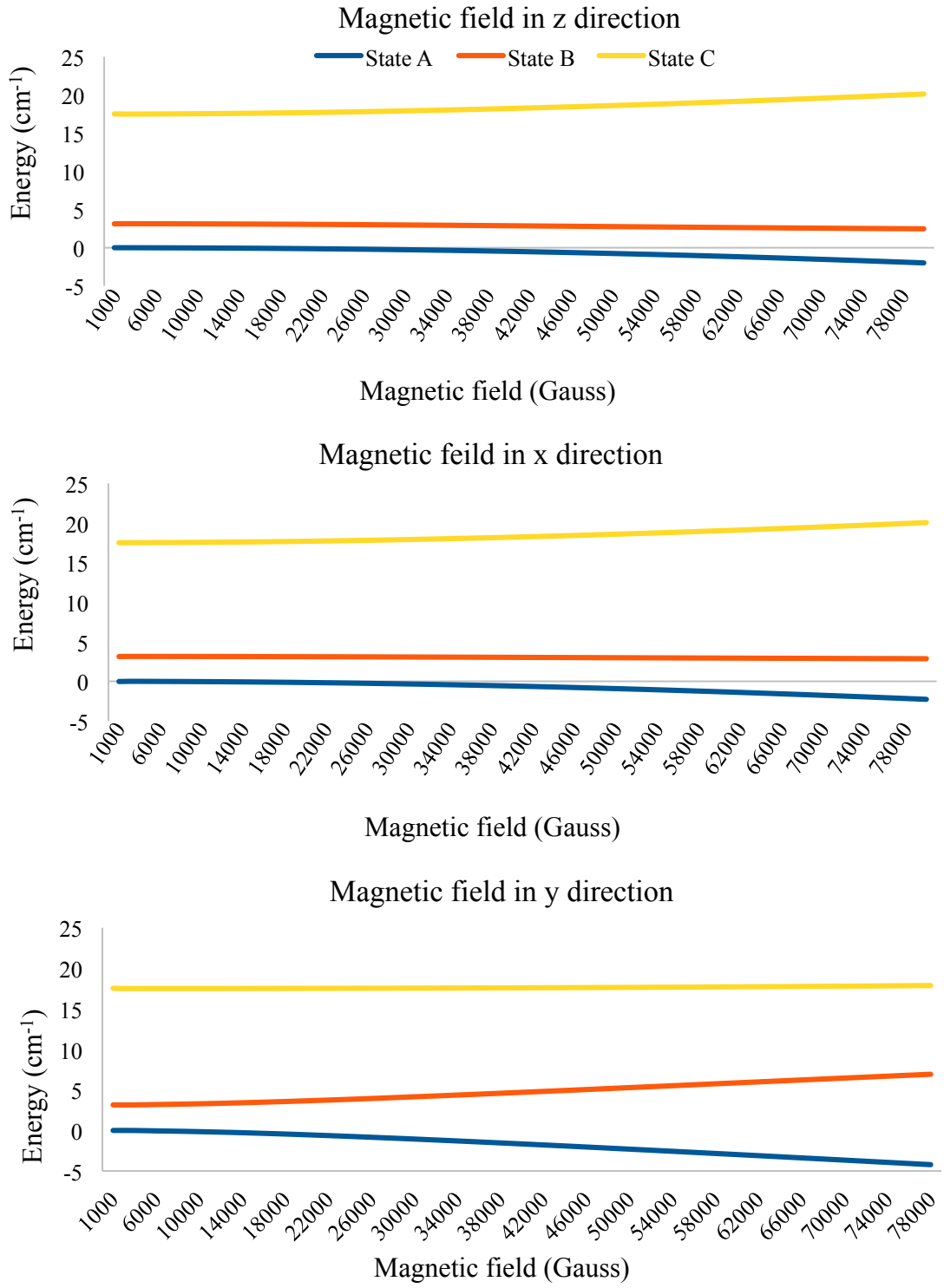

Figure 18: The effect of a magnetic field on the splitting of the first three energy levels from Table 13. The magnetic field is iterated in 1000 Gauss units on the three principal axes. Top left: x axis. Top right: z axis. Bottom: y axes. These number have been normalised to the ZFS by removing the stabilisation constant.

In Figure 18 we have attempted to replicate a high frequency EPR (HFEPR) experiment by applying a magnetic field along the x, y and z axis in 1000 gauss increments up to 80000 Gauss. Without ZFS perturbation these states would all be at 0

cm^{-1} and would split according to the g matrix. It is quickly apparent that the y direction has the behaviour that is expected of a triplet as is represented in Figure 8. States A and B split in the form of $M_S = \pm 1$ and state C is not affected by the magnetic field as would be expected for a $M_S = 0$ state. The splitting along the z direction shows all the states to be affected by the magnetic field and thus proves that this axis has no valid $M_S = 0$ sub-level. This is clear evidence that the y direction is the direction that we should be concerned with when applying the ZFS Hamiltonian and would be the axis chosen in experiment.

The spin-spin and spin-orbit contributions do not have coincident large axes of splitting for this calculation. The diagonalised **D** tensor from the spin-spin component has the directional splitting as y>x>z, whilst the SOC has the directions z>x>y. When these two components do not align it is conceivable that there would be some difficulty in choosing the direction from which to find M_S for the total splitting.

An alternative method to extract the anisotropy is to consider only the energy levels and assign the splitting according to the degeneracy rules that arise from the ZFS Hamiltonian. In the case of a triplet (shown in Figure 8) we should find a large splitting between the $0 \rightarrow \pm 1$ states and small splitting within the ± 1 states, which applied against Table 13 would give D as -20.88 cm^{-1} and E as 2.12 cm^{-1}, resulting in an E/D value of 0.11. These splitting values are more than twice the experimental values and possess a smaller rhombicity.

Chapter 5: Kremer's dimer.

5.1 Experimental data.

Most SMMs are based on large clusters of metal centres held together in an organic framework, this approach is taken in order to make the barrier of spin reversal larger by increasing the total spin of the system. Depending on the chemical environment metals in these frameworks can interact in different ways to produce either a ferromagnetic coupling or an antiferromagnetic coupling between the metals.

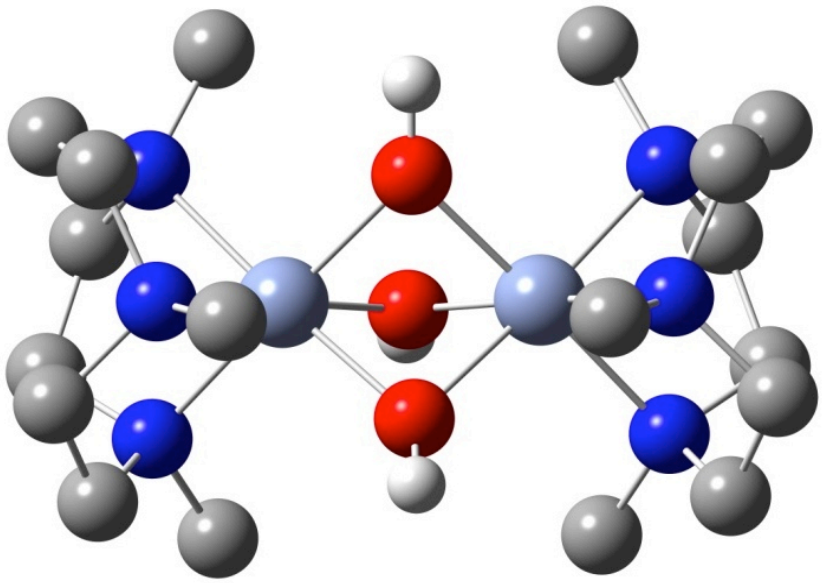

Figure 19: Structure of Tris(μ-hydroxo)bis[(1,4,7-trimethyl-1,4,7-triazacyclononane)chromium(III)]$^{3+}$. Hydrogens on terminal ligands omitted for clarity. C grey, Cr light blue, H white, O red, N dark blue.

Kremer's dimer[119,120] (Figure 19) is a well characterised candidate for studying the ZFS of two coupled metal centres. The molecule consists of two chromium(III) ions bridged by three super-exchange pathway μ-OH ions and each metal is capped by a neutral tridentate triazacyclononane ligand. The crystal structure that we use here was a tris-cation, tris-iodide salt, although we exclude the anions from this work. The removal of the anion is computationally expedient and avoids the long range closed shell

contributions identified by van Wullen[103]. Together the two chromium atoms possess six magnetically active electrons, which couple to produce four magnetically distinct spin states. The ground state for this system is the magnetically inactive antiferromagnetic S = 0 state, and then in accordance with the Heisenberg exchange interaction Hamiltonian is the S = 1 state, then the S = 2 state and the highest energy S = 3 state. The energy separation between these states and their respective ZFS values has been well characterised by experiment (Figure 20).

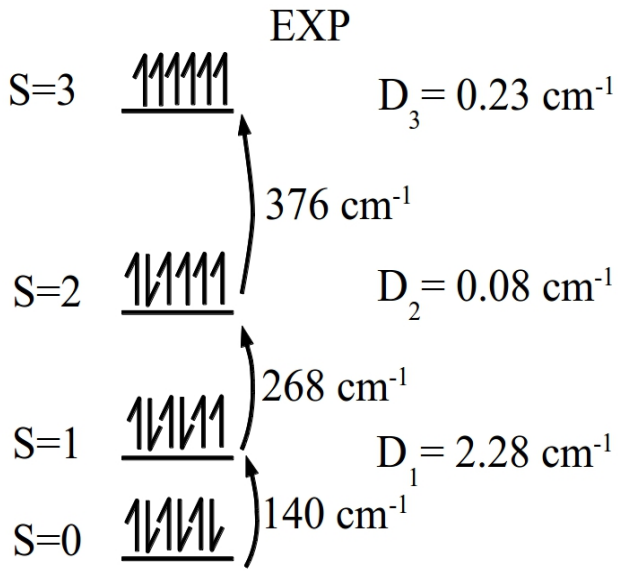

Figure 20: Experimentally determined energy levels and their axial ZFS values. Relative energies and D in cm^{-1}.

5.2 DFT calculations of the spin ladder.

Obtaining the correct order of spin states with DFT is our initial focus as a replication of the experimental ladder would be a good indicator of the validity of the converged solutions to which the ZFS perturbation is applied. Figure 3 shows the energy levels using various exchange-correlation functionals. The spin ladder was calculated for each functional starting with the converged S = 3 state from which the next lower spin state, was started and so on. For each broken symmetry state the correct

pairing of orbitals was checked through a visual inspection of the orbitals as well as analysis of the Mulliken spin densities. For the $S = 1$ state it was found that the solution with equivalent spins on both Cr atoms was of higher energy than the solution reported in Table 14. This can be rationalised by considering the nature of the exchange interactions in broken symmetry solutions. The aim of the broken symmetry approach is to produce a lower energy state through allowing the wavefunction to possess a lower spatial symmetry than the molecular geometry. Such states are achieved by starting low spin states from high spin solutions as we have done here. The reduction in energy occurs because of the localisation of like spins, which are correlated by the exchange term, is stronger at shorter distances. The solutions corresponding to Table 14 shows the alpha electrons to be localised on Cr_1 and the beta electrons on Cr_2 and thus there are greater exchange interactions for this solution than the symmetric ground state.

	B3LYP		PBE		TPSS		M06		M06-L	
	Cr_1	Cr_2	Cr_1	Cr_2	Cr_1	Cr_2	Cr_1	Cr_2	Cr_1	Cr_2
$S = 0$	2.97	-2.97	2.90	-2.90	2.88	-2.88	3.16	-3.16	2.87	-2.87
$S = 1$	2.99	-0.94	2.90	-0.84	2.86	-0.86	3.23	-1.04	2.92	-0.85
$S = 2$	3.04	1.07	2.89	1.25	2.84	1.14	3.29	1.14	2.93	1.24
$S = 3$	3.07	3.07	3.09	3.09	3.05	3.05	3.36	3.36	3.12	3.12

Table 14: The Mulliken spin densities for the chromium atoms for various DFT functionals.

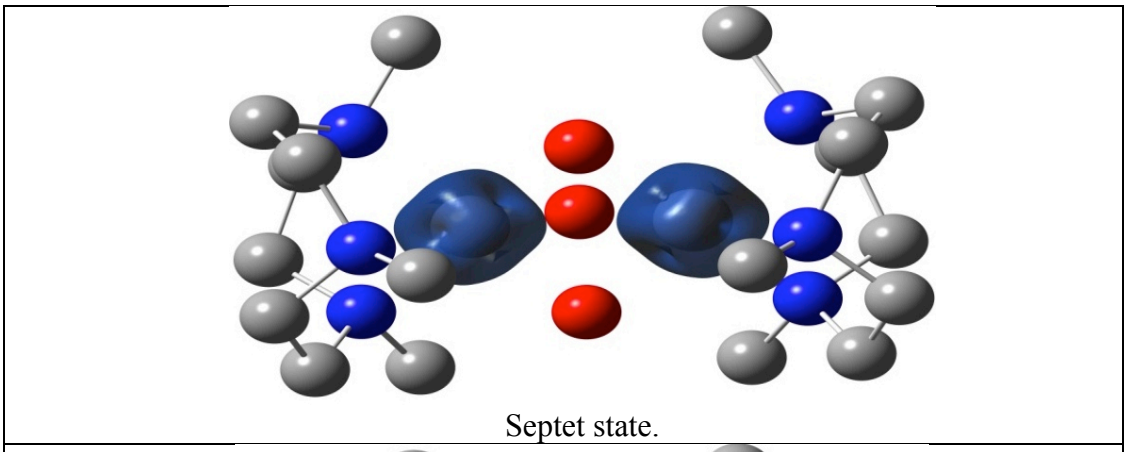

Septet state.

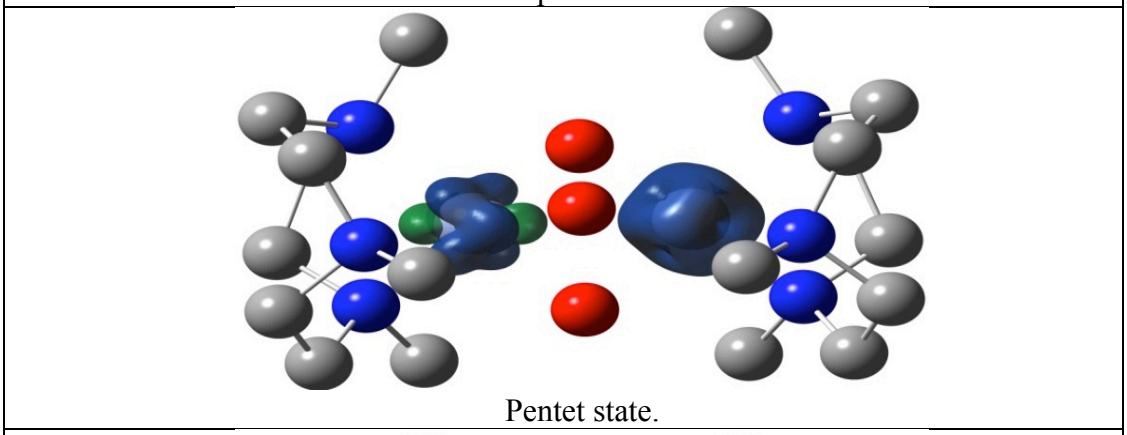

Pentet state.

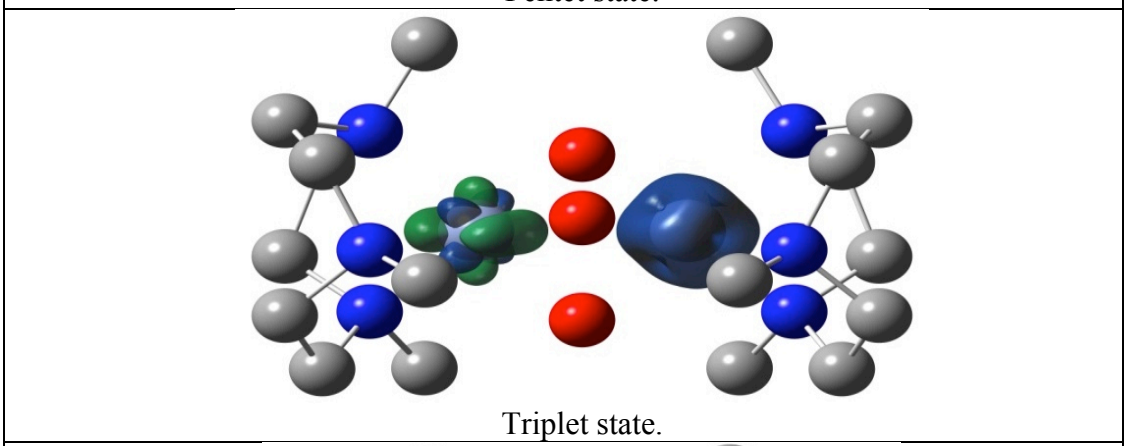

Triplet state.

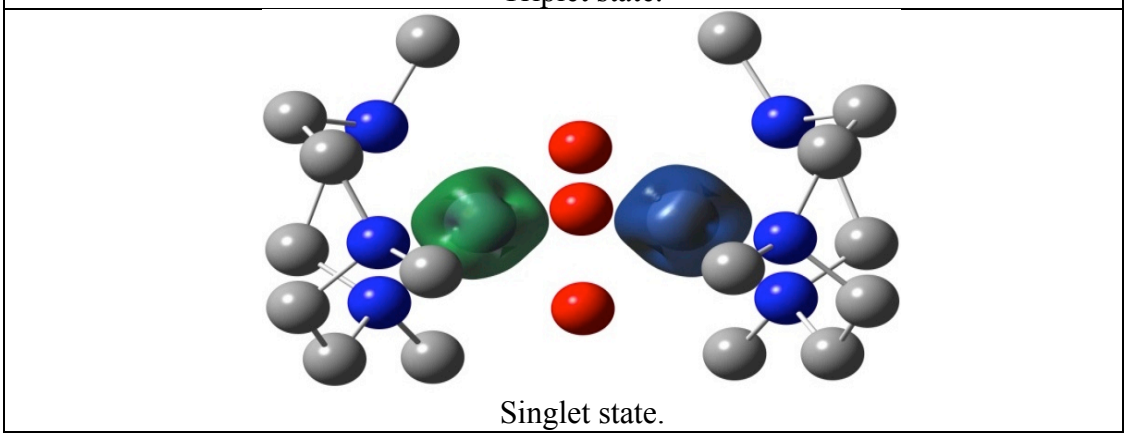

Singlet state.

Figure 21. The spin density calculated from the M06 functional for the 4 spin states with the iso surface rendered at 0.004 a.u.

Many calculations were performed in which occupied and virtual orbitals were swapped and re-optimised in an attempt to ensure that a global minimum was reached for each spin multiplicity. Shown in Figure 21 is the spin density of Kremer's dimer using the M06 functional for the 4 spin states. As the multiplicity decreases the amount of alpha spin density on the left chromium is found to decrease until the singlet state where there is only beta density present. This reflects Table 14 where for the pentet state the spin on Cr2 is reduced to 1.14 (one alpha electron) and the spin density plot shows the spin to be localised on the left Cr. The Mulliken spin on Cr2 is dominated by the two beta electrons and can be seen to be localised on the left Cr in the spin density plot.

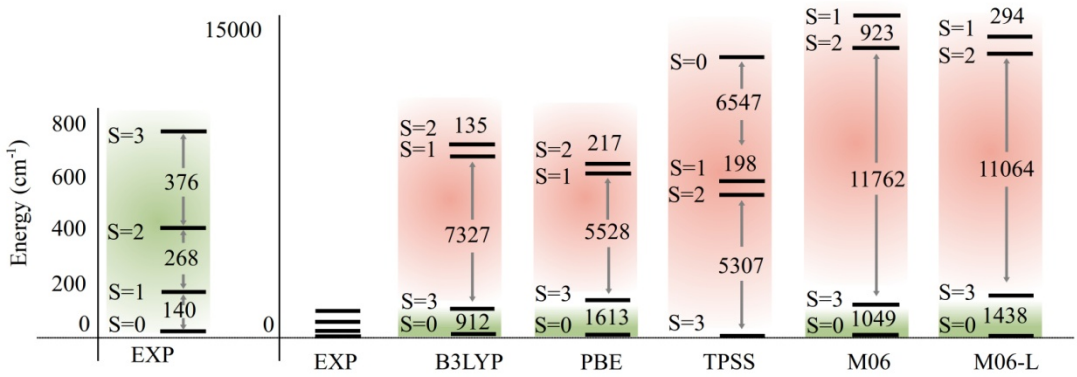

Figure 22: Ordering of energy levels of spin S = 0, 1, 2, 3. Experimental results are shown on an expanded scale and also on the same scale as the DFT calculations. Relative energies in cm–1. The basis set is QZVP-SVP.

The broken symmetry results in Figure 22 show the singlet-septet gap to be correctly ordered for B3LYP, PBE, M06 and M06-L, however the TPSS functional results in an inverted ladder. The experimental energy gap of 784 cm^{-1} between the $S = 0$ and $S = 3$ states is most closely replicated by the hybrid functionals, B3LYP and M06, with errors of 128 cm^{-1} and 265 cm^{-1} respectively. The PBE and M06-L functionals resulted in an energy gap that is too large by approximately a factor of two. For all of the functionals tested the $S = 1$ and $S = 2$ states were problematic and are many thousands of wavenumbers too high in energy. It is clear from these results that standard DFT is not

able to qualitatively reproduce the spin energy ladder of Kremer's dimer.

5.4 Spin contamination.

State	$S(S+1)$	B3LYP	PBE	TPSS	M06	M06-L
$S = 0$	0	2.99	2.89	2.79	3.06	2.97
$S = 1$	2	3.93	3.82	3.60	3.99	3.90
$S = 2$	6	6.96	6.72	6.63	6.96	6.79
$S = 3$	12	12.04	12.05	12.03	12.11	12.07

Table 15: The $\hat{S}^2$ eigenvalues for each spin state with the density functionals used.

The eigenvalues of $\hat{S}^2$ shown in Table 15 indicate that the $S = 0$, $S = 1$, and $S = 2$ states are of broken spin symmetry for all functionals used. The $S = 3$ state possesses least spin contamination for any functional as any higher multiplicity states lie much higher in the energy manifold. The presence of such high spin contaminations means that to achieve a lower energy solution DFT is incorporating character of higher spin states and can be indicative of the converged state not being adequately described by the unrestricted methodology. Although it must be stated that some caution is warranted as to the definition of $\hat{S}^2$ in the context of DFT.

5.5 ZFS from DFT.

State	*Expt.* *D*	B3LYP CP	B3LYP QRO	PBE CP	PBE QRO	TPSS CP	TPSS QRO
$S = 1$	2.2	-0.73	-	3.13	-	-3.63	-
$S = 2$	0.08	14.33	0.27	1.63	0.9	1.37	0.66
$S = 3$	0.24	0.068	0.05	0.12	0.14	0.10	0.12

Table 16: D values (cm^{-1}) obtained with DFT and the CP or QRO methods.

The *D* splittings corresponding to the states shown in Figure 22 are given in Table 16. The QRO results for the triplet states have been omitted since the degree of spin contamination precludes returning the unrestricted natural orbitals to spin eigenfunctions as is done to form the QROs.

For the $S = 1$ state, the B3LYP-CP method is the wrong sign for *D* and gives a splitting 1.5 cm^{-1} (67%) smaller than experiment. Conversely the PBE-CP and TPSS-CP methods produce values too large by ~1 cm^{-1}. For the $S = 2$ state the QRO method produces values of *D* three times that of the experimental value. The CP method results in *D* splitting more than two orders of magnitude greater than experiment, and is particularly inaccurate with the B3LYP with a splitting of 14.33 cm^{-1}. All of the tested combinations of density functionals and CP or QRO methods resulted in *D* values that are too large for the $S = 2$ state. The *D* values for the $S = 3$ state are universally too small, but do approach the experimental value within a factor of two. In this case, where the QRO method is most applicable because of the small degree of spin contamination, very little difference was observed between the CP and QRO results. Despite having the best gap between the $S = 0$ and $S = 3$ states for the energy ladder, the B3LYP is decidedly the least accurate ZFS values of the three functionals.

5.6 CASSCF orbitals.

5.7.1 CASSCF (6,6).

The larger degree of spin contamination for the broken spin symmetry solutions obtained for Kremer's dimer suggest the presence of multi-configurational character. Given the poor ordering of the spin state ordering, and the values of D, it may be assumed that the degree of multi-configurational character is sufficiently strong that the broken symmetry density functional approach does not adequately deal with it. To investigate this suggestion we performed complete active space self-consistent field (CASSCF) calculations. We began with the ground state (S = 0) by finding the 10 molecular orbitals comprised of the 3d orbitals of the Cr atoms. The six lowest energy of these orbitals were included in the active space along with the six electrons coming from the metal centers. Following orbital optimisation the six orbitals shown in Figure 23 were obtained.

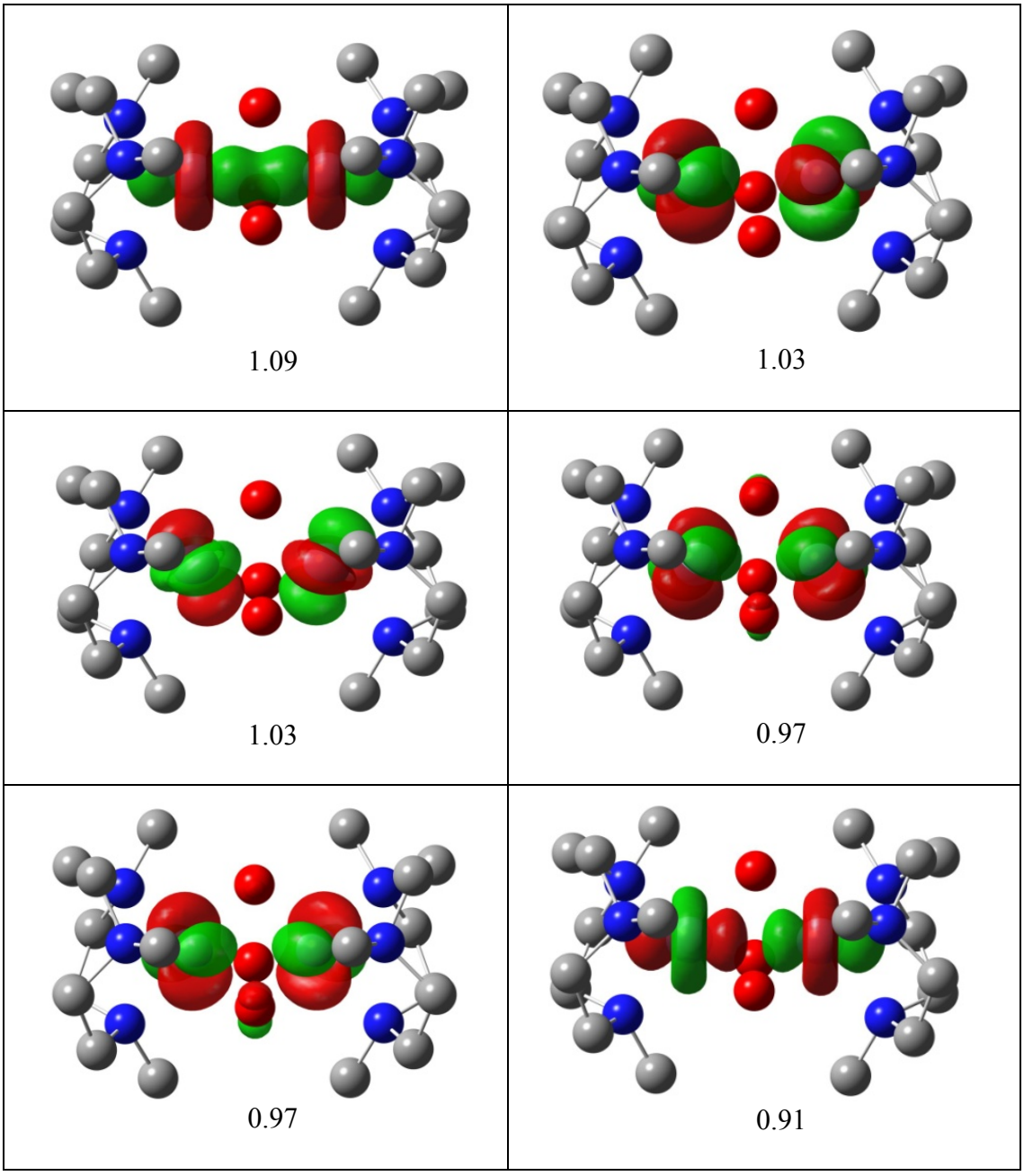

Figure 23: The active orbitals from the CASSCF(6,6)/SVP for the S = 0 state and their natural orbital occupation numbers.

5.7.2 CASSCF(6,10).

The MOs for the CASSCF are proven to be of good d configuration in Figure 23. The natural orbital occupation numbers are shown alongside each orbital and it can be seen that the $S = 0$ state is an open-shell spin-paired state with each orbital having an occupancy of about 1. This reflects the physical situation which the broken symmetry approach attempts to reproduce by allowing the spatial component of the α and β to have the freedom to localise away from each other. The dominant configuration state function (CSF) has a coefficient of only 0.28, with the next 20 most significant CSFs having coefficients of about 0.1. These data all indicate a strongly multi-configurational structure. A similar situation was found for the $S = 1$ and $S = 2$ states. Accordingly, we performed a number of state-optimised CASSCF and state-averaged (SA-CASSCF) calculations, including the remaining 3d orbitals *i.e.* CASSCF(6,10) calculations, to characterise the spin states. Figure 24 shows the converged orbitals of the SA-CASSCF(6,10). The SA-CASSCF(6,10) calculations correspond to an equal weight averaging over the lowest root (most dominant state) of each spin multiplicity. The strongly occupied orbitals are qualitatively indistinguishable from those of the state optimised CASSCF(6,6). The 4 virtual orbitals added to the active space show only a small amount electronic density occupation. It should be stressed that their inclusion is critical in the calculation of the ZFS as they are still coupled via the SOC operator. Figure 25 shows the ordering of energy levels obtained from CASSCF(6,10) and SA-CASSCF(6,10) calculations.

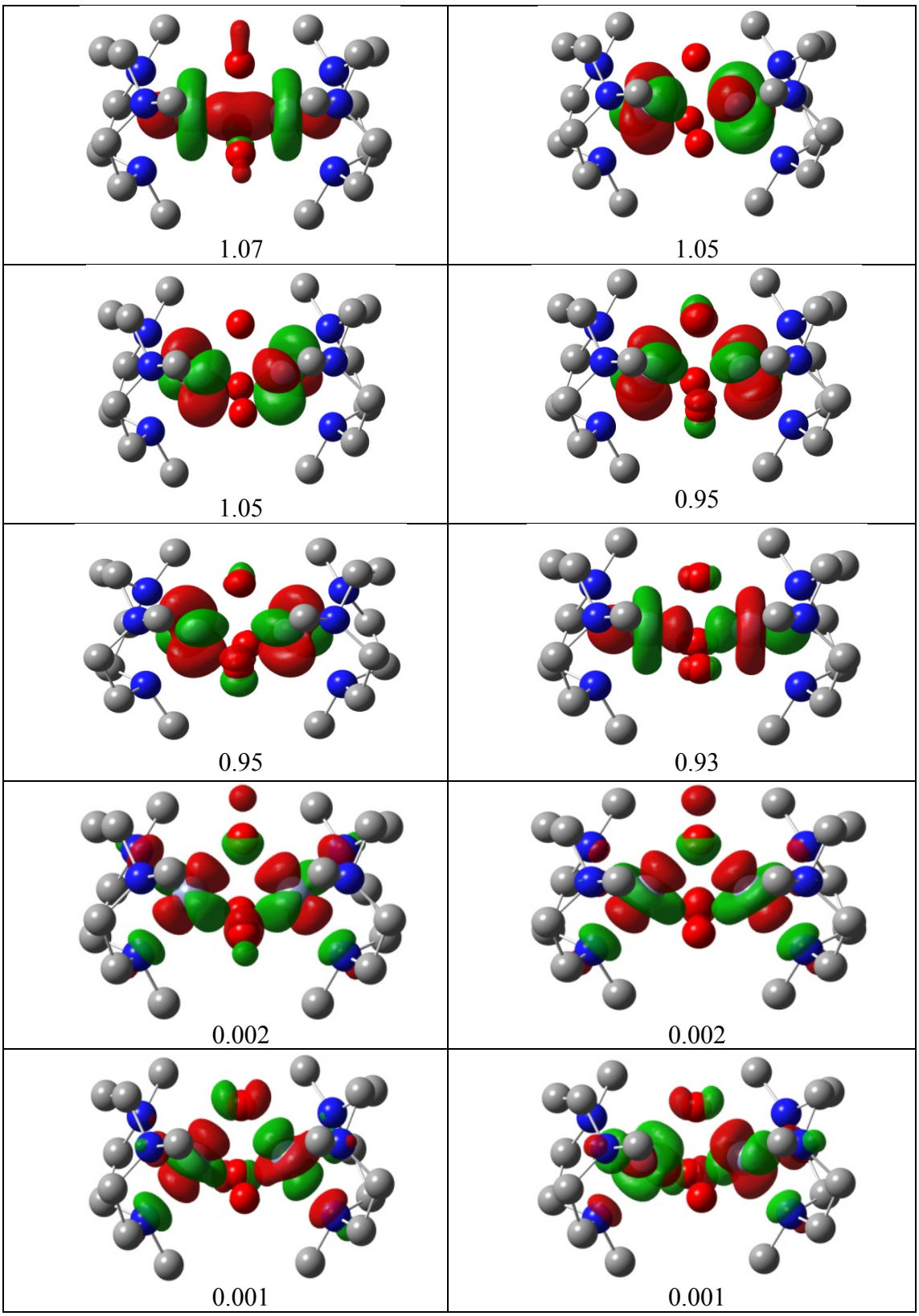

Figure 24: The active orbitals at the SA-CASSCF(6,10)/SVP level. The averaging is over the ground state for each spin multiplicity. Natural orbital occupation numbers are shown.

5.8 CASSCF spin ladder.

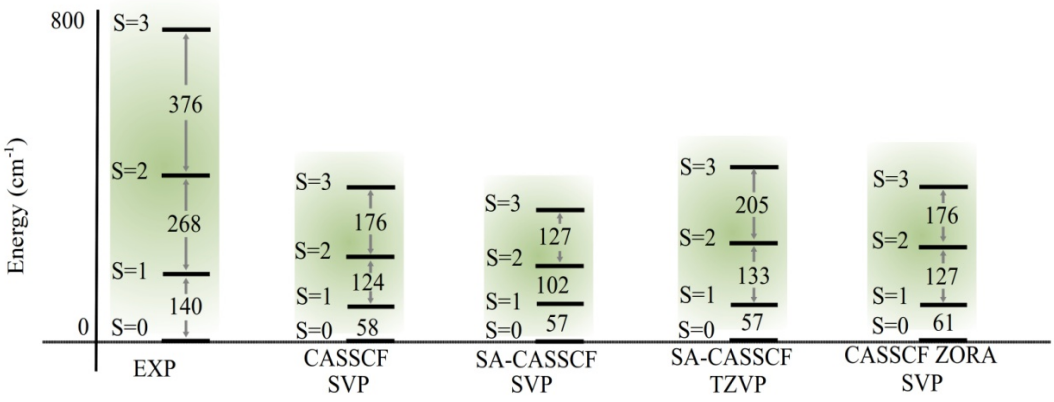

Figure 25: Relative ordering of energy levels from CASSCF(6,10) and SA-CASSCF(6,10) calculations, see text. Relative energies in cm^{-1}.

It is apparent from Figure 25 that both the state averaged and state optimised CASSCF calculations correctly reproduce the state ordering, although the energy gaps are a factor of two smaller than experiment. This is in stark contrast to the results from DFT shown in Figure 22. The SA-CASSCF calculations produce slightly smaller energy gaps. We also tried increasing the size of the basis on the Cr atoms to triple ζ and including ZORA corrections but these had relatively little effect on the energy level splittings.

5.9 SA-CASSCF root convergence.

Turning now to the calculation of *D*, we used a QDPT framework to calculate the ZFS, in which states corresponding to the roots of the CASSCF method are mixed under the spin-orbit operator. All the necessary states for the ZFS are accounted for by including spin states with $\Delta S = 0, \pm 1$ for each reference state, e.*g.* for the $S = 2$ reference state, $S = 1$, $S = 2$ and $S = 3$ states are included in the QDPT. A large span of state energies, amounting to an interval >6 eV, were allowed to mix in the spin orbit treatment, these correspond to spin-orbit coupling with spin anisotropic states of larger multiplicity (i.e. those which have their spin projection degeneracy broken by the spin-

orbit operator) which lie much higher in the virtual space. We varied the number of states of each spin multiplicity that were included in the state-averaged ZFS calculations. The variations in the calculated *D* values are shown in Table 17.

Spin state	*Expt. D*	10 states	20 states	30 states	40 states	50 states
$S = 1$	2.2	-0.653	-2.199	-1.913	-1.923	-1.767
$S = 2$	0.08	0.121	0.138	-0.097	-0.029	-0.048
$S = 3$	0.24	-0.006	0.413	0.166	0.092	0.142

Table 17: D values (cm^{-1}) from SA-CASSCF(6,10) calculations. The number of states specified refers to the number taken from each of the S = 0, 1, 2, 3 states.

We cannot expect monotonic convergence for this process with respect to the number of roots included from the state averaging, because the inclusion of increasing numbers of higher lying states will degrade the description of the lower lying electronic states. From the results in Table 17 we find a reasonable stability of the results with the inclusion of 40 – 50 states from each spin multiplicity. The best results compare well with the small splitting from experiment for the $S = 2$ state and the large splitting of the $S = 1$ state.

5.10 State averaged ZFS.

We also investigated the effect on the results from varying the different spin states included in the state-averaging process. Table 18 shows *D* to be relatively insensitive to the spin states that are included in the state-averaging. The results of the [0,1,2,3] set (third column) are the same as the 50 state selection in Table 17. The *D* splittings closest to experiment are obtained when using orbitals averaged without the $S = 0$ state. In particular the [1,2,3] configuration gives results reasonably comparable to experiment. The $S = 0$ state is irrelevant to the ZFS values as it is magnetically inactive and any

orbital character it contributes to the SCF does not enhance the relevant orbitals for the spin-orbit term or the spin density which defines the spin-spin contribution. Removal of the $S = 0$ states changes the sign of D in the $S = 2$ state, showing the importance of choosing an appropriate set of spin states in the state-averaging process.

Spin state	*Expt.* $\|D\|$	[0,1,2,3]	[0,1,2]	[1,2,3]	[2,3]
$S = 1$	2.2	-1.767	-1.767	-1.943	-
$S = 2$	0.08	-0.048	-0.035	0.016	-0.143
$S = 3$	0.24	0.142	-	0.155	0.173

Table 18: D values (cm^{-1}) obtained with the inclusion of different spin multiplicities in the state-averaging process. All calculations refer to SA-CASSCF(6,10). The spin states included are given in square brackets are.

5.11 State optimised ZFS.

The ZFS values were calculated with orbitals optimised for each reference (ground state) spin multiplicity, see Table 19. This means that each state was optimised without the SCF mixing in contributions from configurations of different multiplicities. When doing the ZFS calculations these orbitals are used for the $S = \pm 1$ states without any optimisation. The $S = 1$ optimised orbitals resulted in a D value that is too large (by 0.4 cm^{-1}), this was not observed in any of the other CASSCF calculations of this state. For the $S = 2$ state, D is 0.019 cm^{-1} larger than experiment when calculated with $S = 2$ optimised orbitals (column 4) and is amongst the best values for this state that we have obtained. For the $S = 3$ state, D differs from experiment by just 0.053 cm^{-1}. An interesting trend can be found when comparing this result to the state averaged values from Table 18. We find an improved agreement with experiment of the D splitting upon removal of the averaging of other states, *i.e.* removal of the $S = 0$ state increases the splitting by 0.012 cm^{-1}, the additional removal of the $S = 1$ state further improves the value by another 0.019 cm^{-1} and using state optimised ($S = 3$) orbitals yields a further

improvement of 0.014 cm^{-1}. This can be traced to the fact that the $S = 3$ is the highest lying state and has a large energy gap with the $S = 2$ state, it appears the character of the other states may be causing degradation of D for the $S = 3$ state.

State Optimised	*Expt.* $\|D\|$	D ($S = 1$)	D ($S = 2$)	D ($S = 3$)
$S = 1$	2.2	**-2.608**	-2.008	Not included
$S = 2$	0.08	0.044	**0.027**	-0.141
$S = 3$	0.24	Not included	0.175	**0.187**

Table 19: D values (cm^{-1}) obtained with state optimised orbitals. Bold values on the diagonal shown are the D values from orbitals optimised for that spin state.

5.12 Spin-spin and spin-orbit contributions of the ZFS.

An advantage that theoretical chemistry has to offer experiment is the ability to extract the components of the ZFS and provide analysis that can aid in the design of SMMs. Using the SA-CASSCF results that we have described, we illustrate that the SS contribution to D for this molecule is not insignificant, see Table 20. The $S = 1$ state shows a large contribution, -0.67 cm^{-1} which adds to the SOC component. The $S = 2$ and $S = 3$ state have negative SS components which act to reduce the overall anisotropy. In particular, the SS contribution for the $S = 2$ state is larger than the SOC contribution. In the earlier discussion we mentioned the $S = 2$ state optimised orbitals have a different sign for D to the state averaged set (Table 18), this can be traced to an increase in the SOC term, which goes from 0.063 cm^{-1} to 0.150 cm^{-1} upon using state optimised orbitals. The degree of this contribution is significant and shows that its inclusion is necessary in any future calculation of ZFS values.

Spin state	*Expt.*|*D*|	Spin-spin cm^{-1}	Spin-orbit cm^{-1}	Total cm^{-1}
$S = 1$	2.2	-0.673	-1.091	-1.767
$S = 2$	0.08	-0.107	0.063	-0.048
$S = 3$	0.24	-0.015	0.159	0.142

Table 20: The breakdown of the spin-spin and spin-orbit components for the SA-CASSCF [0,1,2,3].

5.13 The Rhombic term.

5.13.1 SO-CASSCF.

The rhombic splitting parameter (*E*), being half the splitting between the $M_s = \pm 1$ microstates, was also calculated. Kremer's[120] analysis assumes C_{3h} symmetry to derive the *D* values. C_{3h} implies axial symmetry and $E = 0$. Symmetry this high does not allow enough degrees of freedom for the X and Y components of *D* to vary and create rhombic anisotropy.

State Optimised	*E* (*S* = 1)	*E* (*S* = 2)	E (*S* = 3)
$S = 1$	**0.029**	0.027	-
$S = 2$	0.007	**0.008**	0.019
$S = 3$	-	0.019	**0.024**

Table 21: E values (cm^{-1}) obtained with state optimised orbitals. Bold values on the diagonal shown are the E values from orbitals optimised for that spin state.

5.13.2 SA-CASSCF.

Spin state	[0,1,2,3]	[0,1,2]	[1,2,3]	[2,3]
$S = 1$	0.003	0.003	0.006	-
$S = 2$	0.002	0.001	0.002	0.006
$S = 3$	0.003	-	0.004	0.020

Table 22: E values (cm^{-1}) obtained with the inclusion of different spin multiplicities in the state-averaging process. All calculations refer to SA-CASSCF(6,10). The spin states included are given in square brackets.

E was less than 0.03 cm^{-1} for all of the states and methods utilised. The state-optimised orbitals in Table 21 have much larger *E* splitting values than those from the state-averaged calculations in Table 22. This resembles the smaller *D* splitting found for orbital averaged CASSCF shown earlier. An observation of note is that the $S = 2$ *E* splitting in Table 21, when compared with its partner *D* points to substantial rhombicity ($E/D = 0.3$). The EPR experiments do not indicate any rhombicity. The calculated magnitude of *E* reported here is small enough to be around the margin of error for electronic calculations and thus may be too small to draw general conclusions from.

5.14 QZVP-SVP results.

Additional to the work published on Kremer's dimer we have performed state optimised calculations using the QZVP-SVP basis. The splitting between spin states was found to be $S = 0 \rightarrow S = 1 = 47$ cm^{-1}, $S = 1 \rightarrow S = 2 = 131$ cm^{-1}, $S = 2 \rightarrow S = 3$ 189 cm^{-1}. This improves upon the state optimised results of SVP in Figure 25 by around 10 cm^{-1}. The $S = 1$ state was found to have a *D* of -1.55 cm^{-1}, $S = 2$ was found to have a *D* splitting of 0.105 cm^{-1} and the $S = 3$ state was found to have a splitting of 0.108 cm^{-1}. The most significant change is the $S = 2$ state has double the splitting of the SVP results. The monometallic results in chapter 4 are often more accurate with the decontracted QZVP basis with GGAs, however the hybrid functionals do not share this basis set

dependence. CASSCF calculations using the QZVP–SVP basis have little dynamic correlation and show a slight degradation of accuracy with the increase in the metal basis. This may indicate that to improve the accuracy of these calculations the inclusion of dynamic correlation is necessary.

5.15 Conclusions.

The challenges to the calculation of electronic structure posed by Kremer's dimer make the molecule an excellent test case for some of the current standard DFT techniques. The simple CASSCF techniques we have employed here are able to correctly treat the various spin states, but fall short of quantitative accuracy, as would be expected in the absence of treatment of the dynamic electron correlation. Reasonable agreement with experiment for *D* values can be obtained with a state averaged set of orbitals, however the best results are obtained with state-optimised orbitals. The spin-spin coupling is necessary in gaining good *D* splitting values. *E* values were calculated to be close to zero, in line with the experimental analysis based on C_{3h} symmetry.

Chapter 6: Summary, Conclusions and future work.

The momometalic systems show that there is clearly need for more study on the effect of basis when calculating the ZFS. The QRO method was found to be the most accurate method for the monometallic systems, however the limitation of its applicability is highlighted by Kremer's dimer, which has large amounts of spin contamination. The QZVP-SVP basis is shown to be an accurate approximation compared to the balanced TZVP basis. Using a large basis on the metal highlights an interesting route to improving the values of the ZFS and simultaneously decreasing the cost of the calculations. The $Mn(acac)_3$ system was shown to be more subtle than the literature suggests, however by increasing the basis it is possible to accurately calculate the ZFS for both CASSCF and DFT calculations. The labelling of the sub-state splitting was explored for $V(acac)_3$ and by using the Zeeman operator it is possible to correctly tease out the identity of the sub states.

Kremer's dimer was found to be a difficult molecule for DFT to accurately calculate due to its multi-configurational character. This molecule presents an interesting case where DFT fails entirely and shows how simple CASSCF calculations are able to accurately reproduce the experimental data. The limits of DFT may become an issue when larger SMM candidates are being studied and careful analysis should be put into the determination of whether the ground state can be approximated by a single determinant. State optimised CASSCF calculations prove to be the most accurate at determining the splitting values and it is our recommendation that this method is chosen over state averaged calculations where possible.

The results from Kremer's dimer do not suggest a bright future for DFT at calculating the properties of large SMMs. If candidate molecules can be guaranteed to be suitably singly configurational, then from the results presented here we suggest that GGA functionals be used with a large basis set on the metal. However, it is likely that

such systems will be similar multi-metallic compounds and thus careful consideration is needed to ensure that the system does not require multi-configurational treatment. In this vein we have started work on a tetra iron system[121] and have been able to obtain DFT values for the ZFS in good agreement with experiment. Unfortunately, analysis of the solution shows that the broken symmetry result has a large amount of spin contamination. Performing a CASSCF calculation would require a multi-billion configuration active space. Such a calculation is currently not possible and may indicate that current techniques in quantum chemistry are unable to scale to the type of large SMMs being studied by the inorganic community. A critical test of this will be to see if a restricted active space self-consistent field (RASSCF) calculation is capable of capturing enough of the multi-configurational character to make such calculations feasible.

A possible route to reach quantitative *ab-initio* accuracy at calculating the ZFS for large molecules is to try calculations that marry DFT with *ab-initio* methods. Recently, the author of this report started work on quantum embedding development, where post Hartree-Fock calculations can be embedded exactly in DFT wavefunctions. Once embedding can be extended to open shell systems Kremer's dimer serves as the perfect test-bed for such a methods applicability to SMMs. Another possibility would be to test such embedding methods on dimers of Cr_7Ni wheels[122] where it may be possible to treat the linkers to the coupled cluster singles, doubles and pertubative triples (CCSD(t)) " gold standard" level. Using these more exotic techniques we believe that it may be possible to apply theory to state of the art large SMMs.

[1] S. J. Bennie, D. Collison, J. J. W. McDouall, *J. Chem. Theory Comput.,* 2012, **8**, 4915-4921.

[2] H. Schift A. Kirsensen*, Handbook of Nanotechnology*, B. Bhushan, Springer, 3rd ed. 2007, 264.

[3] H. J. Richter, *J. Magn. Magn. Mater.*, 2009, **321**, 467-476.

[4] S. N. Piramanayagam, *J. Appl. Phys.*, 2007, **102**, 011301 (22 pages)

[5] E. L. Wolf, M. Medikonda, *Understanding the Nanotechnology Revolution*, Wiley, New York, 2012, 181.

[6] E. L. Wolf, *Nanophysics and Nanotechnology*, Wiley, New York, 2nd ed, 2006, 11.

[7] J. R. Friedman, M. P. Sarachik, *Annu. Rev. Condens. Matter. Phys.*, 2010, **1**, 109–28.

[8] G. Christou, D. Gatteschi, D. N. Hendrickson, R. Sessoli., *MRS Bulletin*, 2000, **25**, 66-71.

[9] M. Soler, W. Wernsdorfer, K. Folting, M. Pink, G. Christou, *J. Am. Chem. Soc.*, 2004, **126**, 2156-2165.

[10] P. Lin, T. J. Burchell, L. Ungur, L. F. Chibotaru, W. Wernsdorfer, M. Murugesu*, Angew. Chem. Int. Ed.*, 2009, **48**, 9489-9492.

[11] D. N. Woodruff, R. E. P. Winpenny, R. A. Layfield, *Chem. Rev.*, 2013, 5110–5148.

[12] O. Waldmann, *Inorg. Chem.*, 2007 **46**, 10035-10037.

[13] F. Neese, D. A. Pantazisab, *Faraday Discuss.*, 2011, **148**, 229-238.

[14] F. Neese, *J. Chem. Phys.* 2001, **115**, 11080. (17 pages).

[15] J. Cirera, E. Ruiz, S. Alvarez, F. Neese, J. Kortus, *Chem. Eur. J.*, 2009, **15**, 4078-4087.

[16] J. B. Lounsbury, *J. Chem. Phys.*, 1965, **42**, 1549. (6 pages)

[17] J. F. Harrison, *J. Chem. Phys.*, 1971, **54**, 5413. (5 pages)

[18] W. Gerlach, O. Stern, *Z. Phys. A.*, 1922, **9**, 353-355.

[19] A. Szabo, N. S. Ostlund, *Modern Quantum Chemistry: Introduction to Advanced Electronic Structure Theory*, Dover Publications, New York, New ed., 1996, 98-99.

[20] P. J. Atkins, *Physical Chemistry*, Oxford University Press, Oxford, 8th ed., 2006, 272.

[21] A. Szabo, N. S. Ostlund, *Modern Quantum Chemistry: Introduction to Advanced Electronic Structure Theory*, Dover Publications, New York, New ed., 1996, 146.

[22] J. Grãfenstein, D. Cremer, *Mol. Phys*, 2001, **99**, 981-989.

[23] A. J. Cohen, D. J. Tozer, N. C. Handy, *J. Chem. Phys.*, 2007, **126**, 214104 (4 pages).

[24] A. Szabo, N. S. Ostlund, *Modern Quantum Chemistry: Introduction to Advanced*

Electronic Structure Theory, Dover Publications, New York, New ed., 1996, 58.

[25] C. J. Calzado, J. Cabrero, J. P. Malrieu, R. C. Citation, *J. Chem. Phys*., 2002, **116**, 3985.

[26] C. J. Calzado, J. Cabrero, J. P. Malrieu, R. C. Citation, *J. Chem. Phys*., 2002, **116**, 2728.

[27] E. Fermi, *Ren. Accad. Naz. Lincei*. 1927, **6**, 602-607.

[28] L. H. Thomas, *Proc. Cambridge Phil. Soc.*, 1927, **23**, 542-548.

[29] J. C. Slater, *Phys. Rev.*, 1951, **81**, 385-390.

[30] J. C. Slater, T. M. Wilson, J. H. Wood, *Phys. Rev.*, 1969, **179**, 28-29.

[31] W. Koch, M. C. Holthausen, *Density functional theory for chemists*. Wiley, New York, 2nd edition, 2001,19.

[32] W. Koch, M. C. Holthausen, *Density functional theory for chemists*. Wiley, New York, 2nd edition, 2001, 22.

[33] R. G. Parr, W. Yang, *Density functional theory of atoms and molecules*, Oxford University Press, Oxford, 1989, 28.

[34] D. E. Ellis, *Density Functional Theory of Molecules, Clusters, and Solids*, Springer, Germany, 1995, 11.

[35] R. McWeeny, B. T. Sutcliffe, *Methods of molecular quantum mechanics*, Reprinted with SI units and revisions. edn., Academic Press, London, 1976, page 86.

[36] J. Kohanoff, *Electronic Structure Calculations for Solids and Molecules*, Cambridge University Press, Cambridge, 2006, 69.

[37] R. F. Nalewajski, *Perspectives in Electronic Structure Theory*, Springer, New York, 2012, 317.

[38] T. Yanai, D. P. Tew, N. C. Handy, *Chem. Phys*. *Lett.*, 2004, **393**, 51-57.

[39] J. Gräfenstein, D. Cremer, *Chem. Phys. Lett.*, 2000, **316**, 569-577.

[40] W. Kohn, L. J. Sham, *Phys. Rev.*, 1965, **140**, 1133-1138.

[41] C. E. Dykstra, G. Frenking, K. S. Kim, G. E. Scuseria, *Theory and Applications of Computational Chemistry*, *The First Forty Years*, Elsevier, Amsterdam, 2005, 682.

[42] N. H. March, *Electron Correlation in Molecules and Condensed Phases*, Springer, New York, 1996, 30.

[43] D. M. Ceperley, B. J. Alder, *Phys. Rev. Lett*., 1980, **45**, 566-569.

[44] J. P. Perdew, *Phys. B (Amsterdam, Neth.)*, 1991, **172**, 1-6.

[45] C. J. Cramer, *Essentials of computational chemistry*, Wiley, New York, 2nd ed., 2004, 280.

[46] A. D. Becke, *Journal of Chemical Physics*, 1993, **98**, 1372-1377.

[47] A. D. Becke, *Physical Review A*, 1988, **38**, 3098-3100.

[48] C. T. Lee, W. T. Yang and R. G. Parr, *Physical Review B*, 1988, **37**, 785-789.

[49] E. Engel, R. M. Dreizler, *Density functional theory : an advanced course*, Springer, Heidelberg, 2011, 204-205.

[50] J. P. Perdew, *Physical Review B*, 1986, **33**, 8822-8824.

[51] J. P. Perdew, J. A. Chevary, S. H. Vosko, K. A. Jackson, M. R. Pederson, D. J. Singh and C. Fiolhais, *Physical Review B*, 1992, **46**, 6671-6687.

[52] J. P. Perdew, K. Burke and Y. Wang, *Physical Review B*, 1996, **54**, 16533-16539.

[53] J. F. Dobson, G. Vignale and M. P. Das, *Electronic density functional theory : recent progress and new directions*, Plenum Press, New York ; London, 1998..

[54] J. P. Perdew, K. Burke and M. Ernzerhof, *Physical Review Letters*, 1996, **77**, 3865-3868.

[55] N. C. Handy and A. J. Cohen, *Molecular Physics*, 2001, **99**, 403-412.

[56] W. M. Hoe, A. J. Cohen and N. C. Handy, *Chemical Physics Letters*, 2001, **341**, 319-328.

[57] A. D. Becke, *Journal of Chemical Physics*, 1993, **98**, 5648-5652.

[58] C. Adamo and V. Barone, *Journal of Chemical Physics*, 1999, **110**, 6158-6170.

[59] J. M. Tao, J. P. Perdew, V. N. Staroverov and G. E. Scuseria, *Physical Review Letters*, 2003, **91**, 4. 146401-146404.

[60] Y. Zhao, D. G. Truhlar, *Journal of Chemical Physics*, 2006, **125**, 18.

[61] Y. Zhao, D. G. Truhlar, *Theoretical Chemistry Accounts*, 2008, **120**, 215-241.

[62] S. E. Wheeler, K. N. Houk, *Journal of Chemical Theory and Computation*, 2010, **6**, 395-404.

[63] K. R. Glaesemann, M. S. Gordon, *Journal of Chemical Physics*, 1998, **108**, 9959-9969.

[64] L. Noodleman, D. A. Case, A. Aizman, *Journal of the American Chemical Society*, 1988, **110**, 1001-1005.

[65] P. E. M. Siegbahn, J. Almlof, A. Heiberg, B. O. Roos, *J. Chem. Phys*., 1981, **74**, 2384, (*13 pages)*.

[66] B. O. Roos, P. R. Taylor and P. E. M. Siegbahn, *Chemical Physics*, 1980, **48**, 157-173.

[67] K. P. Lawley, *Ab initio methods in quantum chemistry. Pt.1, edited by K.P. Lawley*, Wiley, Chichester, 1987. Page 409.

[68] J. Paldus, *Physical Review A*, 1976, **14**, 1620-1625.

[69] R. McWeeny, B. T. Sutcliffe, *Methods of molecular quantum mechanics*, Reprinted with SI units and revisions. edn., Academic Press, London, 1976, 61-75.

[70] P. W. Atkins, R. Friedman, *Molecular quantum mechanics*, 5th ed. edn., Oxford University Press, Oxford, 2011, 304.

[71] R. Ditchfield, W. J. Hehre, J. A. Pople, *J. Chem. Phys.*, 1971, **54**, 724, (5 pages).

[72] W. J. Hehre, R. Ditchfield, J. A. Pople, *J. Chem. Phys.*, 1972, **56**, 2257, (5 pages).

[73] Schaefer, H. Horn, R. Ahlrichs, *J. Chem. Phys.*, 1992, **97**, 2571-2577.

[74] H. F. Schaefer, C. Huber, and R. Ahlrichs*, J. Chem. Phys.*, 1994, **100**, 5829-5835.

[75] F. Weigend and R. Ahlrichs, *Phys. Chem. Chem. Phys.*, 2005, **7**, 3297-3305.

[76] M. J. Frisch, J. A. Pople, J. S. Binkley, *J. Chem. Phys.*, 1984, **80**, 3265, (5 pages).

[77] C. K. Skylaris, L. Gagliardi, N. C. Handy, A. G. Ioannou, S. Spencer and A. Willetts, *Journal of Molecular Structure-Theochem*, 2000, **501**, 229-239

[78] J. Leszczynski and M. Shukla, *Practical aspects of computational chemistry : methods, concepts and applications*, Springer, Heidelberg, 2009, page 8.

[79] K. Eichkorn, O. Treutler, H. Ohm, M. Haser, R. Ahlrichs, *Chem Phys Lett*, 1995, **240**, 283-289.

[80] M. Barysz and Y. Ishikawa, *Relativistic methods for chemists*, Springer, Dordrecht ; London, 2010, 168.

[81] K. G. Dyall and K. Fægri, *Introduction to relativistic quantum chemistry*, Oxford University Press, Oxford, 2007, 52.

[82] E. van Lenthe, E. J. Baerends, J. G. Snijders, *J. Chem. Phys.*, 1993, **99**, 4597, (14 pages).

[83] E. van Lenthe, J. G. Snijders, E. J. Baerends, *J. Chem. Phys.*, 1996, **105**, 6505, (12 pages).

[84] C. van Wüllen, *J. Chem. Phys.*, 1998, **109**, 392 (8 pages).

[85] E. K. Zavoski, *J. Phys. USSR*, 1945, **9**, 211.

[86] K. Nakamura, K. Hagiwara, K. Hikasa, H. Murayama, M. Tanabashi, T. Watari, C. Amsler, M. Antonelli, D. M. Asner, H. Baer, *et.al*, *J. Phys.*, 2010, **G 37**, 075021.

[87] R. Boca, *Coord. Chem. Rev.*, 2004, **248**, 757-815.

[88] F. Neese, E. I. Solomon, *Magnetism : molecules to materials*, J. S. Miller, M. Drillon, Weinheim, Wiley-VCH, Great Britain, 2002, 347.

[89] F. Neese, *High resolution EPR : applications to metalloenzymes and metals in medicine*, R. Hanson, L. J. Berliner, Springer, G. New York ; London, 2009. Ch 5, 176.

[90] C. A. Hutchinson, B. W. Mangum, *J. Chem. phys.*, 1958, **29**, 952, (2 pages).

[91] R. Sessoli, D. Gatteschi, A. Caneschi, M. A. Novak, *Nature*, 1993, **365**, 141-143.

[92] C. D. Delfs, R. Bramley, *J. Chem. Phys.*, 1997, **107**, 8840, (8 pages).

[93] A. Carrington and A. D. Maclachlan, *Introduction to magnetic resonance, with applications to chemistry and chemical physics*, Harper & Row, New York, etc., 1967, 121-122.

[94] D. Ganyushin, F. Neese, *J. Chem. Phys.*, 2013, **138**, 104113, (19 pages).

[95] F. Neese, F. Wennmohs, *ORCA - An ab initio, DFT and semiempirical SCF-MO package, version 2.9*, 2012, http://cec.mpg.de/forum/OrcaManual.pdf, 479.

[96] R. McWeeny, *Methods of molecular quantum mechanics*, 2nd ed. edn., [s.n.], Acad. Press, 1976, 390.

[97] J. E. Harriman, *Theoretical foundations of electron spin resonance*, Academic Press, [S.l.], 1977, 192.

[98] F. Neese, *High resolution EPR : applications to metalloenzymes and metals in medicine*, R. Hanson, L. J. Berliner, Springer, G. New York ; London, 2009. Ch 5, 183.

[99] B. A. Hess, C. M. Marian, U. Wahlgren, O. Gropen, *Chem. Phys. Lett.*, 1996, **251**, 365-371.

[100] F. Neese, *J. Chem. Phys*., 2005, **122**, 034107, (13 pages).

[101] R. Pederson, S. N. Khanna, *Phys. Rev. B*, 1999, **60**, 9566-9572.

[102] F. Neese, *J. Am. Chem. Soc.*, 2006, **128**, 10213-10222.

[103] S. Schmitt, P. Jost, C. van Wüllen, *J. Chem. Phys.*, 2011, **134**, 194113 (11 pages).

[104] I. Mayer, *Int. J. Quantum. Chem*., 1986, **29**, 477-483.

[105] M. J. Frisch, G. W. Trucks, H. B. Schlegel, G. E. Scuseria, M. A. Robb, J. R. Cheeseman, G. Scalmani, V. Barone, B. Mennucci, G. A. Petersson, H. Nakatsuji, M. Caricato, X. Li, H. P. Hratchian, A. F. Izmaylov, J. Bloino, G. Zheng, J. L. Sonnenberg, M. Hada, M. Ehara, K. Toyota, R. Fukuda, J. Hasegawa, M. Ishida, T. Nakajima, Y. Honda, O. Kitao, H. Nakai, T. Vreven, J. A. Montgomery, Jr., J. E. Peralta, F. Ogliaro, M. Bearpark, J. J. Heyd, E. Brothers, K. N. Kudin, V. N. Staroverov, R. Kobayashi, J. Normand, K. Raghavachari, A. Rendell, J. C. Burant, S. S. Iyengar, J. Tomasi, M. Cossi, N. Rega, J. M. Millam, M. Klene, J. E. Knox, J. B. Cross, V. Bakken, C. Adamo, J. Jaramillo, R. Gomperts, R. E. Stratmann, O. Yazyev, A. J. Austin, R. Cammi, C. Pomelli, J. W. Ochterski, R. L. Martin, K. Morokuma, V. G. Zakrzewski, G. A. Voth, P. Salvador, J. J. Dannenberg, S. Dapprich, A. D. Daniels, Ö. Farkas, J. B. Foresman, J. V. Ortiz, J. Cioslowski, and D. J. Fox, Gaussian, Inc., Wallingford CT, Gaussian 09,

Revision A.1, 2009.

[106] F. H. Allen, *Acta Cryst., B*, 2002, **58**, 380-388.

[107] I. J. Bruno, J. C. Cole, P. R. Edgington, M. Kessler, C. F. Macrae, P. McCabe, J. Pearson, R. Taylor, *Acta Cryst., B,* 2002, **58**, 389-397.

[108] J. Krzystek, A. Fiedler, J. Sokol, A. Ozarowski, S. Zvyagin, T. Brunold, J. Long, L. Brunel, J. Telser, *Inorg. Chem.* 2004, **43**, 645–5658.

[109] A. Behrens, D. Rehder, Private Communication to Crystallographic Database. 2009**.**

[110] L. Singer, *J. Chem. Phys*, 1955, **23**, 379–388.

[111] S. Bott, B. Fahlman, M. Pierson, A. Barron, *J. Chem. Soc. Dalton.* 2001, 2148–2152.

[112] J. Krzystek,. G.J Yeagle, J. H. Park, R. D. Britt, M.W. Meisel, L.C. Brunel, J. Telser, *Inorg. Chem.* **2003**, 42, 4160-4681.

[113] R. Stults, R. S. Marianelli, V. W. Day, *Inorg Chem.* 1979, **18**, 1853–1858.

[114] D. Collison, A. L. K. Powell, *Inorg. Chem.* 1990, **29**, 4735–4746.

[115] R. Roof, *Acta Crystallogr.* 1956, **9**, 781–786.

[116] W. Clegg, *Acta Crystallog. C.* 1985, **41**, 1164–1166.

[117] A. Caneschi, D. Gatteschi, R. Sessoli, A. L. Barra, L. C. Brunel, M. Guillot *J. Am. Chem. Soc*., 1991, **113**, 5873-5874.

[118] J. Cirera, E. Ruiz, S. Alvarez, F. Neese, J. Kortus, *Chem. Eur. J.,* 2009, 15, 4078–4087.

[119] D. E Bolster, P. Gütlich, W. E. Hatfield, S. Kremer, E. W. Muller, T. L. Wieghardt, *Inorg. Chem.* 1982, **22**, 1725-1729

[120] S. Kremer, *Inorg. Chem.*, 1985, **24**, 887-890

[121] A. L. Barra, A. Caneschi, A. Cornia, F. Fabrizi de Biani, D. Gatteschi, C. Sangregorio, R. Sessoli, L. Sorace. *J. Am. Chem. Soc*., 1999, **121**, 5302–5310

[122] G. A. Timco, E. J. L. McInnes, R. G. Pritchard, F. Tuna, R. E. P. Winpenny, *Ange. Chem. Int. Ed*., 2008, **50**, 9681- 9684.